Argonne NATIONAL LABORATORY

ANL-06/49

Yucca Mountain Project

FY 2006 Annual Report for Waste Form Testing Activities

Chemical Engineering Division

About Argonne National Laboratory

Argonne is a U.S. Department of Energy laboratory managed by UChicago Argonne, LLC under contract DE-AC02-06CH11357. The Laboratory's main facility is outside Chicago, at 9700 South Cass Avenue, Argonne, Illinois 60439. For information about Argonne, see www.anl.gov.

Availability of This Report

This report is available, at no cost, at http://www.osti.gov/bridge. It is also available on paper to the U.S. Department of Energy and its contractors, for a processing fee, from:

U.S. Department of Energy
Office of Scientific and Technical Information
P.O. Box 62
Oak Ridge, TN 37831-0062
phone (865) 576-8401
fax (865) 576-5728
reports@adonis.osti.gov

ANL-06/49

YUCCA MOUNTAIN PROJECT

FY 2006 Annual Report for Waste Form Testing Activities

by

W. L. Ebert, J. A. Fortner, A. V. Guelis, and J. C. Cunnane

Chemical Engineering Division
Argonne National Laboratory
9700 South Cass Avenue
Argonne, Illinois 60439

October 2006

Conducted under
MPO No. B004210CM3X

INTENTIONALLY LEFT BLANK

CONTENTS

CONTENTS (continued)

FIGURES

FIGURES (continued)

FIGURES (continued)

TABLES

ACKNOWLEDGEMENTS

Use of the Advanced Photon Source was supported by the DOE's Office of Energy Research, Basic Energy Sciences. We thank Yifen Tsai for performing the inductively coupled plasma mass spectrometry and gamma spectroscopy analyses, and Dr. A. Jeremy Kropf for analyses at the APS and data interpretation.

ACRONYMS

AMR	Analysis/Model report
ANL	Argonne National Laboratory
APS	Advanced Photon Source
ATM	approved test material
BSC	Bechtel SAIC Company, LLC
CSNF	commercial spent nuclear fuel
EDS	energy dispersive x-ray spectroscopy
EXAFS	extended x-ray absorption fine structure
FY	fiscal year
HA	humid air
HDR	high drip rate
HLW	high-level waste
ICP-MS	inductively coupled plasma – mass spectrometry
LDR	low drip rate
MPO	Memorandum Purchase Order
MR-CAT	Materials Research – Collaborative Access Team
MWd/kgU	Megawatt days per kilogram of Uranium
NIST	National Institute of Standards and Technology
PA	performance assessment
PTFE	polytetrafluoroethylene
QA	Quality Assurance
SAED	selected area electron diffraction
SEM	scanning electron microscopy
SHE	standard hydrogen electrode
SITP	scientific investigation test plan
SRM	Standard Reference Material
TBD	to be determined
TEM	transmission electron microscopy
TSPA	total system performance assessment
XAS	x-ray absorption spectroscopy
XANES	x-ray absorption near-edge spectroscopy
YMP	Yucca Mountain Project

EXECUTIVE SUMMARY
(J. Cunnane)

This report describes the experimental work performed at Argonne National Laboratory (Argonne) during fiscal year (FY 2006) under the Bechtel SAIC Company, LLC (BSC) Memorandum Purchase Order (MPO) contract number B004210CM3X. Because this experimental work is focused on the dissolution and precipitation behavior of neptunium, the report also includes, or incorporates by reference, earlier results that are relevant to presenting a more complete understanding of the likely behavior of neptunium under experimental conditions relevant to the Yucca Mountain repository. Important results relevant to the technical bases, validations, and conservatisms in current source term models are summarized below.

- The CSNF samples were observed to corrode following the general contour of the surface rather than via (for instance) grain boundary attack. This supports the current approach of estimating the effective surface area of corroding CSNF based on the geometric surface area of fuel pellet fragments.

- It was observed that the neptunium and plutonium concentrations in corroded CSNF samples were somewhat higher at and near the corrosion front (i.e., at the interface between the alteration product "rind" layer and the underlying fuel) than in the bulk fuel.

- The neptunium and plutonium at the corrosion front and in the uranyl alteration layer were found to be in the quadravalent (4+) oxidation state.

- The uranyl phases that constitute most of the alteration rind were depleted in neptunium relative to the bulk fuel: neptunium concentrations in the uranyl alteration rind were less than 20% of that in the parent fuel.

- Homogeneous precipitation tests have shown that solids precipitate from a 1×10^{-4} M Np(V) solution over the temperature range of 200–280ºC, but no evidence was found that any solids precipitated from the same solution at 150ºC through 289 days.

- The solids formed in the homogeneous precipitation tests were predominantly a Np(IV)-bearing phase, probably NpO_2.

- The presence of UO_2 resulted in the rapid precipitation at room temperature of similar amounts of Np(IV)- and Np(V)-bearing phases, probably NpO_2 and Np_2O_5. Although the UO_2 is presumed to act as a reducing agent for Np(V) that leads to the precipitation of a Np(IV)-bearing phase, the observed formation of a Np(V)-bearing phase suggests that the UO_2 also catalyzes Np_2O_5 precipitation under these test conditions.

1. INTRODUCTION
(J. Cunnane)

This report describes the experimental work performed at Argonne National Laboratory (Argonne) during fiscal year 2006 (FY 2006) under Bechtel SAIC Company, LLC (BSC) Memorandum Purchase Order (MPO), contract number B004210CM3X. The report is presented in two major sections that correspond to the experimental activities into which the FY 06 work was organized, namely, the examination of commercial spent nuclear fuel (CSNF) that had been reacted in previous corrosion tests and tests to study Np(V) precipitation kinetics. Technical support activities (e.g., hot cell maintenance) that were performed in FY 2006 under this contract are not described. This work was conducted under the current revision of the quality assurance (QA) plan entitled "Quality Assurance Plan for Technical Activities in Support of the Yucca Mountain Project (Argonne QA Document No. YMP-02-001, Rev. 6).

2. EXAMINATION OF CORRODED CSNF
(J. Fortner)

2.1 BACKGROUND

Specimens of unclad fragments of commercial spent nuclear fuel (CSNF) that had been subjected to corrosion testing for up to 10 years under hydrologically unsaturated conditions were examined to elucidate radionuclide release pathways and mechanisms, with particular emphasis on the behavior of neptunium. These unsaturated tests had been used to investigate oxidative dissolution of the fuel, release of radionuclides, and formation of alteration phases that can sequester radionuclides in an oxidizing environment that is relevant to the Yucca Mountain Repository (Finch 2003, Finch et al. 1999). These tests provided substantial information on the relative release rates of various radionuclides, which were generally found to be highly incongruent. Notably, the tests had shown that neptunium was released at a normalized rate roughly similar to that of uranium, but orders of magnitude more slowly than that of molybdenum, cesium, or iodine. Since a significant quantity of uranium was observed to precipitate into alteration phases that formed in these tests, an examination of the CSNF solids would provide a basis for a realistic assessment of neptunium behavior, including a better understanding of solubility-limiting phase(s) and rate-limiting mechanism(s) for the release of this important radionuclide. The work reported here was performed under the Test Plan ANL-TP-04-001, Rev. 01, as part of the BSC Technical Work Plan for Waste Form Testing, TWP-WIS-MD-000018 REV 00 (BSC 2005).

The objectives are:

- Examine corroded CSNF archived from the Argonne unsaturated tests to determine neptunium accumulation at or near the interface between the corroding fuel and the alteration rind.
- Assess the extent to which neptunium is incorporated into the rind's uranyl alteration phases.
- Generally assess the condition of the fuel and alteration rind.

This report focuses on specimens prepared by cross-sectioning intact, corroded fuel fragments recovered from unsaturated tests conducted previously. Also available for study were archived solids that had been removed from the fuel surface during testing using double-sided cellophane tape. Examination of these specimens was reported previously (Argonne 2005).

2.1.1 Neptunium in CSNF

In spent UO_2 fuels the oxygen potential is less than about -400 kJ/mol (-4.1 eV) (Dehaudt 2001). Under these conditions the uranium in the fuel matrix is believed to be present mostly in the U(IV) oxidation state. Neptunium in the fuel is expected to be present as a solid solution of NpO_2 in the UO_2 fluorite structure with which it is compatible (Dehaudt 2001). This is confirmed by recent x-ray absorption near-edge spectroscopy (XANES) studies that indicate the oxidation state of Np in the fuel matrix is Np(IV) and extended x-ray absorption fine structure (EXAFS) measurements that show the Np(IV) is present in a UO_2–like phase. This is consistent

with Np being in solid solution in the fuel's UO_2 fluorite lattice structure (Kropf et al. 2005, Argonne 2005; see also this report, Section 3.4).

In considering processes that impact the release of ^{237}Np from corroding spent nuclear fuel, including incorporation into uranyl alteration phases, it is generally assumed that the Np(IV) in the fuel's UO_2 matrix will undergo oxidative dissolution to Np(V) when the fuel's matrix corrodes in air-saturated solutions (Finch 2002). However, available data for the standard reduction potentials for NpO_2^+/Np^{4+} and UO_2^{2+}/U^{4+} couples indicate that Np(IV) may not be effectively oxidized to Np(V) at the corrosion potentials of uranium dioxide spent nuclear fuel in air-saturated aqueous solutions. Also, local chemical conditions (such as the precipitation of uranyl phases) may facilitate precipitation of any aqueous Np(V) species that are formed. It is therefore important to understand the effect of the fuel matrix on the oxidative dissolution and reductive precipitation of Np to assess processes that will control Np release while the fuel is corroding and to assess the subsequent availability of Np(V) for incorporation into uranyl alteration phases.

The Np release path starts at the corroding fuel surface and progresses through the alteration phase rind to the "bulk solution" ("bulk solution" is used to refer to any solution beyond the immediate influence of the corroding fuel surface). Figure 2.1 illustrates salient features and processes that are considered here for the fuel matrix corrosion and the initial part of the reaction path for Np. It also qualitatively illustrates the relevant potentials (see dashed line) that Np will encounter for reactions occurring at the surface of the fuel (1), in the alteration product rind layer (2), and in the bulk solution (3).

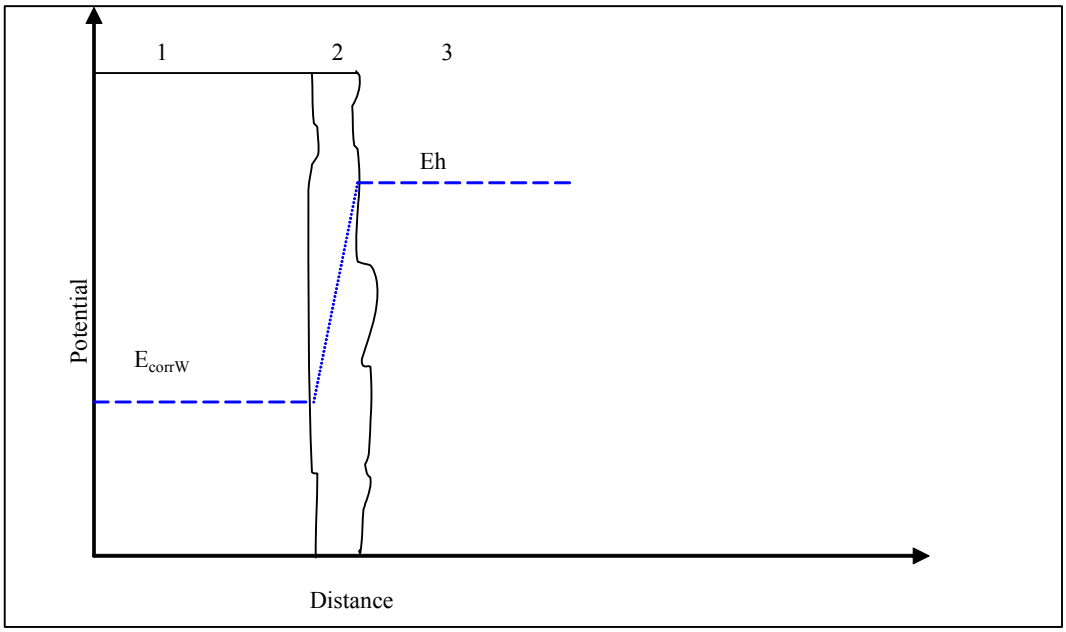

Figure 2.1. Qualitative Illustration of the Variation of the Oxidation Potential Profile at and Near the Corroding Fuel Surface. (1) Bulk fuel, (2) alteration products ("rind"), and (3) bulk solution.

It is instructive to consider the electrochemical interactions between U(IV) and Np(IV) to assess the likely behavior of Np as the host fuel matrix undergoes oxidative dissolution. Reduction of Np(V) by the oxidation of U(IV) as the fuel corrodes is thermodynamically favored, as shown by Equation 2.1 (Finch 2002):

$$2NpO_2^+ + U^{4+} + 4H^+ \leftrightarrows 2\,Np^{4+} + UO_2^{2+} + 2H_2O \qquad E^o = 0.405 \text{ to } 0.469V \qquad (2.1)$$

This indicates that while the fuel is corroding there is potential for reducing dissolved Np(V) to Np(IV) at the surface of the residual fuel.

Although the reduction of Np(V) by U(IV) is favored thermodynamically, the redox kinetics of Np under the corrosion conditions at the corroding fuel surface are uncertain. Measured corrosion potentials (E_{corr}) for spent UO_2 fuels in aerated near-neutral pH solutions depend on many factors but are generally in the range of about 300 to 600 mV on the standard hydrogen electrode (SHE) scale (Shoesmith 2000). Corrosion potentials in the range of 510 to 620mV SHE were also measured for UO_2 in 95% saturated NaCl solutions when 0.1M H_2O_2 was added to simulate the influence of radiolysis products (Grambow et al. 2000, p. 123). These data indicate that the fuel's corrosion potential (E_{corrW} in Figure 2.1) may be lower than the standard potential for the anodic oxidative dissolution of Np(IV). This indicates that oxidation of Np(IV) to Np(V) may not occur under the pertinent potential conditions at the fuel's surface.

The precipitation behavior of dissolved Np at and near the corroding fuel surface is also potentially important. The Eh/pH thermodynamic stability fields for pure neptunium phases have been estimated (Kaszuba and Runde 1999, Lemire 1984) and indicate that NpO_2 is the most thermodynamically stable Np phase over most of the pH/Eh regime of interest. However, $Np(OH)_4$ and Np_2O_5 may be the most thermodynamically stable phases for more-reducing and higher pH conditions, respectively (Kaszuba and Runde 1999). When the solubility limit of NpO_2 in the solution contacting the corroding fuel surface is reached, NpO_2 will likely precipitate onto, or be incorporated into, the corroding UO_2 fluorite lattice structure. This indicates that the dissolved concentration of Np at the corroding CSNF surface is likely to be controlled by the solubility of $U_{(1-x)}Np_xO_2$ or $U_{(3-x)}Np_xO_8$. As illustrated by the dashed line in Figure 2.1, any Np(IV) released from the corroding fuel surface (i.e., from the interface between regions 1 and 2) will encounter increasingly oxidizing conditions as it diffuses away from the fuel surface through the alteration phase rind layer and into the bulk solution. As Np(V) is the predominant oxidation state for the aqueous species in air-saturated water (Kaszuba and Runde 1999, Lemire 1984), it is likely that most of the aqueous Np(IV) will be oxidized to Np(V) as it traverses the corrosion product rind that forms on the fuel. This Np(V) would be available for incorporation into precipitating uranyl alteration phases (Burns, Ewing, and Miller 1997; Burns, Deely, and Skanthakumar 2004). If oxidation is inhibited, it may result in Np being incorporated into uranyl phases at concentrations below that found in the parent fuel (Fortner et al. 2004). The work described in this report is designed to build upon previously reported findings that suggest a possible enrichment of Np at the corrosion front and a low level of Np residing in the alteration layer (Argonne 2005). Confirmation of these findings would support the hypothesis that Np(IV) in the fuel is not effectively oxidized to Np(V) as the fuel corrodes.

2.2 APPROACH

2.2.1 Test Materials

Corrosion tests to study the release of radionuclides from commercial spent nuclear fuel (CSNF) under hydrologically unsaturated conditions were conducted at Argonne National Laboratory during a 10-year period from 1992 until 2002. The tests subjected approximately 8 grams of unclad fuel pellet fragments (~5-mm diameter chunks) to humid air and intermittent (twice weekly) dripping ground water at rates of either 0.15 mL/week or 1.5 mL/week. The tests were referred to as "vapor" (100% relative humidity, but no injected water), low-drip-rate, and high-drip-rate tests, respectively. Tests with pressurized-water-reactor (PWR) spent fuel specimens were run for approximately 10 years (1992 to 2002) and tests with boiling-water reactor (BWR) spent fuels ran for about 4 years (1998 to 2002). Commonly known as the Argonne "drip tests," this series of investigations was conducted under the auspices of the OCRWM Yucca Mountain Project. Two of the fuels, ATM-103 and ATM-106, were PWR fuel with nominal burnups of 30 and 45 MWd/kgU, respectively (Guenther et al. 1988a, 1988b). The other three fuels, ATM-109A, ATM-109B, and ATM-109C (Goldberg 2003) were BWR fuels with burnups of 64, 71, and 72 MWd/kgU, respectively. One BWR fuel (ATM-109C) contained 2% Gd as a burnable neutron absorber. Characteristics of the five fuels are summarized in Table 2.1. The unsaturated tests and findings are described in detail elsewhere (Finch et al. 1999, Finch 2003).

After the drip tests were terminated, the remaining fuel and alteration phases (plus metal internal components) were stored in labeled containers within the hot cell facilities in Building 205 at Argonne National Laboratory (ambient laboratory atmosphere). These materials have proven to be a valuable source of information that complements the leachate solution data (Argonne 2005, Finch 2003). These materials consist mainly of unaltered uranium oxide CSNF with a thin alteration rind of uranyl phases ranging in composition from pure uranyl oxyhydrates formed in the water vapor tests to sodium and calcium uranyl silicates formed in the high drip-rate tests (Finch et al. 1999).

2.2.2 Methodology

Initially, all fuel fragments from the tests were photographed "as received" when taken from storage. In most cases, the fuel was still in its original test configuration within the zircaloy fuel holder. These photographs document the condition of the corroded fuel fragment specimens. Next, individual fuel fragments were selected from among the different fuel and test types (the ATM-109 fuels were not selected owing to shorter test duration and higher specific radioactivity). The selection process was random, as there were multiple fragments of each type stored together from each test, and these were not distinguishable from the vantage of the hot cell operation to isolate an individual fragment (in one case, ATM-106 high drip rate, two fuel fragments were embedded together in a single epoxy block). The fuel fragments were embedded in a slow-curing, low-viscosity transparent epoxy (Epo-thin™, by Buehler) in a plastic container. The embedded fragment(s) were then cut into sections about 1 mm thick with a diamond-encrusted wafering saw. These cut sections were then photographed to document the appearance

Table 2.1. Characteristics of LWR Fuels Used in Tests [a]

Fuel	ATM-103 [b]	ATM-106 [c]	ATM-109A [d]	ATM-109C [d]	ATM-109B [d]
Reactor	PWR	PWR	BWR	BWR	BWR
Burnup (MWd/kgU)	30	45	71	64	72
Grain Size (μm)	17-20	6-16	~15	Bimodal 5, 10-20	~30
Fission Gas Release (%)	<0.25	11	4.4	3.5	2.95
Rim Structure Thickness (μm)	None	100	80-140	150-250 Confined to 5 μm grains	100-180
Out-of-reactor	1980	1980	1991	1991	1991
Gd (%)[e]	<0.02	<0.02	<0.02	2	<0.02
Test Type [f]	HDR, LDR, HA	HDR, LDR, HA	HDR, HA	HDR, HA	HA
Approximate test duration (years)	10	10	4	4	4

[a] Adapted from SITP-02-WF-001, Rev. 00.
[b] Guenther et al. (1988a).
[c] Guenther et al. (1988b).
[d] Vaidyanathan et al. (1997); see also Goldberg (2003).
[e] All fuels have radiogenic Gd from fission; ATM-109C was doped with 2% Gd as burnable neutron poison.
[f] HDR – High drip rate (~1.5 mL each week); LDR– low drip rate (~0.15 mL each week), HA – humid air (saturated water vapor in air).

of the alteration rind, especially its apparent thickness, and the condition of the interface between the interior fuel and the rind.

The next goal was to further reduce the volume of fuel in the specimen while keeping an intact alteration layer to allow removal of a specimen small enough to be handled outside of the heavily shielded hot cell facility for further analysis. Our approach was to re-embed a cut section in epoxy, and extract a core sample using a tubular stainless steel bit. The bit was nominally 1.5 mm in diameter and encrusted with diamond abrasive (available from Dad's Rock Shop, Mohave, Arizona). The coring was manually operated from a variable-speed tabletop drill press through a gloved port access once the CSNF specimen had been cut to a size small enough for direct handling (Figure 2.2).

The next objective was to remove the core fuel sample from the bit and again re-embed the specimen (now reduced to a fragment smaller than a grain of rice) in fresh epoxy. This small specimen would meet requirements for glove box operations, where the core itself would be cross sectioned using a diamond-encrusted wafering saw, to expose a fuel/alteration rind interface. This objective, still carried out through glove port access to the hot cell, proved to be quite difficult. There was only one unqualified success in recovering an intact core from the bit. Attempts to "salvage" a core stuck in the bit provided mixed results, as discussed below. This is largely because obtaining a cross section of a core that remained in the bit required sectioning the bit itself, an operation that took weeks, rather than the approximately

Figure 2.2. Miniature Drill Press for Coring CSNF Specimens Using a Hollow Stainless Steel Bit with Diamond Abrasive, Shown in the Hot Cell

30 minutes needed to cross-section the single extracted core. The extended abrasion experienced while sectioning the diamond-encrusted coring bit with a diamond-encrusted wafering saw caused extensive damage to the specimen. In one case, nearly the entire fuel core was abraded away.

Once a cross-sectioned core was obtained, it was removed from the glove box to a hood for decontamination, then transferred to a scanning electron microscope (SEM) for further examination. Once the specimen was examined in the SEM, it was re-packaged under multiple layers of kapton film (for radiological containment) and transferred to the Argonne Advanced Photon Source (APS) synchrotron for x-ray absorption spectroscopy (XAS) and x-ray imaging. In the case of one specimen (ATM-106, high drip rate specimen, which is discussed in detail below), multiple sessions at the APS were undertaken to revisit and improve details of observations that proved most interesting.

2.3. RESULTS AND DISCUSSION

2.3.1 Examination of Intact Corroded Fuel Fragments: Visible Light Microscopy

A starting point for characterizing the state of the CSNF solids from the unsaturated tests was to examine the material using visible light microscopy. This allows qualitative description

of the alteration phase coverage and distribution. Of particular interest are details of the occurrence and extent of grain boundary penetration. One can directly observe how the alteration rind follows the contours of the pellet surfaces. From the apparent corrosion, one can distinguish whether the pellet size, fragment size, or grain size establishes the appropriate length scale for estimating the effective surface area undergoing corrosion. Similarly, observations can be made to help determine whether changes in water penetration or exclusion occur as a result of the self-sealing of pathways. Visible light microscopy was carried out on all intact fuel fragments. Selected fuel fragments were epoxy-embedded and cross-sectioned for a direct view of the alteration rind/fuel interface.

Light microscopy of the CSNF solids as-received post-test revealed a coating of white-to-yellow alteration products covering most of the (initially black) oxide fuel (Figures 2.3a – 2.3h). Some areas of the alteration coating had been spalled off, either incidentally from handling or as a deliberate effort to recover some of the alteration material. The coating of alteration material is mildly adherent. Note that the alteration materials coating the ATM-109 fuels (Figures 2.3g and 2.3h) are more sparse owing to the shorter test duration (4 years vs. 10 years for the ATM-103 and -106 fuels). A more extensive collection of light micrographs of the intact fuel specimens appears in an earlier report (Argonne 2005). The most salient features to be noted from these micrographs are that:

- the similar appearance of the weakly-adherent layers (alteration rinds) formed on the different fuels under different test conditions,
- the crystals within the alteration rinds are cemented together, and
- the rinds have a fairly uniform thickness over all of the fragments.

2.3.2 Examination of Cross-Sectioned Fuel Fragments: Visible Light Microscopy

To provide greater detail, selected fragments of the CSNF specimens were embedded in epoxy resin and cross-sectioned using a diamond-blade saw. Light microscopy of these cross-sectioned fragments revealed that the alteration rind was relatively thin and mostly adherent (Figures 2.4 through 2.6). There was no evidence of gross grain boundary penetration or degradation of the interior of the CSNF fragments.

Cross-sections of a fuel fragment from ATM-103 tested for nearly 10 years at high drip rate appear in Figure 2.4. Aside from a continuous coverage of a thin (15-30 micrometers) alteration rind, there is little evidence of fuel alteration. Based on the available evidence, it appears that fuel grain induration is retained and grain boundary penetration by water and alteration phases is limited to the geometric periphery of the fuel fragments. In other words, the effective surface area of contact between the unclad CSNF and liquid water/water vapor is consistent with geometric surface area estimates of the fuel fragments.

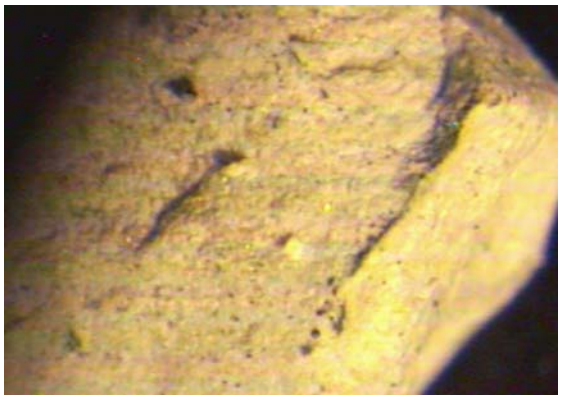

Figure 2.3a. Low-Drip-Rate-Tested ATM-103, Post-Test

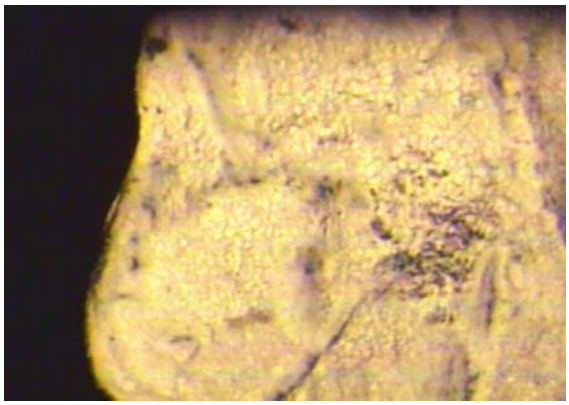

Figure 2.3b. High-Drip-Rate-Tested ATM-103, Post-Test.

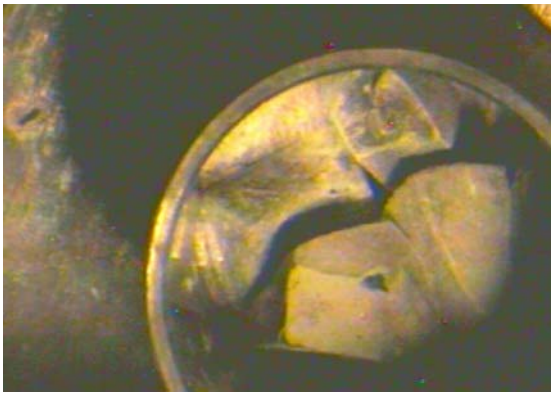

Figure 2.3c. Vapor-Tested ATM-106, Post-Test. Note scale: the outside diameter of the zircaloy fuel holder is 1.34 cm.

Figure 2.3d Vapor-Tested ATM-106, Post-Test. Part of the zircaloy fuel holder (outside diameter 1.34 cm) is visible in the left of the image.

Figure 2.3e. High-Drip-Rate-Tested ATM-106, Post-Test. Note spalling of some of the alteration rind to expose black fuel.

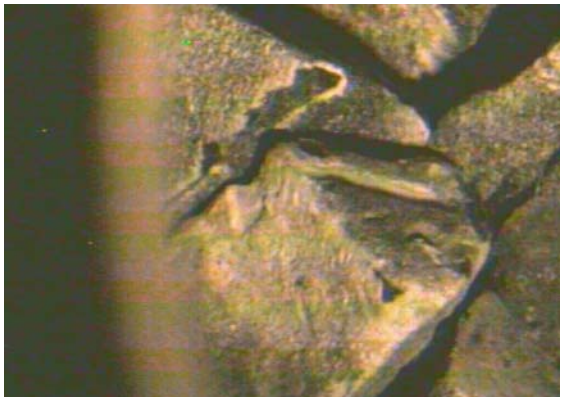

Figure 2.3f. High-Drip-Rate-Tested ATM-106, Post-Test, Detail. Part of the zircaloy fuel holder (outside diameter 1.34 cm) is visible in the left of the image.

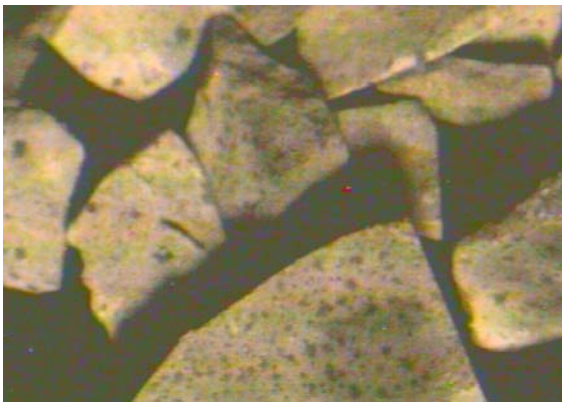

Figure 2.3g. High-Drip-Rate-Tested ATM-109A, Post-Test

Figure 2.3h. Vapor-Tested ATM-109B, Post-Test.

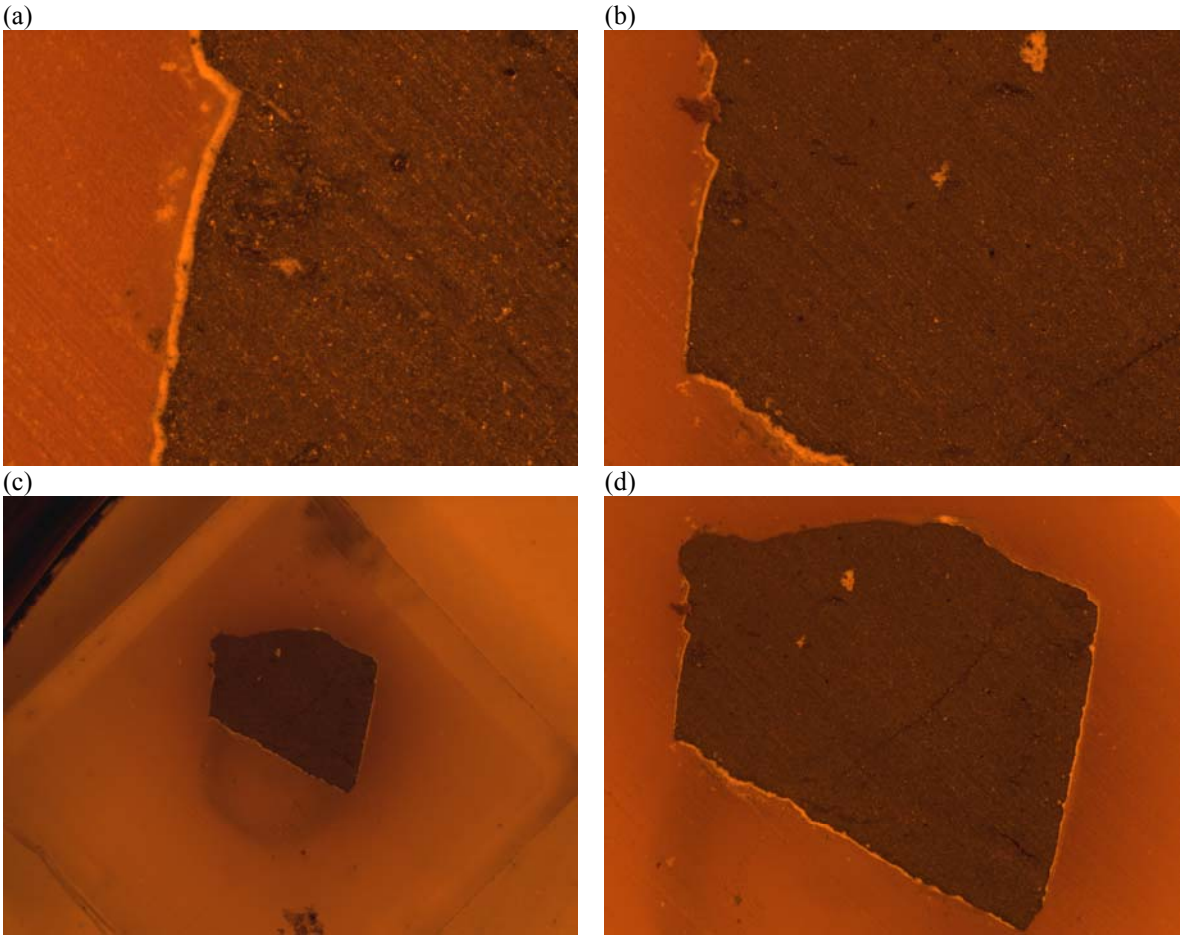

Figure 2.4. ATM-103 High-Drip-Rate Test Specimen, Epoxy-Embedded and Cross-Sectioned. Micrographs are decreasing in magnification clockwise from upper right. Based upon the known size of the square epoxy block (12 mm) visible in the lowest magnification image, the thickness of the alteration layer can be estimated as varying between 15 and 30 micrometers (Argonne 2005).

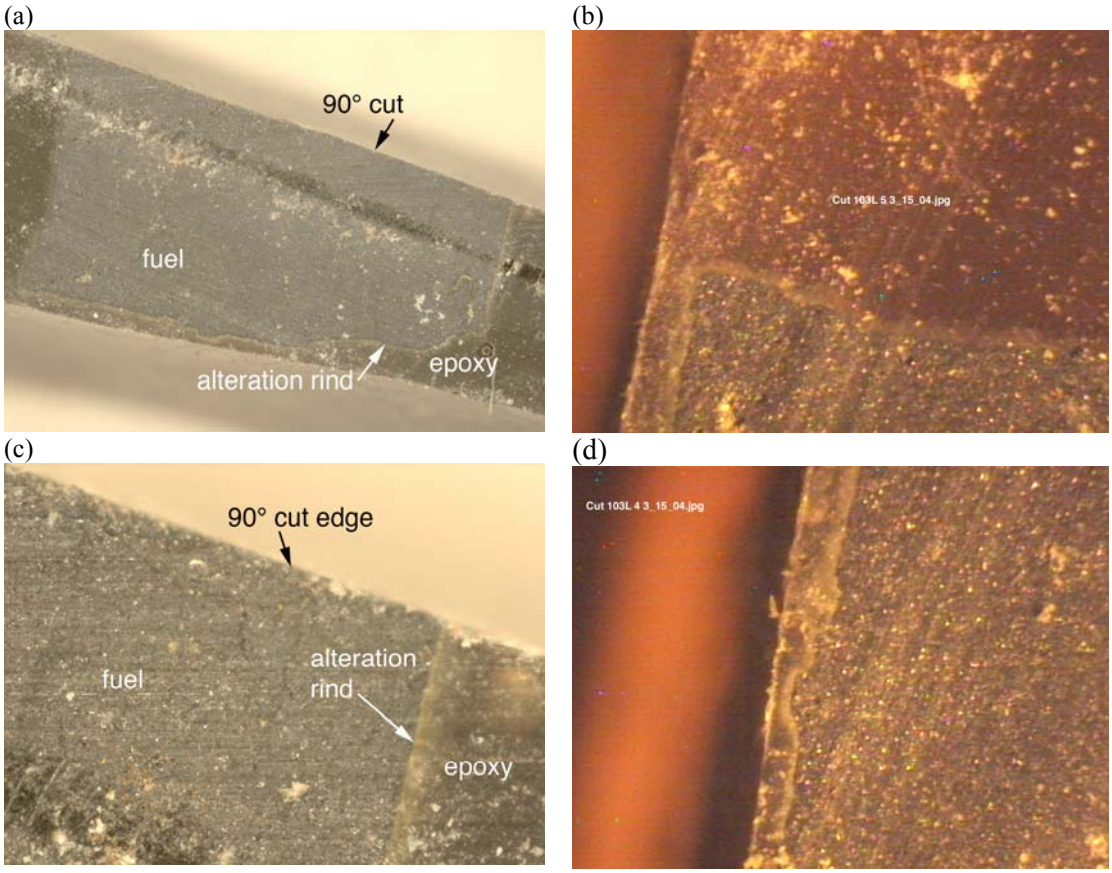

Figure 2.5. Cross-Sectioned Fragment of ATM-103 from Low-Drip-Rate Test of 10 Years. The field of view in (a) is approximately 5 mm across. A deep scoring, or tool mark, is visible roughly parallel to the 90° cut face (Argonne 2005).

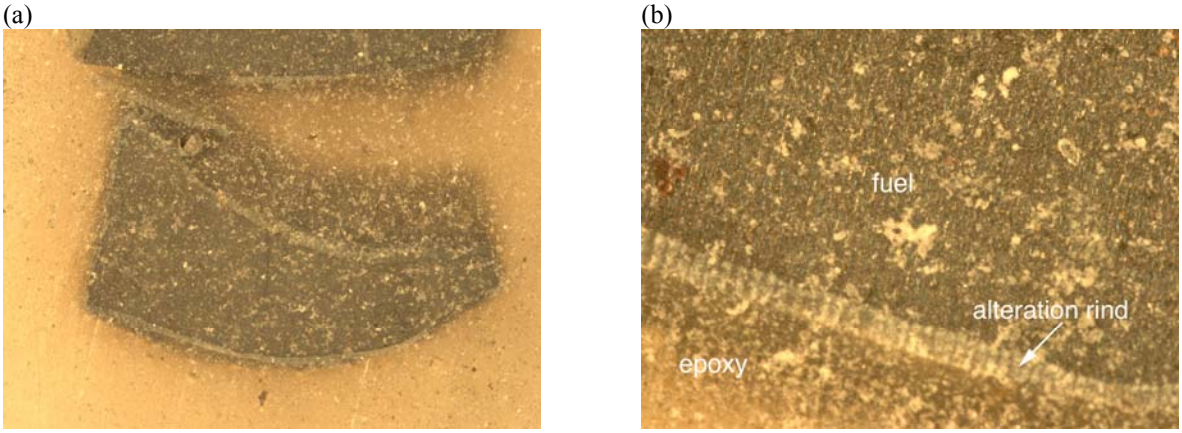

Figure 2.6. Cross-Section of the ATM-106 Fragment from the High-Drip-Rate Test That Was Cored for Most of the SEM and XAS Studies (Argonne 2005).

The light microscope images of as-cut ATM-103 specimens tested under low-drip test conditions appear in Figure 2.5. Note the very thin alteration rind, and the sharp, intact edge at the 90° cut (intersection of 2 orthogonal cuts through the fuel). The sharp edge suggests that the interior of the fuel fragment has remained unaffected during 10 years of testing, and most corrosion appears to be localized along exposed, geometric surfaces. Note that the epoxy resin has turned a dark gray owing to radiation damage.

Specimens of ATM-106 tested under high-drip-test conditions for 10 years were also epoxy-embedded and cross-sectioned in the hot cell. Photomicrographs were taken using the light microscope, revealing a thin (~100 micrometer) alteration rind surrounding relatively intact fuel fragments (~5 mm across) (Figure 2.6). The alteration rind on the surface of this irregularly shaped fragment is approximately 100-200 micrometers thick, by comparison with the size of the fuel fragment (which is approximately 5 mm across). Note the tenacious alteration rind and sharp interface. Much of the light-colored material scattered across the surface in Figure 2.6 is epoxy debris from the cutting wheel. The alteration rind on this specimen appears somewhat thicker than that seen on the low-drip tests on ATM-103 (Figure 2.5). The alteration appears to have been localized to the region near the geometric surface. Natural analogs for paragenesis of mineral deposits often follow the contour of geometric surface (reaction front) as opposed to complex granular penetration. Based upon the above observations plus those that follow, it appears that the geometric surface area is a justified description of the reaction front area (on the fuel fragment length scale) in the unsaturated tests of CSNF.

2.3.3 Examination of Cross-Sectioned Fuel Fragments: Scanning Electron Microscopy

Cores were taken from the cross sections of fragments from each of the 103 LDR, 103 HDR, and 106 HDR test series, and re-embedded in fresh epoxy. A core of a corrosion-altered CSNF fragment surface of ATM-106 fuel reacted in a high drip rate test, approximately 3 mm long and 1 mm diameter when extracted, was re-embedded into fresh epoxy for further handling, whereupon it broke into 2 separate pieces (Figure 2.7). The re-embedded core, contained in a labeled epoxy block, was removed from the hot cell, and found to be small enough for further hands-on work in the glove box. There, the two core pieces were separated from each other by cutting the epoxy block, and the core pieces were labeled separately as “106 H core-1” and “106 H core-2” for further analysis.

The SEM uses a focused beam of electrons to form an image of the surface of CSNF from the backscattered or secondary electrons. It also can provide elemental compositional information using energy dispersive x-ray fluorescence spectroscopy (EDS). A Hitachi 3000N SEM was used to obtain the electron micrographs shown in this report. The high magnification offered by SEM allows direct observation of details at the CSNF grain size (and below). This greater detail is important to affirm the observation from visible light microscopy that grain boundary penetration does not appear to be a significant contributor to the effective surface area during corrosion.

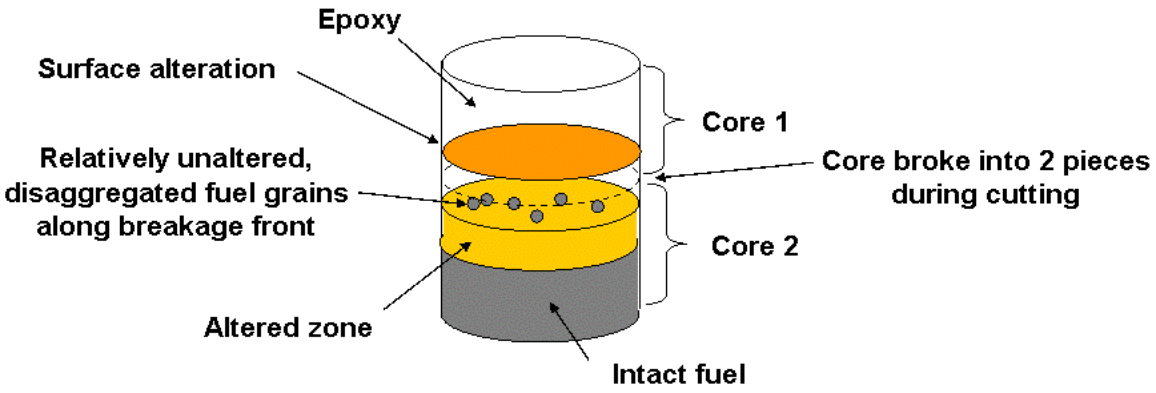

Figure 2.7. Schematic Illustration of the Core Taken from the ATM-106 High-Drip-Rate Test Fragment. The core broke into 2 pieces during re-embedding. See text for discussion; SEM micrographs of the pieces in cross-section appear in Figures 2.5 through 2.7. The core was approximately 1 mm in diameter, and was subsequently re-sectioned radially for SEM and XAS examination.

Backscatter scanning electron micrographs were taken of the cross-sectional cores "106 H core-1" and "106 H core-2". The images in Figure 2.8 show the outermost material (106 H core-1), which contained uranyl silicate and intact 5-metal epsilon particles (Mo, Tc, Ru, Rh, Pd alloy) (Kleykamp et al. 1985, Thomas and Guenther 1989). The presence of these elements was verified using EDS for elemental analysis (not shown).

Figure 2.9 shows backscatter SEM images of a 100- to 200-micrometer-thick alteration rind (medium gray) still attached to relatively unaltered fuel (very light gray) against a black background of epoxy resin from specimen "106 H core-2." Small, bright particles on the upper surface of the alteration rind appear to be disaggregated fuel grains. The presence of fuel grains on the upper surface may be an artifact of the abrasive cutting during sample preparation, but it is also possible that they may have been transported there through the water film during the test. EDS analysis was not possible on this core section owing to its high radioactivity (the EDS detector is sensitive to the beta and gamma emissions from the fuel). Nevertheless, from our previous experience with alteration material from the 106 H test series, the alteration layer from the high-drip-rate tests on ATM-106 is known to consist mainly of uranyl silicates, specifically sodium/potassium boltwoodite [$(Na, K)(UO_2)(SiO_3OH)(H_2O)_{1.5}$] (Argonne 2005, Finch et al. 1999). Close examination of the fuel alteration rind interface in Figure 2.10 reveals some minor grain pullout, which may be a sample preparation artifact or may indicate some sign of grain boundary penetration. Overall, the interface between the fuel and the alteration rind is rather abrupt, and the alteration rind well indurated.

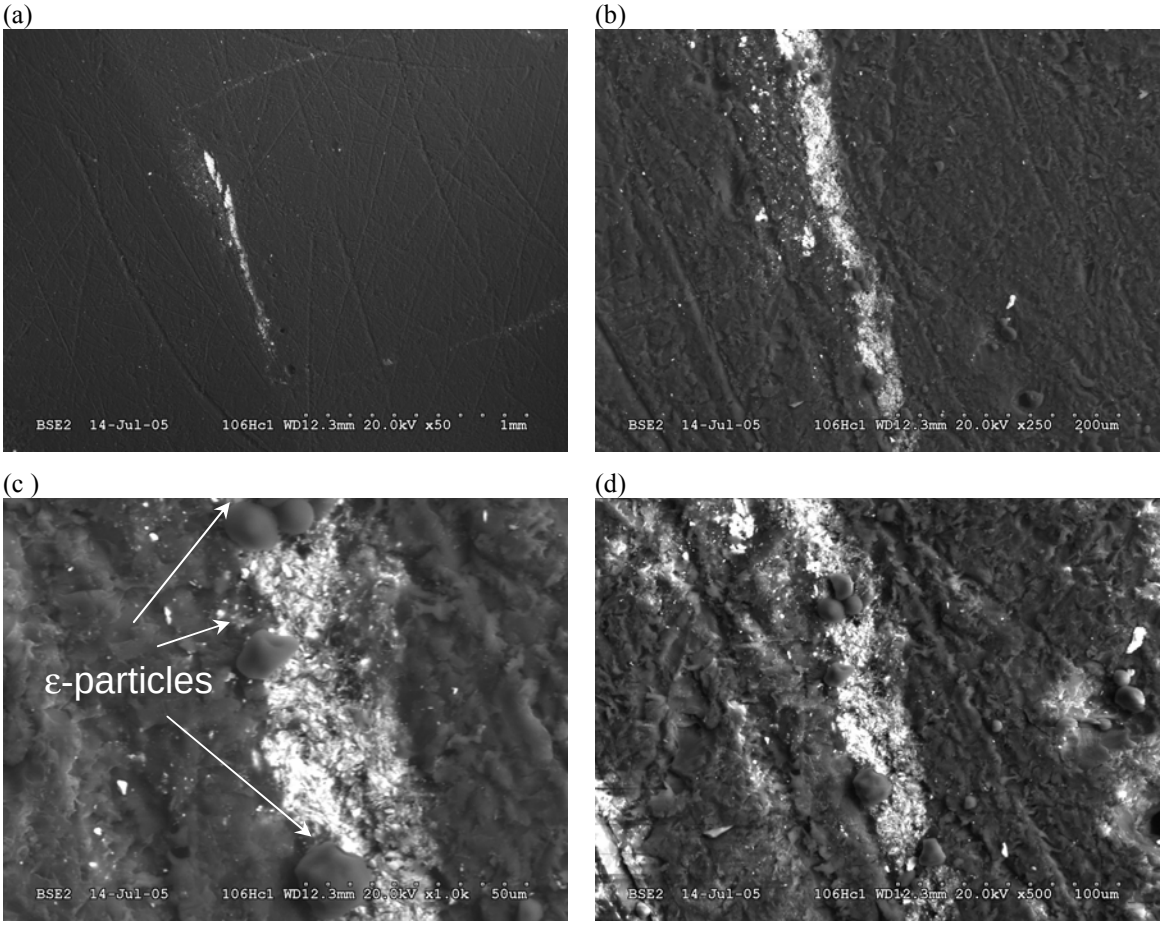

Figure 2.8. SEM Micrograph of the ATM-106 High-Drip-Rate Test Fragment Outer Core ("106 H core 1"), which was Found to be a Thin Outer Layer of Uranyl Silicates with Entrained Epsilon Particles. Magnification increases clockwise from upper left.

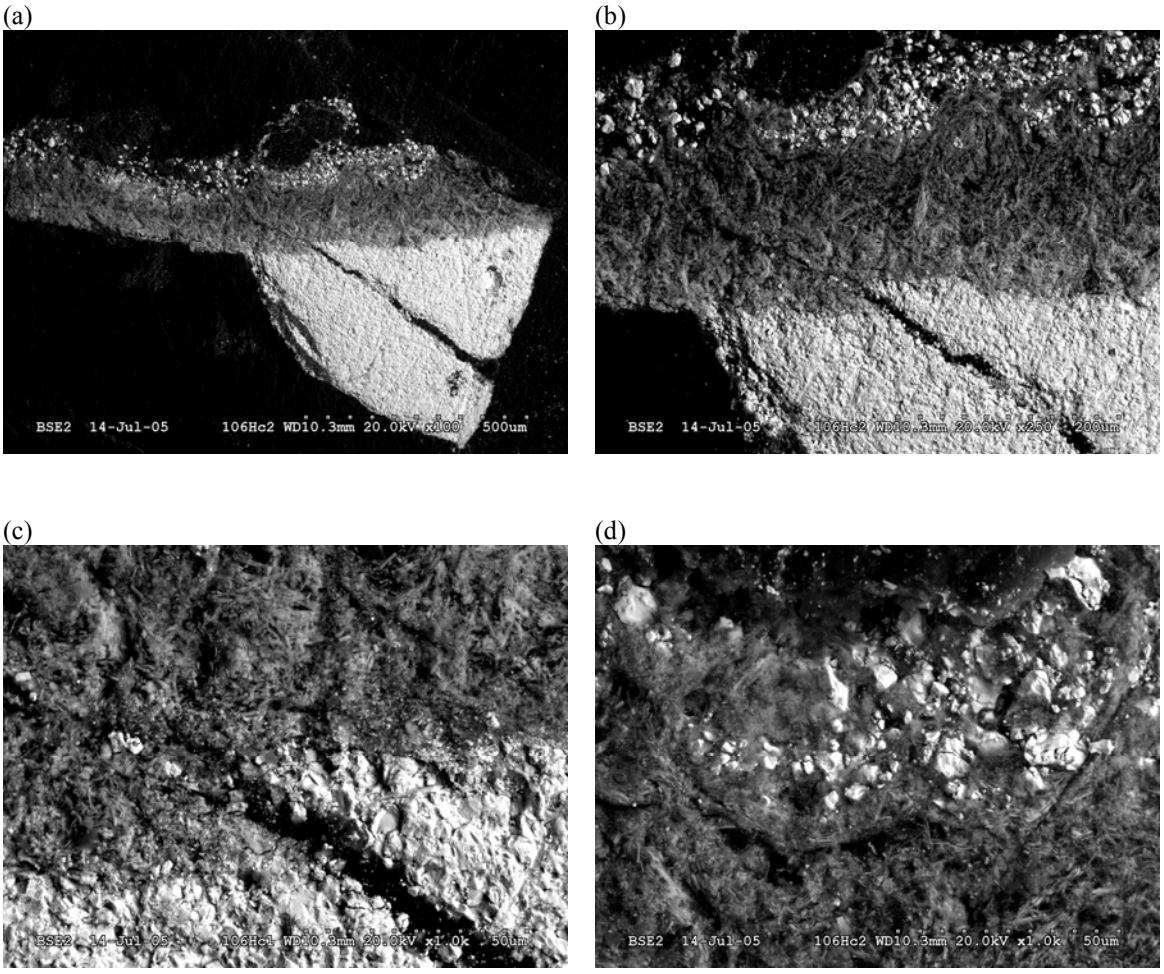

Figure 2.9. Backscatter SEM Micrograph of the ATM-106 High-Drip-Rate Test Fragment Inner Core ("106 H core 2"), which Contained a Piece of Intact Fuel (light colored, dense grained region) with a 100-micron Layer of Uranyl Silicate (gray, acicular, or "needle-like" material) and an Outermost Layer that Appears to Contain Relatively Unreacted, Disaggregated Fuel Grains (also light colored). Magnification increases clockwise from upper left. Note that (c) and (d) are the same magnification but display different regions of the sample.

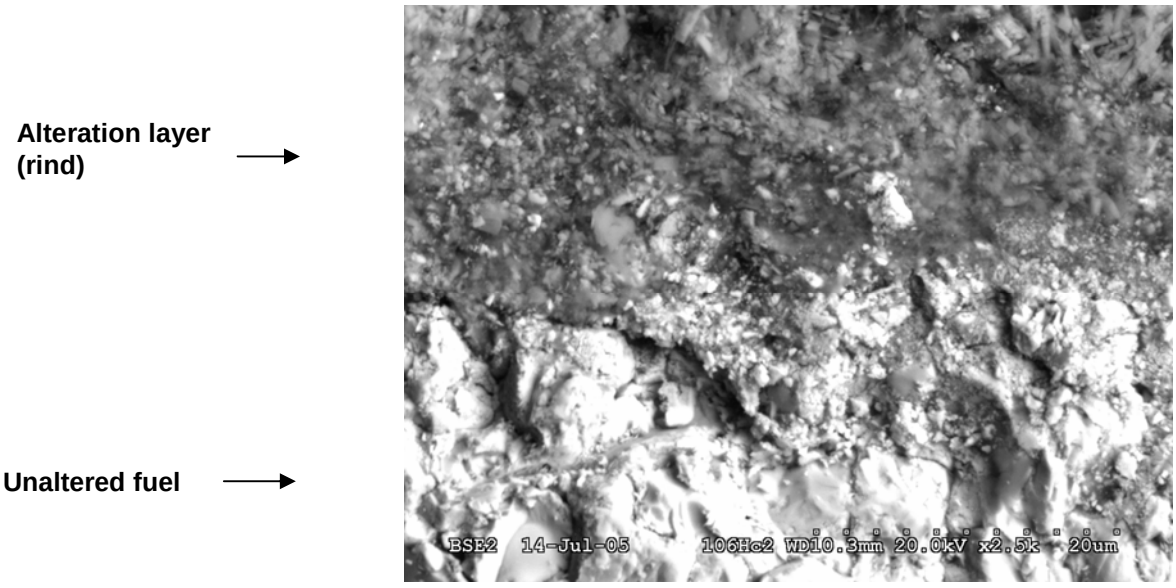

Figure 2.10. High-Magnification Backscatter SEM Micrograph Showing Detail of the Interface between the Unaltered Fuel (below) and the Uranyl Silicate Alteration Phase Layer (above). Note the infusion of the alteration layer through the transition to the unaltered fuel grains, and the fairly sharp boundary between the fuel and the alteration layer.

A micro-cored section of a fuel fragment from the ATM-103 low-drip-rate-tests was also cross-sectioned using a diamond wafering saw. Unlike the high-drip-rate ATM-106 specimen discussed above, the low-drip-rate-tested ATM-103 core section could not be recovered from the diamond-encrusted coring bit. Thus, the entire bit, with the entrapped fuel core, was re-embedded in epoxy and cross-sectioned. The coring bit itself made unambiguous the orientation of the tiny core (which is about 2 mm long with a 0.5 mm diameter) during sectioning. This core was then examined using SEM and XAS. The SEM showed a heavily damaged (presumably from the sample preparation) region of unaltered fuel, but no intact alteration rind was identifiable (Figure 2.11). This was confirmed by XAS, in that no area having a U(VI) signature characteristic of altered fuel could be located.

2.3.4 Examination of Cross-Sectioned Fuel Fragments: X-Ray Absorption Spectroscopy

Few techniques have proven more effective than x-ray absorption spectroscopy (XAS) for determining oxidation states and structural environments of elements in solids. Using a novel "bent-Laue analyzer" (Figure 2.12) we have obtained detailed XAS information from trace elements in specimens of CSNF (Kropf et al. 2005). Several XAS measurements from CSNF were performed at the Materials Research Collaborative Access Team (MR-CAT) insertion device beam line located at sector 10 of the APS. The brightness of the APS facility in the high-energy x-ray regimes makes it ideal for investigating radionuclide systems, which have relatively high-energy absorption edges, and which must be carefully encapsulated for radiological safety. This approach, for the first time, has allowed direct observation of oxidation state, coordination environment, and site symmetry of fission product and actinide elements in CSNF.

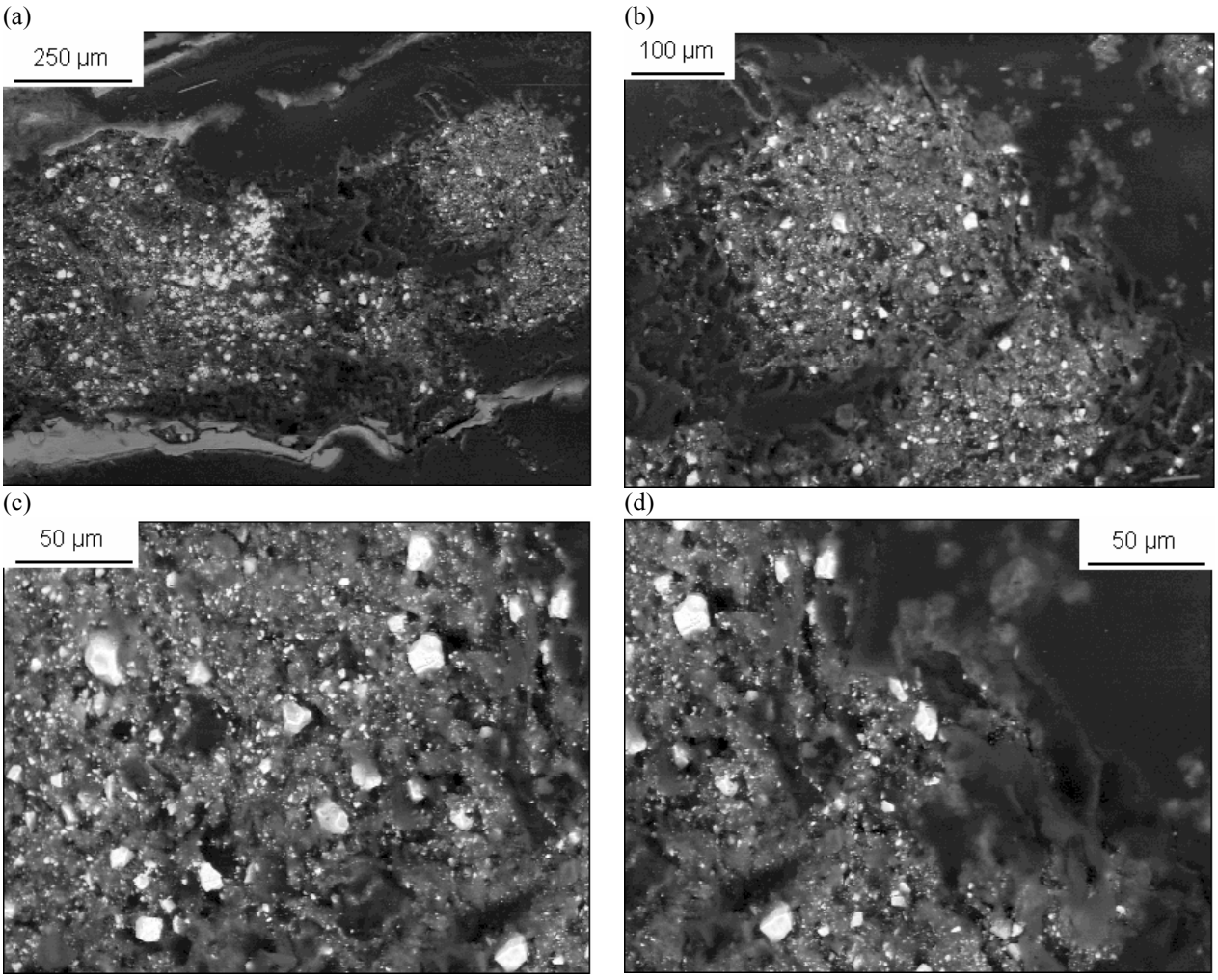

Figure 2.11. SEM Micrographs of Low-Drip-Rate-Tested ATM-103 Core Section. The core failed to release from within the diamond-encrusted stainless steel coring tube, forcing the entire core to be cut. The difficulty of this step caused excessive abrasion and fuel pull-out, so the fuel is less intact than that observed in the high-drip-rate ATM-106 core (compare Figures 2.9 and 2.10).

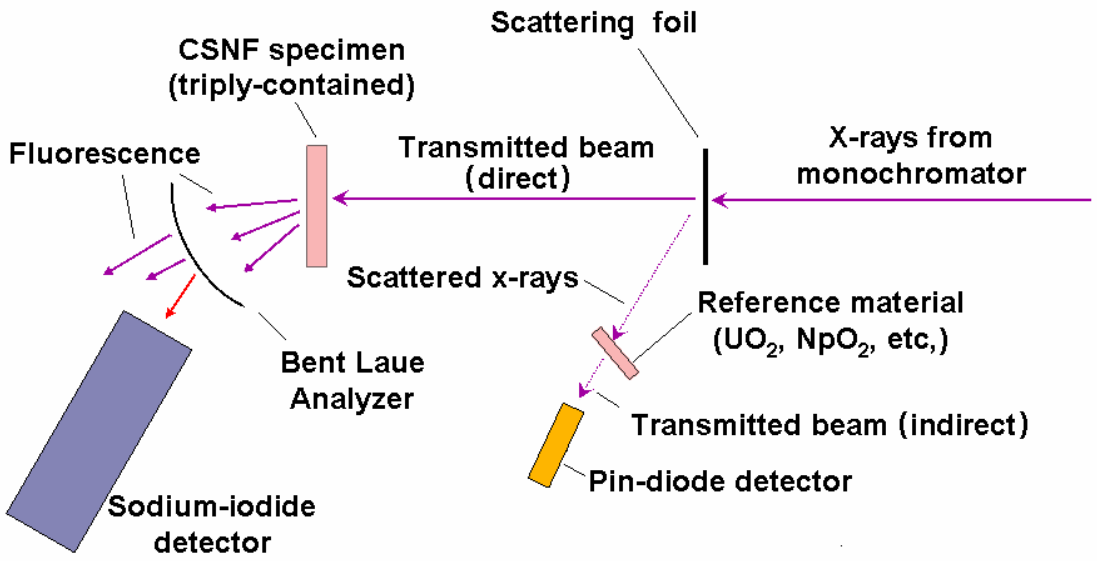

Figure 2.12. Schematic of X-Ray Absorption Experiment Configuration at the APS, Showing Position of Detectors and Reference Materials. The sodium iodide detector (or solid-state germanium detector, which can also be used) is calibrated by replacing the specimen with a NIST SRM, which contains at least one element in common with the specimen. The pin-diode (p/n semiconductor junction) detector uses non-specular scattered x-rays in transmission mode to identify the energy of the absorption edge of a secondary reference material (e.g., uranium or neptunium oxides), serving as a fixed energy reference during data collection from the specimen.

To achieve the high sensitivity and energy resolution required to record trace neptunium spectroscopy from a uranium oxide (CSNF) matrix, a cryogenically cooled double-crystal Si(111) x-ray monochromator was used along with a focusing harmonic rejection mirror (rhodium coating) to help eliminate higher-order insertion device beam harmonics. A tunable, x-ray-generating insertion device ("undulator") was run with a narrow gap using the 3rd harmonic. Rhodium-coated, 200-mm-long Kirkpatrick-Baez (K-B) mirrors were used to focus the beam to a spot size of approximately 5 micrometers. The combination of the three mirrors set with critical energies near 22 keV combined to ensure minimal harmonic content in the probe beam.

Measuring the L-edge fluorescence X-ray absorption fine-structure (XAFS) in a mixed actinide specimen requires excellent energy resolution, as the Lα1 fluorescence lines for U, Np, and Pu are separated by only approximately 350 eV; the Lα2 lines are separated by less than 150eV from neighboring Lα1 lines. The required energy resolution is achieved using a bent silicon wafer in the Laue geometry (bent Laue analyzer). An array of five bent Laue analyzers was distributed around the sample to collect fluorescence from the different elements (Figure 2.13). The energy resolution of the analyzers ranged from 25 eV (for one Sr Kα1 fluorescence analyzer) to 105 eV for the larger-area analyzer optimized for Np Lα fluorescence.

Sample mounts for XAS at the APS were prepared from "106 H core-2" taken from the ATM-106 high-drip-rate 10-year test. The specimen was oriented such that the plane of the x-ray beam from the synchrotron with the normal of the specimen surface lay parallel to the fuel/alteration layer interface in order to minimize signal contribution from material not targeted, thus effectively sharpening the resolution of a scan across the interface. X-ray fluorescence mapping, edge spectroscopy, and line scans were used to investigate the distribution of uranium, neptunium and plutonium across the interface. Additional data, including detailed line scans and x-ray absorption spectra, were collected.

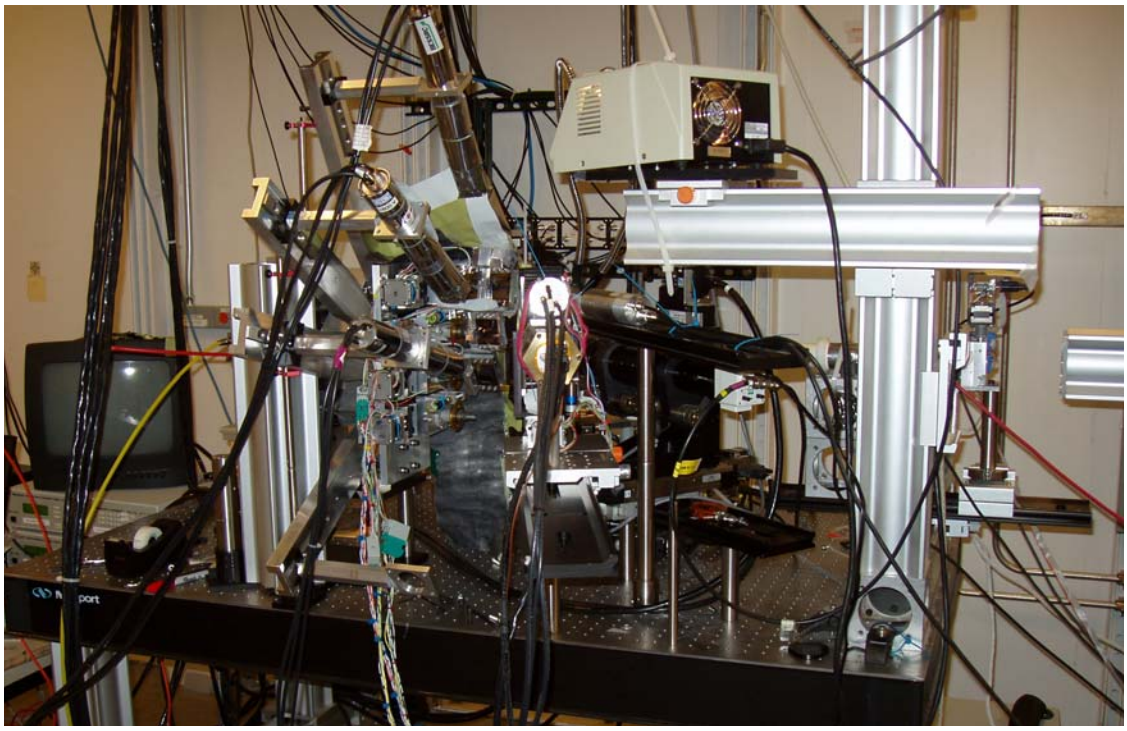

Figure 2.13. Photograph of the Detector Array Surrounding the Sample Position

Figure 2.14 shows x-ray spectral maps of uranium with plutonium and plutonium with strontium, along with a scaled SEM image for reference. The bright triangular region (unaltered fuel) is clearly correlated strongly with higher plutonium abundance in the two x-ray images, while the sharp boundary between the fuel and corrosion layer exhibits a high concentration of strontium (in blue, middle image), indicating that some Sr may be sequestered in minerals formed at the interface. The relative concentrations of the plutonium and strontium compared with the uranium are up to 2 atomic % Pu and 4 atomic % Sr (at the interface), while the background Sr concentration is less than 1 atomic %. It should be noted that the "EJ-13" groundwater used in the Argonne tests in which the fuels were reacted contained about 30 ng/mL of natural strontium, so the Sr in the layer may not be radiogenic. It could, however, indicate a region of β-uranophane [$Ca(UO_2)_2(SiO_3OH)_2(H_2O)_5$], where Sr would readily substitute for Ca, underlying the structurally related Na/K-boltwoodite (Finch et al. 1999).

A closer look at the x-ray spectral intensities across the interface region shows a slight increase in the neptunium and plutonium concentration within a 20-micrometer-wide zone at the corrosion front (Figures 2.14 through 2.17). While subtle, this effect appears to be consistent across much of the interface in this sample (Figures 2.15 and 2.17 are from different line scans across the interface). This level of enrichment, along with the thickness of the enriched zone (compared with the total amount of fuel altered) is not, by itself, enough to account for all of the Np that was originally present in the spent fuel that has been altered. The Np abundance in the pristine material is about 1 atom per 1000-2000 atoms of uranium, while in the corrosion layer, the Np abundance drops to lower than 1 atom per 7,000 atoms of uranium. Note, however, that neptunium and plutonium are detectable well into the uranyl-silicate alteration layer (Figures 2.15 and 2.17).

The oxidation state is determined by examining the shape of the near-edge features of the absorption edge of U or Np (Figure 2.16). Particularly, the relative height of the sharp "white line" edge to the jump height varies between the U(IV) and U(VI) species and similarly with the Np(IV) and Np(V) species. Also, the presence of a high-energy spectral shoulder on the white line peak is characteristic of the *trans* dioxo-cation structure common to both uranyl- and neptunyl- species (Conradson 1998). Both the Pu and the Np concentrations are strongly correlated to the uranium oxidation state (Figures 2.15 through 2.17), which has been estimated by comparing the white line intensity with the jump height in the uranium spectra in Figures 2.15 and 2.17. This trend of Pu and Np concentration diminishing in regions of more oxidized uranium is in general agreement with previous examination of corroded fuel specimens using x-ray spectroscopy and electron microscopy (Argonne 2005). Of particular note is the persistence of a weak neptunium signal (~20% of the Np:U ratio found in the fuel) well into the alteration layer, which exhibits a purely U(VI) character. Notice that the range of the scans from the location in the fuel at "3100" to that in the alteration layer at "3270" (relative positions in micrometers) in Figures 2.14 through 2.16 extends at least 50 micrometers into the alteration layer. Figure 2.17 shows similar data from a different line scan across the fuel/alteration zone interface. Although the spectra in Figure 2.17 have poorer counting statistics than those in Figure 2.16, they are included to illustrate that these observations are representative and reproducible.

(a)

(b)

(c)

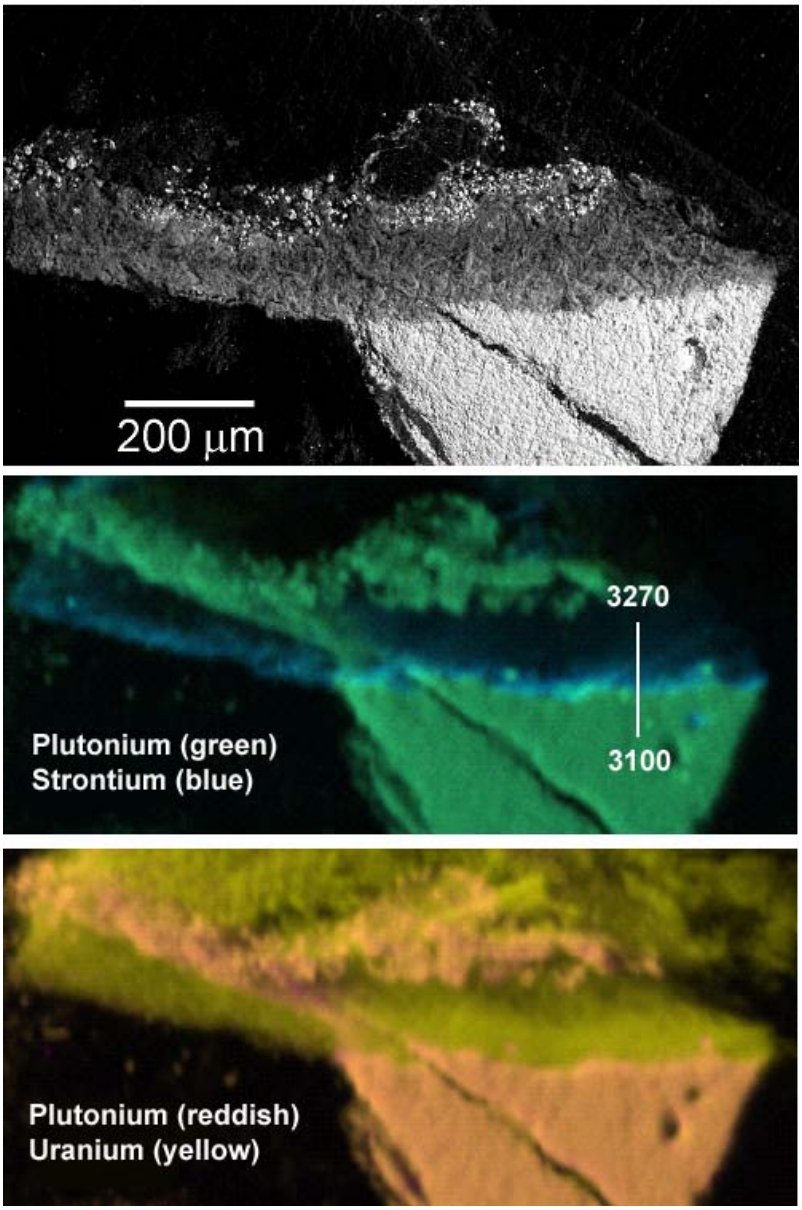

Figure 2.14. SEM Image (from Figure 2.9a) of the ATM-106 Core-2 Sample with Fluorescence Mapping of U, Pu, and Sr Using X-Rays. The bright triangular region of unaltered fuel in (a) is correlated strongly with higher plutonium abundance in the lower two x-ray images (b and c), while the sharp boundary between the unaltered fuel and corrosion layer exhibits a high concentration of strontium (b), indicating that some Sr may be sequestered in minerals formed at the reduction potential of the interface. The relative concentrations of the plutonium and strontium compared with the uranium are up to 2 at% Pu and 4 at% Sr (at the interface), while the background Sr concentration is less than 1 at%. The white line in (b) indicates the position of the line scan described below (Figure 2.15).

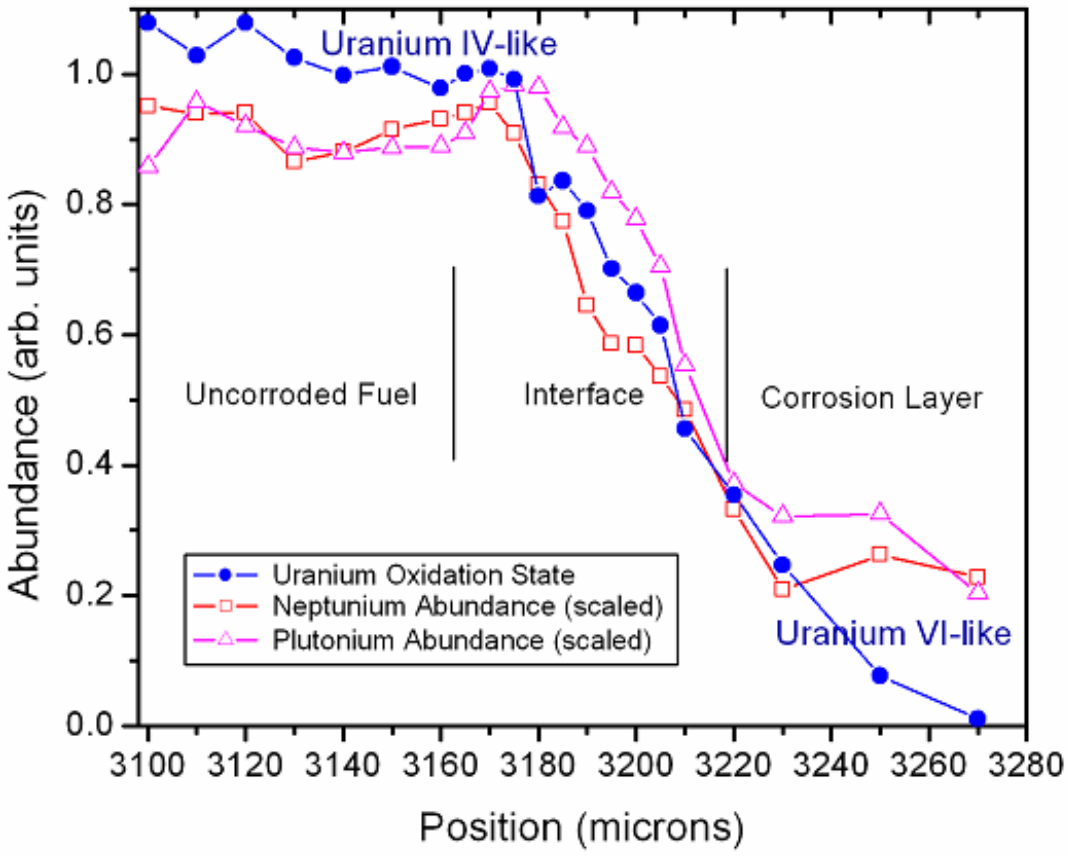

Figure 2.15. XAS Line Scans of Neptunium and Plutonium Abundance (scaled to uranium) along with Uranium Oxidation State across the Reaction Front, Showing Distinct Evidence of a Weak, Yet Fairly Broad (~20 micrometer) Zone that is Enriched in Neptunium and Plutonium. The location of the line scan is indicated in Figure 2.14 (b). The enrichment of neptunium and plutonium occurs near the onset of a transition from quadravalent uranium [U(IV)] in the fuel to hexavalent uranium [U(VI)] that characterizes the alteration rind. Note that neptunium and plutonium are detected well into the alteration rind. The findings provide further evidence that redox conditions near the corroding fuel surface control neptunium (and plutonium) oxidation and dissolution. Representative individual spectra of neptunium and uranium appear in Figure 2.16.

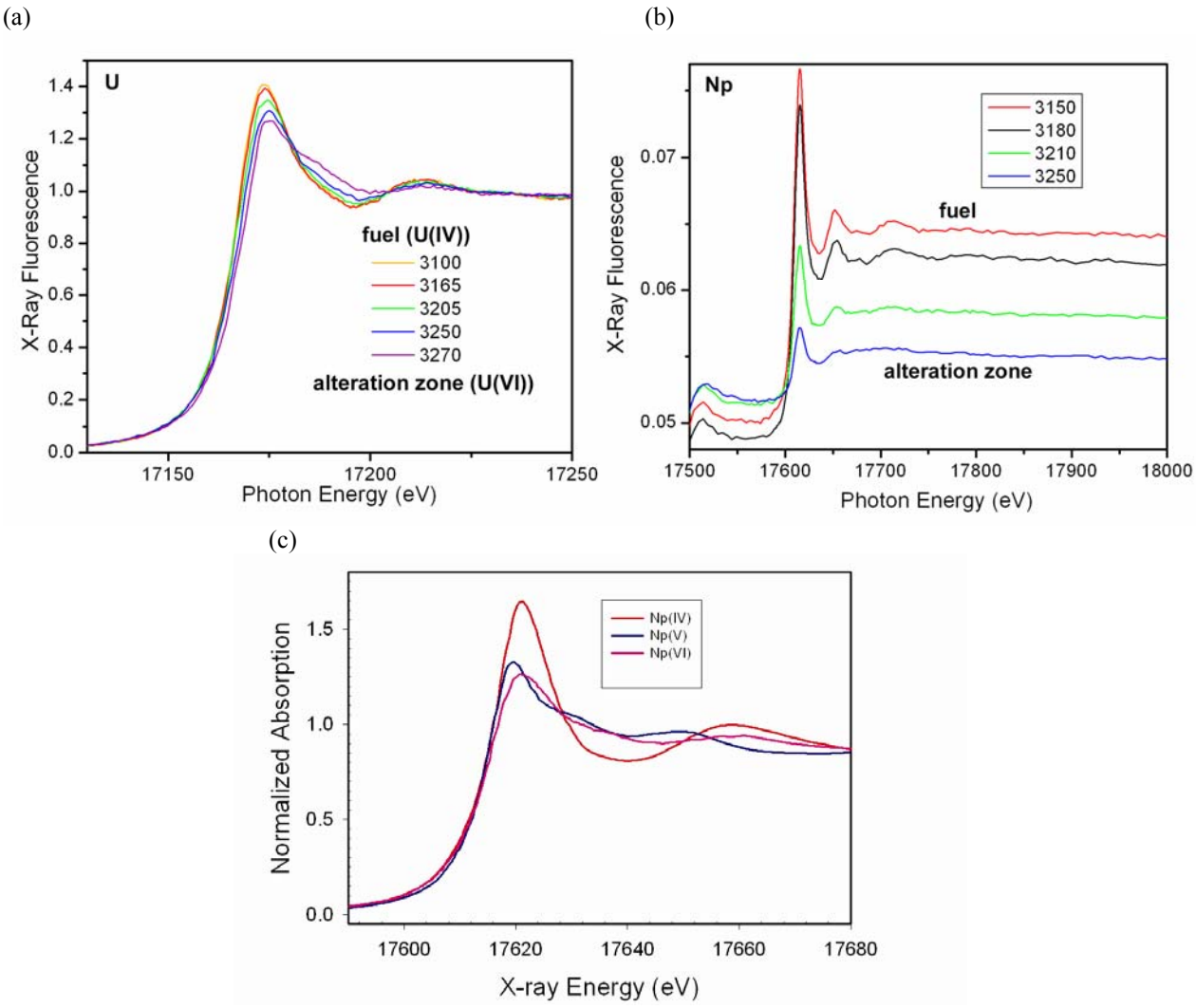

Figure 2.16. Uranium, Neptunium, and Reference Np Spectra. (a) Uranium Spectra Taken at Points across the Fuel/Alteration Zone Interface. The relative position (in micrometers) is indicated by the numerical labels in the key, with higher values toward the alteration zone (corresponding to position in Figure 2.15). Note the qualitative changes in the spectral shape. (b) Neptunium spectra taken at points across the fuel/alteration zone interface. The relative position is indicated as in Figure 2.15. Although the intensity of the Np signal is dropping, there are minimal qualitative changes in its shape. (c) Reference Np spectra ($Np(IV)F_4$, $Np(V)O_2^+{}_{aq}$, and $Np(VI)O_2^{2+}{}_{aq}$) showing the effect of the oxidation state on the near edge structure.

(a)

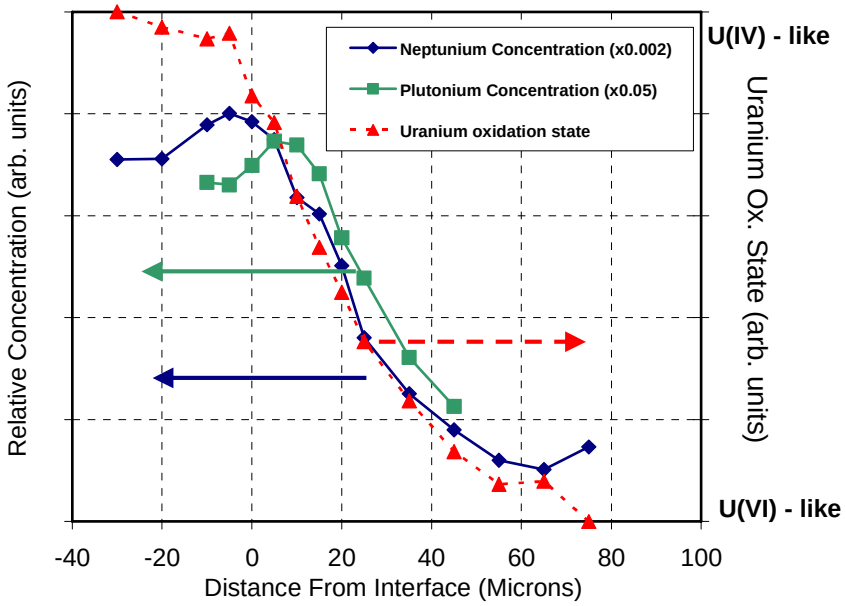

(b)

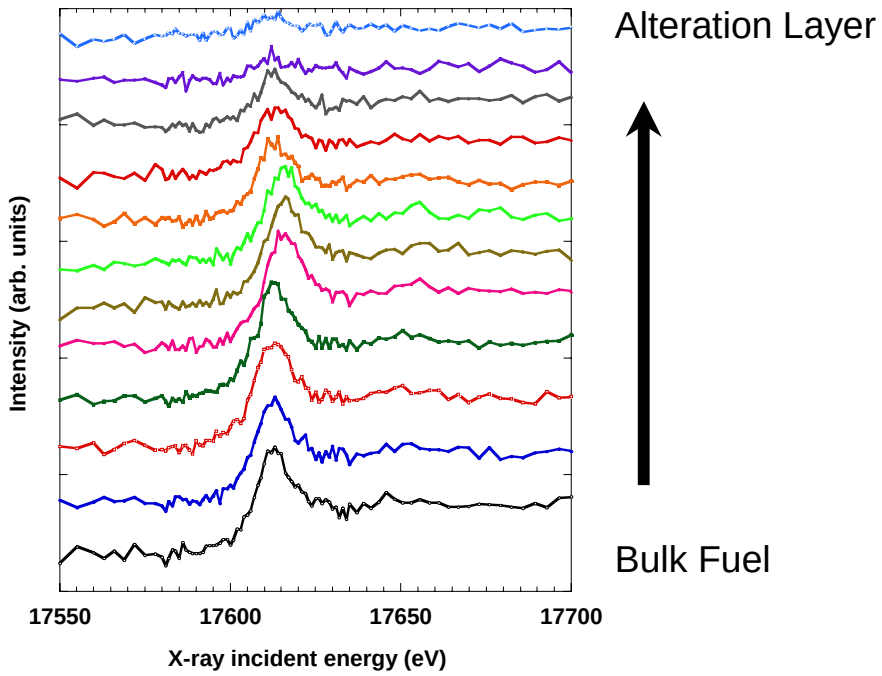

Figure 2.17. (a) XAS Line Scans of Neptunium and Plutonium Abundance (scaled to uranium) along with Uranium Oxidation State across the Reaction Front (compare Figure 2.15, from a different scan location). (b) Raw Np L_{III} absorption spectra from various points across the interface.

No qualitative change is seen in the shape of the neptunium spectra (Figures 2.16 and 2.17), which remain consistent with a +4 oxidation state within the fluorite (UO_2) crystal structure of the fuel (Kropf et al. 2005), although the intensity of the spectrum decreases (reduced relative concentration) in the altered zone. This is consistent with, and indeed is supportive of, the hypothesis that Np(IV) will not be oxidized to Np(V) at the corrosion potential of the fuel (effectively, the U(IV)/U(VI) redox couple). This is the most likely explanation of the relatively low release rates of neptunium observed during testing, and supports the use of NpO_2 as a solubility-controlling phase in dissolved concentration models (Sassani, Van Luik, and Summerson 2006). Note that it is not possible to assign an unambiguous oxidation state to the weaker signals in spectra taken in the alteration zone, where one would expect to find Np(V) if Np had indeed been incorporated into uranyl phases (Burns, Ewing, and Miller 1997; Burns, Deely, and Skanthakumar 2004).

2.4 DISCUSSION

An examination of CSNF that had undergone up to 10 years of corrosion testing has provided valuable insights into mechanisms of radionuclide release and sequestration (particularly for Np and Pu). Corrosion fronts have been found to follow the contours of exposed geometric surfaces, with little apparent effect from grain boundary penetration. This observation supports use of the geometric surface area of fuel fragments to scale the corrosion rate data from laboratory experiments to the repository. The important radioelements neptunium and plutonium have been found to exist in the +4 oxidation state in the unaltered fuel, in solid solution with the fluorite crystal structure of UO_2. Across the corrosion layer in the altered fuel, Np and Pu are found to be slightly enriched in abundance near the surface of the corroding fuel, while remaining in the +4 oxidation state even as the uranium is oxidized. Uranyl alteration products are found to be depleted in neptunium relative to the original fuel (the Np:U in the layer is about 20% or less of that found in the fuel) and nearly devoid of plutonium. These results are consistent with the hypothesis that neptunium, which is resistant to oxidation relative to uranium, is not oxidized as the fuel corrodes and behaves as if NpO_2 is the solubility-controlling phase. Although coprecipitation of Np with uranyl phases as an important sequestration mechanism is not ruled out by these observations, it appears that the relative stability of Np(IV) solids at the corrosion potential of oxidizing UO_2 is controlling Np release. Nonetheless, the evidence is pointing toward a model based upon NpO_2 as a solubility-limiting phase, at least while fuel (or a similar redox couple) is present.

Several important observations potentially related to uncertainties, validations, and conservatisms in current models (BSC 2004) have been reported:

- The CSNF samples were observed to corrode in such a manner that the corrosion front follows the geometric contour of the fuel surface, rather than via (for instance) preferential grain boundary attack. This supports current estimates of the corroding CSNF effective surface based upon geometric surface area of fuel pellet fragments.

- It was observed that neptunium and plutonium concentrations in corroded CSNF samples were somewhat higher at and near the corrosion front (i.e., the interface

between the alteration product "rind" layer and the underlying fuel) than in the bulk fuel.

- The neptunium and plutonium were found in the quadravalent (4+) oxidation state, extending into the enrichment zone and the uranyl alteration layer.

- The uranyl phases that constitute most of the alteration rind were depleted in neptunium relative to the bulk fuel. Neptunium concentrations in the uranyl alteration rind were less than 20% of that in the parent fuel.

This work addresses the technical basis for the assumption that the dissolved Np concentration is controlled by NpO_2 rather than the more conservative assumption that Np_2O_5 controls the dissolved concentration. Coprecipitation models (in which neptunium is sequestered in precipitated uranyl phases) are not precluded by the data presented herein, because neptunium resisted oxidation in these tests and thus may have been present at low concentrations in the solutions from which the uranyl phases had precipitated.

2.5 REFERENCES FOR SECTION 2

Argonne (Argonne National Laboratory), "Yucca Mountain Project, FY 2004 Annual Report for Waste Form Testing Activities," ANL-05/08, Argonne, Illinois (2005).

BSC (Bechtel SAIC Company), "CSNF Waste Form Degradation: Summary Abstraction," ANL-EBS-MD-000015 REV 2, Las Vegas, Nevada, Bechtel SAIC Company (2004) DOC.20040908.0001.

BSC, "Technical Work Plan for Waste Form Testing," TWP-WIS-MD-000018 REV 00, Las Vegas, Nevada, Bechtel SAIC Company, LLC (2005).

P. C. Burns, R. C. Ewing, and M. L. Miller, "Incorporation Mechanisms of Actinide Elements Into the Structures of U6+ Phases Formed During the Oxidation of Spent Nuclear Fuel," Journal of Nuclear Materials **245**(1), 1-9 (1997).

P. C. Burns, K. M. Deely, and S. Skanthakumar, "Neptunium Incorporation into Uranyl Compounds That Form as Alteration Products of Spent Nuclear Fuel: Implications for Geologic Repository Rerformance," Radiochimica Acta **92**, 151-159 (2004).

S. D. Conradson, "Application of X-ray Absorption Fine Structure Spectroscopy to Materials and Environmental Science," Applied Spectroscopy **52**(7), 252A-279A (1998).

P. Dehaudt, "State of the Art of the Oxidation of Spent Nuclear Fuel," Section 7.2 of *Synthesis on the Long Term Behavior of the Spent Nuclear Fuel*, C. Poinssot, C., ed., CEA-R-5958(E),Volume II, Commissariat à l'Énergie Atomique, Paris, France (2001).

R. J. Finch, "Unsaturated Testing of Bare Spent UO_2 Fuel Fragments," Data Report YMP/SF-3A-455, Chicago, Illinois: Argonne National Laboratory, Argonne, Illinois (2003). MOL. 20040129.0324.

R. J. Finch, "Precipitation of Crystalline NpO_2 During Oxidative Corrosion of Neptunium-Bearing Uranium Oxides," Scientific Basis for Nuclear Waste Management XXV, B. P. McGrail and G. A. Cragnolino, eds., Materials Research Society Symposium Proceedings **713**, 639-646 (2002).

R. J. Finch, E. C. Buck, P. A. Finn, and J. K. Bates, "Oxidative Corrosion of Spent UO_2 Fuel in Vapor and Dripping Groundwater at 90°C." Scientific Basis for Nuclear Waste Management XXII, MRS Symposium Proceedings 556 D. J. Wronkiewicz and J. H. Lee, eds., 431-438, Materials Research Society, Warrendale, Pennsylvania (1999). TIC: 246426.

J. A. Fortner, R. J. Finch, A. J. Kropf, and J.C. Cunnane, "Re-evaluating Neptunium in Uranyl Alteration Phases from Corroded Spent Fuel," Nuclear Technology **148** (2) 174-180 (2004).

M. Goldberg, "Rod Segment Test Data Report, CSNF Degradation Model: Q Data Input from ANL Testing," Task Number: PAWC1M5. [Argonne, Illinois]: Argonne National Laboratory, Argonne, Illinois (2003). ACC: MOL.20030627.0221.

B. Grambow, A. Loida, A. Martinez-Esparza, P. Diaz-Arocas, J. de Pablo, J. L. Paul, G. Marx, J. P. Glatz, K. Lemmens, K. Ollila, and H. Christensen, "Long-Term Safety of Radioactive Waste Disposal: Source Term for Performance Assessment of Spent Fuel as a Waste Form, Final Report," FZKA 6420, Forchungszentrum Karlsruhe, Technik und Umwelk, Forschungszentrum Karlsruhe GmbH Karlsruhe, Germany (2000).

R. J. Guenther, D. E. Blahnik, T. K. Campbell, U. P. Jenquin, J. E. Mendel, L. E. Thomas, and C.K. Thornhill, Characterization of Spent Fuel Approved Testing Material ATM--103, PNL-5109-103, Pacific Northwest Laboratory, Richland, Washington (1998a). ACC: NNA.19911017.0104.

R. J. Guenther, D. E. Blahnik, T. K. Campbell, U. P. Jenquin, J. E. Mendel, and C. K. Thornhill, "Characterization of Spent Fuel Approved Testing Material--ATM-106," PNL-5109-106, Pacific Northwest Laboratory, Richland, Washington (1998b). NNA.19911017.0105.

J. P. Kaszuba and W. H. Runde, "The Aqueous Geochemistry of Neptunium: Dynamic Control of Soluble Concentrations with Applications to Nuclear Waste Disposal," Environmental Science and Technology **33**(24), 4427-4433 (1999).

H. Kleykamp, J. O. Paschoal, R. Pejsa, and F. Thommler, Journal of Nuclear Materials **130,** 426-433 (1985).

A. J. Kropf, J. A. Fortner, R. J. Finch, J. C. Cunnane, and C. Karanfil, 2005, "A Bent Silicon Crystal in the Laue Geometry to Resolve X-ray Fluorescence for X-ray Absorption Spectroscopy," Physica Scripta **T115**, 998–1000 (2005).

R. J. Lemire, “An Assessment of the Thermodynamic Behavior of Neptunium in Water and Model Groundwaters from 25 to 150°C,” AECL-7817, Whiteshell Nuclear Research Establishment, Pinawa, Atomic Energy of Canda, Limited, Pinawa, Manitoba, Canada (1984).

D. C. Sassani, A. Van Luik, and J. Summerson, “Neptunium Solubility in the Near-Field Environment of a Proposed Yucca Mountain Repository,” Scientific Basis for Nuclear Waste Management XXIX, MRS Symposium Proceedings, P. Van Iseghem, ed., **932.,** 991-998, Materials Research Society, Warrendale, Pennsylvania (2006).

D. W. Shoesmith, “Fuel Corrosion Processes Under Waste Disposal Conditions,” Journal of Nuclear Materials **282**, 1-31 (2000).

L. E. Thomas and R. J. Guenther, "Characterization of Low-Gas-Release LWR Fuels by Transmission Electron Microscopy," Materials Research Society Symposium Proceedings **127**, 293-300 (1989)

S. Vaidyanathan et al., “High Burnup BWR Fuel Pellet Performance,” Proceedings of the 1997 International Topical Meeting on LWR Fuel Performance, 471-477 (1997).

3. Np(V) PRECIPITATION KINETICS IN HOMOGENEOUS AND HETEROGENEOUS SYSTEMS
(W. L. Ebert and A. V. Guelis)

This Task was conducted to better understand the kinetics of NpO_2 precipitation from a super-saturated solution of Np(V) in homogeneous and heterogeneous systems. Although thermodynamics indicates that NpO_2 is more stable than Np_2O_5 under most repository conditions (e.g., Kaszuba and Runde 1999), uncertainties in the database make the identification of either phase as the solubility-controlling phase tenuous. The phase selected as the solubility-controlling phase is very important, as dissolved concentrations calculated in the "Dissolved Concentration Limits of Radioactive Elements" model (BSC 2005a) based on NpO_2 are about 20-times lower than those calculated based on Np_2O_5. Experiments at ≤90ºC have shown the formation of Np(V)-bearing solids (e.g., Np_2O_5) to be kinetically favored in homogeneous systems (Efurd et al. 1998), although NpO_2 has been observed to form from Np(V)-bearing solutions at 200ºC (Roberts et al. 2003) and higher temperatures (this work). This suggests that the formation of NpO_2 may be kinetically inhibited at lower temperatures, either by direct precipitation or transformation of Np_2O_5. This hypothesis is supported by the observation that NpO_2 precipitates at ambient temperatures in the presence of UO_2 (this work), presumably because the oxidation of U^{4+} to UO_2^{2+} can reduce NpO_2^{+} to Np^{4+}, so that NpO_2 can precipitate without the initial formation of Np_2O_5. This work was performed under Test Plan ANL-TP-05-001 (Rev. 0 and Rev. 1) as part of the BSC Technical Work Plan for Waste Form Testing, TWP-WIS-MD-000018 REV 00 (BSC 2005b).

The current TSPA model uses NpO_2 as the solubility-limiting phase within a breached waste package under most conditions ($NaNpO_2CO_3$ is used at high pH and low Eh values). The model is based on the assumption that, although the precipitation of NpO_2 is expected to be sluggish at temperatures below about 200ºC, the presence of UO_2 (spent fuel) and perhaps steels will facilitate its formation. In the model, the maximum dissolved Np concentration does not depend on temperature or time. The objective of this Task is to provide experimental data to support (or refute) the assumptions that underlie the use of NpO_2 as the solubility-limiting phase in the Np dissolved concentration limit model. Specifically, tests were conducted to confirm that NpO_2 can form from a Np(V)-bearing solution in a homogeneous system at 200ºC and to measure the precipitation rates at 150, 200, 240, and 280ºC. The intent of those tests was to estimate an effective activation energy and assess the likelihood that NpO_2 will precipitate even in the absence of reducing agents such as UO_2 and steels and continue to control the dissolved Np concentration. This may be important for very long disposal times after the fuel has been completely dissolved and can no longer facilitate the formation of NpO_2. Although the rate that is predicted at ambient temperature by extrapolation of rates measured at near 200ºC is highly uncertain, it provides some insight into whether the current assumption that the formation of NpO_2 can occur at a non-negligible rate over repository time scale (and in preference to the formation of Np_2O_5) is reasonable. Solids formed in those tests, including solids suspended in the test solution, were analyzed to determine the Np oxidation state and the phase composition. Additional tests were designed to study the effectiveness of UO_2 and various steels in catalyzing the precipitation of NpO_2 (or Np_2O_5) at ambient temperatures; however, except for one test with

UO_2, those tests have not yet been conducted due to a stop-work order that was issued by BSC related to consumable chemicals and standards.

3.1 BACKGROUND

Released ^{237}Np is predicted to be a major contributor to the radiation dose from the Yucca Mountain repository at times beyond about 50,000 years. Although it is not abundant in spent fuel initially, ^{237}Np will accumulate over time as a decay product of ^{241}Am ($t_{1/2}$ = 432.7 years). ^{237}Np itself has a half life of 2.14×10^6 years. Whereas Np exists in the Np(IV) oxidation state in the fuel and NpO_2 is expected to form on the fuel surface, the Np in near-neutral air-saturated aqueous solutions will exist primarily in the Np(V) oxidation state as the mobile neptunyl ion NpO_2^+. Depending on the solution chemistry and conditions, various oxide, hydroxide, or carbonate solid phases can precipitate from a solution containing Np(V), although thermodynamic calculations indicate that these Np(V)-bearing solids are all less stable (more soluble) than NpO_2 under most of the range of repository conditions being considered in TSPA (Kaszuba and Runde 1999). The dissolved concentration limits established by NpO_2 are significantly lower than those established by any of the Np(V)-bearing phases that could form under various conditions. Whether or not NpO_2 can control the dissolved concentrations of Np(V) species remains a key uncertainty. Obviously, the formation of NpO_2 in a solution of Np(V) requires the reduction of Np(V) to Np(IV). The reduction step is sluggish at low temperatures (<200ºC) but can be catalyzed in the repository by reducing agents such as the U(IV) in spent fuel. The impact of the different Np concentration limits established by various phases on performance assessment calculations is significant, as summarized in the following paragraphs.

For a 1992 assessment (Barnard et al. 1992), dissolved ^{237}Np concentrations were assigned very low values, on the order of 1×10^{-8} M, based on the results of spent nuclear fuel dissolution studies (e.g., Wilson and Burton 1989; Wilson 1990a, 1990b). The total radiation doses calculated with those low dissolved concentrations were well within regulatory limits. Subsequent experiments were conducted to supplement the database used for the calculations and identify the solubility-controlling phase(s). In those experiments, saturation was approached from supersaturated solutions that were maintained at pH values of 5.9, 7.0, and 8.5 at 25, 60, or 90ºC. Crystalline sodium neptunyl(V) carbonates, $Na_{2x-1}NpO_2(CO_3)_x \bullet nH_2O$, were identified as the solid phases formed under most test conditions; Np_2O_5(cr) was detected in experiments conducted at 90ºC in pH 5.9 and pH 7.0 solutions. This series of tests yielded significantly higher steady-state Np concentrations than those used in the 1992 assessment, with values up to 6×10^{-3} M in tests at pH 5.9 and 60ºC (Nitsche et al.1993a, 1993b). These phases are not expected to control the Np concentrations over long times, however, because equilibrium calculations (at 25ºC) have shown that NpO_2 is the thermodynamically favored phase in J-13 and UE-25p#1 groundwaters under most Eh-pH conditions (Kaszuba and Runde 1999). The phases formed in the tests by Nitsche et al. (1993b) are expected to be replaced by NpO_2 over time. In the absence of NpO_2, the stable solids phases were predicted to be Np_2O_5 under oxidizing conditions and $Np(OH)_4$ under more reducing conditions. "Increasing the redox potential to approximately 0.25 V favors the successive formation and increasing predominance of Np(V) in solutions while maintaining Np(IV) in the solid state" (Kaszuba and Runde 1999). (All voltages given herein are reported relative to the standard hydrogen electrode.) Tuff groundwater from

well J-13 is near-neutral and measured redox potentials range from about 0.10 to 0.43 V. In the "In-Package Chemistry Abstraction AMR (BSC 2005c), the *Eh* (electron activity in volts) is modeled to vary with the pH, temperature, and partial pressure of oxygen as

$$Eh = \frac{2.303\ RT}{F}\left[\frac{6193.973}{T} - pH + 0.25 \log P_{O_2}\right], \tag{3.1a}$$

where F is the Faraday constant (23.06 kcal/volt-gram equivalent), T is absolute temperature (Kelvin), and P_{O_2} is the partial pressure of oxygen (BSC 2005c, Table 6-25). At a temperature of 90ºC and an oxygen pressure of 0.2 bar (0.1974 atm), the range of *Eh* values is 0.892 – 0.604 V over the pH range of 4.5 to 8.5 that is specified in the "In-Package Chemistry Abstraction." The *Eh* value is calculated in the "Dissolved Concentration Limits of Radioactive Elements" model with the expression (BSC 2005a, Eq. 6.5-7):

$$Eh = 1.10 - 0.0592\ pH\ . \tag{3.1b}$$

This equation does not take into account the effects of temperature and oxygen explicitly, and gives a slightly lower range of *Eh* values over this pH range (namely, 0.835 – 0.599 V) than the equation given in the "In-Package Chemistry Abstraction." The discrepancy between Equations 3.1a and 3.1b becomes greater at lower temperatures and higher oxygen pressures. Nevertheless, both models indicate oxidizing environments.

The absence of NpO_2 in the experiments of Nitsche et al. (1993a, 1993b) was probably due to kinetic limitations on its formation and the relatively short test durations (a few months). It is also likely that those results were affected by the high sodium concentrations that resulted from titrating the solutions to maintain constant pH values – i.e., the predominant solid phases were sodium neptunyl carbonates. Similar tests in which the Na^+ was kept low resulted in a lower range of steady-state values for the Np solubility: from 6 x 10^{-6} M at pH 8.5 and 90ºC to 9 x 10^{-4} M at pH 6.0 and 60ºC (Efurd et al. 1998), and the solid phases in those experiments were identified as $Np_2O_5 \bullet nH_2O$(cr). Although the new results gave slightly lower steady-state concentrations, the Np concentration was still controlled by a Np(V)-bearing solid rather than NpO_2, even after equilibration times of about 425 days.

Roberts and co-workers conducted tests at 200ºC in an effort to promote the precipitation of NpO_2 from a supersaturated solution (Roberts et al. 2003). Tests were conducted using a 1 x 10^{-4} M Np(V) solution that had been adjusted to pH 6. This solution was presumed to be saturated with respect to NpO_2 but undersaturated with respect to $Np_2O_5 \bullet nH_2O$ (cr) to prevent its precipitation. The dissolved Np(V) concentration decreased within the first sampling interval (after 5 days) and steady-state was reached after about 60 days. Analysis of the resulting solids revealed NpO_2(cr) had formed, but no Np(V) solids were detected. The decreases in the aqueous Np concentrations observed over time were accompanied by decreases in the pH, as they had expected based on the reaction in Equation 3.2a:

$$NpO_2^+(aq) + 0.5\ H_2O \leftrightarrows NpO_2(cr) + H^+(aq) + 0.25\ O_2(g). \tag{3.2a}$$

This can be obtained as the net reaction for precipitation and reduction steps

$$NpO_2^+(aq) + 0.5\ H_2O \leftrightarrows Np_2O_5(cr) + H^+(aq) \quad (3.2b)$$

and

$$Np_2O_5(cr) \leftrightarrows NpO_2(cr) + 0.25\ O_2(g), \quad (3.2c)$$

respectively.

The reduction of Np_2O_5 to NpO_2 (Equation 3.2c) is thermodynamically favorable under Yucca Mountain conditions, and the precipitation reaction in Equation 3.2b is known to occur (Efurd et al. 1998). This suggests that NpO_2 could form in repository environments after long times when ^{237}Np becomes a major dose contributor, depending on the kinetics of the reaction in Equation 3.2c.

It is important to note that the experiments to measure Np solubility limits were conducted using **homogeneous** systems that excluded the effects of various solids that will be present in a disposal container. The precipitation of NpO_2 has been observed in a **heterogeneous** system in which $Np_{0.33}U_{2.67}O_8$ was corroded in humid air at 90 and 150°C (Finch 2002). The oxidation of U(IV) to U(VI) catalyzed the reduction of Np(V) to Np(IV) according to the thermodynamically favorable reaction in Equation 3.3a:

$$2NpO_2^+ + U^{4+} + 4H^+ \leftrightarrows 2\ Np^{4+} + UO_2^{2+} + 2H_2O \qquad E^o = 0.405 \text{ to } 0.469V, \quad (3.3a)$$

which can then precipitate according to Equation 3.3b:

$$Np^{4+} + 2\ H_2O \leftrightarrows NpO_2(cr) + 4\ H^+. \quad (3.3b)$$

(The reported range in E^o reflects current uncertainties in the U and Np half reactions.) The pair of reactions in Equations 3.3a and 3.3b provide a path to NpO_2 formation that avoids the slow conversion from Np_2O_5. Other interactions could facilitate the reduction of Np(V) to Np(IV) and promote the formation of NpO_2 at low temperatures, such as interactions with steels in the waste package container and internal structures. In that case, the oxidation of iron could catalyze the reduction of Np(V) to Np(IV) in reactions analogous to that in Equation 3.3a. We note that whereas only NpO_2 was detected in tests at 150ºC, similar amounts of NpO_2 and Np_2O_5 were detected in tests at 90ºC (Finch 2002). It is likely that the Np_2O_5 that formed (e.g., by the reaction in Equation 3.2b) will convert to NpO_2 over time (if NpO_2 is truly the thermodynamically stable phase). Because NpO_2 has the same fluorite structure and similar lattice parameters as UO_2, CSNF can also facilitate the nucleation and epitaxial growth of NpO_2.

The current dissolved concentration model for performance assessment calculations uses NpO_2 as the solubility-controlling phase within the waste package under most conditions, except that $NaNpO_2CO_3$ is used at high pH and high $P(CO_2)$ conditions (BSC 2005a). However, Np_2O_5 is used as the base case solubility-controlling solid in the invert, where the dissolved Np(V) is removed from the influence of the waste package and is in a more oxidizing environment.

3.2 APPROACH

This task is divided into two subtasks addressing the kinetics for homogeneous and heterogeneous precipitation.

3.2.1 Subtask (1) Homogeneous Precipitation Kinetics Tests

Tests were conducted at 150, 200, 240, and 280ºC following the same methodology used by Roberts et al. (2003). The tests were conducted using Parr Instruments™ high-pressure vessels in which borosilicate glass, quartz, or PTFE Teflon containers (liners) were placed to hold the solution and prevent Np from contacting the steel vessel, which could reduce it to Np(IV). The same stock solution (an approximately 1 x 10^{-4} M Np solution that was adjusted to pH 6.0) was used for all tests. This solution was similar to the solution used by Roberts et al., and is undersaturated with respect to the Np(V) phases that were found to have formed in previous tests (i.e., in tests by Nitsche et al. 1993a and by Efurd et al. 1998), but believed to be supersaturated with respect to NpO_2. Tests were static (i.e., the solutions were not agitated during the tests) and were conducted in ovens set at the appropriate temperatures. The tests were interrupted after several test durations to remove small samples of the test solution for analysis of the pH and Np content (with gamma spectroscopy). These are referred to as serially sampled tests. The Np content was tracked over time to assess the extent of the homogeneous nucleation and precipitation, and precipitated solids were collected at the end of the test. The precipitates from some tests were analyzed using transmission electron microscopy (TEM) and/or with X-ray absorption near edge structure (XANES) and extended X-ray absorption fine structure (EXAFS) spectroscopies to determine the oxidation state of Np in the phases that formed (e.g., NpO_2 or Np_2O_5). A separate series of batch tests was conducted at 200ºC to evaluate the impact of interrupting tests to sample the solution on the precipitation rate. These tests were conducted in Parr Instrument Company model 4749 steel digestion vessels with PTFE Teflon liners. The completed test matrix for the serially sampled homogeneous precipitation kinetics tests is shown in Table 3.1. The serially sampled tests were initially run using borosilicate glass liners; however, corrosion of the glass liners at high test temperatures resulted in a significant increase in the pH and the generation of an abundance of silica colloids. Tests with borosilicate glass liners were halted and new tests were started using quartz liners. Several preliminary TEM and X-ray studies were conducted with solids recovered from tests conducted in borosilicate glass liners, and those results are included in this report as added insight into the Np precipitation behavior.

The neptunium starting solution was purified using an anion exchange method. An initial solution was prepared using a solution of H_2O_2 in approximately 8 M HNO_3. The resulting solution was passed through an anion exchange column containing resin AG-1 (Bio-Rad) to sorb the $Np(NO_3)_6^{2-}$. The column was then washed with a solution of approximately 1% H_2O_2 in approximately 8 M HNO_3. After washing, the column was stripped at 60ºC with a 0.3 M HNO_3 solution, which allows reoxidation to Np(V). The NpO_2^+ thus formed is not retained on the AG-1 anion exchange column and was eluted. This starting solution was used to make the stock solution for the precipitation tests. The Np(V) hydroxide was precipitated as NpO_2OH by mixing with a NaOH solution (0.072 g NaOH was dissolved in 10 g of demineralized water, and then 1 g of the Np(V) solution was added). The grey-green solid that formed was separated by

Table 3.1. Matrix of Tests to Study Homogeneous Precipitation Kinetics (Subtask 1)

Test Number	Liner	Temperature, ºC	Sampling Intervals, days
Serially Sampled Tests			
280-1-1, -2	Borosilicate glass	280	10, 25
240-1-1, -2	Borosilicate glass	240	10, 25
200-1-1, -2, -3	Borosilicate glass	200	6, 29, 56
150-1-1, -2	Borosilicate glass	200	6, 29, 56
Serially Sampled Tests			
280-2-1, -2, -3, -4	Quartz	280	2, 12, 21, 68
240-2-1, -2, -3, -4	Quartz	240	2, 12, 21, 68
200-3-1, -2, -3, -4, -5	Quartz	200	2, 12, 21, 68, 289
150-2-1, -2, -3, -4, -5	Quartz	150	2, 12, 21, 68, 289
Batch Tests			
200-2-1, -2, -3, -4, -5, -6, -7	Teflon	200	2, 8, 17, 23, 30, 45, 71

centrifugation and then washed three times with demineralized water (which had been distilled and filtered through a Milli-Q Plus Water System) to remove any residual sodium nitrate. The solid NpO_2OH was then dissolved in 3 M HCl. The solution was an emerald green color indicative of Np(V). The oxidation state of the dissolved Np was verified using UV/VIS spectrophotometry; a single peak was observed at 980 nm corresponding to Np(V) (Katz, Seaborg, and Morss 1986). The solution was further diluted with demineralized water to generate the stock solution for all tests: the Np concentration in the as-prepared solution was determined to be 3.218×10^{-4} M by gamma spectroscopy. The solution was diluted three-fold with demineralized water to attain a stock solution with the desired concentration near 1×10^{-4} M.

The pH of the diluted solution was measured to be 6.76, and then adjusted to near pH 6 by the addition of 0.004 g NaOH. The concentration of Np in the resulting stock solution was determined by gamma spectroscopy to be 1.023×10^{-4} M (see Appendix A, Section A.1) and the pH was measured to be 6.00 (at room temperature) using a combination electrode that had been calibrated with NIST-traceable buffer standards (see **Note 1**).

[Note 1. A stop work order was issued by BSC on June 1, 2006, in response to Condition Report CR 7875 regarding the used of consumable standards and reagents. The pH buffer standards that were used in this work were not procured directly from the National Institute of Standards and Technology (NIST) and so the results of analyses using these standards remain to be verified.]

The homogeneous precipitation experiments were conducted in stainless steel high-pressure reaction vessels obtained from Parr Instrument Company (Figure 3.1). The Np(V) solutions were contained within a borosilicate glass, quartz, or Teflon liner that was placed in a Parr vessel to prevent Np from contacting the steel vessel. The borosilicate glass liners were procured from Parr Instrument Company and are cylindrical with flat bottoms. The quartz liners were custom-made at Argonne to fit snuggly inside the steel vessel and had rounded

(hemispherical) bottoms. Both the borosilicate glass and quartz liners were open at the top. The Teflon liners were procured from Parr Instrument Company and are 23-mL cups with lids. About 60 mL of the Np stock solution was added initially to the borosilicate liners (about 80 mL was added to the quartz liners and 8 mL was added to the Teflon cups) in each test. The vessels were sealed and then placed in an oven set at 150, 200, 240 or 280°C. Tests were conducted in convection ovens that had been set at the desired temperatures prior to testing. The oven temperatures were monitored continuously with thermocouples that had been calibrated against NIST-traceable mercury thermometers prior to starting the tests. The thermocouple temperatures were recorded every 12 hours by a data logger. After the desired reaction time, a vessel was removed from the oven and allowed to cool to near room temperature before being opened.

The test solution was poured from the liner into a collection bottle, and then an aliquot of the consolidated solution (nominally 2 mL) was removed for analysis. The remaining solution was poured back into the liner in the vessel. The vessel was then re-sealed and returned to the oven. We note that the total vessel mass was not measured before and after the test interval, so any vapor loss during testing and solution lost during the emptying, sampling, and refilling of the test vessel was not accounted for. It is assumed that the mass of solution decreased by amounts equal to the aliquots taken for analysis at each sampling. This adds uncertainty to the concentrations calculated at each sampling. The amount of solution remaining at the end of the test (after all samples were removed) provides some indication of the amounts lost, although the final test interval was considerably longer than the previous intervals.

The test solution collected at each sampling was passed through a 0.2-μm-pore-size filter using a centrifuge to remove suspended precipitates and colloids. The Np concentration in the filtrate was measured with gamma spectroscopy. (Note that the filtrate contains an abundance of colloids smaller than 0.2 μm, and not all of the measured Np is necessarily dissolved.) The pH values of the test solutions were measured at room temperature with a combination electrode and pH meter that had been calibrated with NIST-traceable commercial buffer solutions (see **Note 1**).

Aliquots of some test solutions were taken for solids analyses. For TEM analysis, about 2 mL of test solution was passed through a TEM grid coated with a lacey formvar film that was fitted in a centrifuge tube. This film is porous and traps suspended solids as the solution is filtered through. Some of these have been characterized with analytical transmission electron microscopy (TEM). The membranes of some of the centrifuge filters used to filter the solutions for Np analysis were removed from the filter housing and embedded in epoxy for X-ray analysis at the Argonne National Laboratory Advanced Photon Source (APS). These were then examined by XAFS at the Argonne National Laboratory Advanced Photon Source (APS). Both X-ray absorption near edge (XANES) and extended X-ray absorption fine structure (EXAFS) spectroscopy measurements were performed.

Figure 3.1. Parr Instruments Model 4750 Reaction Vessel

3.2.2 Subtask (2) Heterogeneous Precipitation Study

An aliquot of the 1 x 10^{-4} M Np(V) stock solution was exposed to UO_2 in a scintillation vial at room temperature to determine if the presence of UO_2 facilitated the precipitation of NpO_2. A piece of UO_2 (taken from an archived source) was fixed in epoxy and one flat surface was exposed by polishing to a 600-grit final finish. (A nearly circular surface having a diameter of about 1 cm was exposed.) The embedded UO_2 was immersed in 9.53 g of the stock solution. The sealed vial was clamped to a circular rotator and rotated at a rate of 7.5 revolutions per minute to continually mix the solution. The test was conducted at ambient temperature (about 24ºC) for 4 days. The test solution was passed through a 0.2-µm-pore-size filter to remove suspended and colloidal material. The pH was measured with a combination electrode and the Np concentration was measured with gamma spectroscopy. The solid was analyzed at the APS.

An extensive test matrix to measure the effects of UO_2 and various steels on the precipitation of NpO_2 at room temperature was planned (see Table 3.2), but was not completed this year due to the stop-work order (see Note 1). Only test 200-UO_2-1 has been completed. The stop-work order impacted chemicals needed to prepare the Np(V) solution and measure the solution pH. The objective of the tests is to determine if UO_2 or the steels facilitate the precipitation of NpO_2 and estimate the steady-state dissolved concentration. The following standard steels were procured from NIST: SRM 101g (Type 304L stainless steel), SRM 1155 (Type 316 stainless steel), and SRM 20g (carbon steel). The steels were provided as chips

(shavings). The steel chips were embedded in epoxy as follows. A 1-cm hole was drilled into the axial center of a pre-cast epoxy plug about 1 inch in diameter and 5/8 inch tall. A piece of tape was place over the hole on one face of the plug and about 1 g of chips were placed in the hole. The hole was then filled with epoxy. After the epoxy cured, the tape was removed and that face was polished successively with 320, 400, and 600-grit carborundum paper with water lubrication to expose approximately 0.7 cm^2 area of polished steel. Three casts were made with each steel and three casts were made by filling the hole with epoxy but without steel for use in blank tests. It is planned to prepare stock solutions having Np(V) concentrations of 1×10^{-4} M, 1×10^{-5} M, and 1×10^{-6} M with the intent of using at least one solution that is supersaturated with respect to NpO_2 at room temperature. From the homogeneous precipitation tests, the solubility of NpO_2 is about 2×10^{-5} M at 200ºC and lower at higher temperatures. If UO_2 and/or steel catalyzes its formation at room temperature, NpO_2 is expected to precipitate from the 1×10^{-4} M solutions, but not from the 1×10^{-5} M solution. The solutions in each test are to be sampled after four durations to track the approach of the Np(V) dissolved concentration to steady state.

Table 3.2. Matrix of Tests to Study Heterogeneous Precipitation (Subtask 2)

Test ID	Nominal Np Concentration	Added Solid	Sampling Time, d
200-UO_2-1	1×10^{-4} M	1 surface of UO_2 pellet	4
(the tests listed below have not yet been conducted)			
Np1-UO2-1, -2, -3, -4	1×10^{-4} M	1 surface of UO_2 pellet	3, 7, 14, TBD[a]
Np2-UO2-1, -2, -3, -4	1×10^{-5} M	1 surface of UO_2 pellet	3, 7, 14, TBD
Np3-UO2-1, -2, -3, -4	1×10^{-6} M	1 surface of UO_2 pellet	3, 7, 14, TBD
Np1-S304-1, -2, -3, -4	1×10^{-4} M	Type 304L SS chips	3, 7, 14, TBD
Np2-S304-1, -2, -3, -4	1×10^{-5} M	Type 304L SS chips	3, 7, 14, TBD
Np1-S316-1, -2, -3, -4	1×10^{-4} M	Type 316 SS chips	3, 7, 14, TBD
Np2-S316-1, -2, -3, -4	1×10^{-5} M	Type 316 SS chips	3, 7, 14, TBD
Np1-SC-1, -2, -3, -4	1×10^{-4} M	Carbon steel chips	3, 7, 14, TBD
Np2-SC-1, -2, -3, -4	1×10^{-5} M	Carbon steel chips	3, 7, 14, TBD
NP1-blank-1, -2, -3, -4	1×10^{-4} M	None	3, 7, 14, TBD
NP2-blank-1, -2, -3, -4	1×10^{-5} M	None	3, 7, 14, TBD
NP3-blank-1, -2, -3, -4	1×10^{-6} M	None	3, 7, 14, TBD

[a]Test duration is to be determined based on the results of shorter-term samplings.

3.3 RESULTS

3.3.1 Stock Solution

The composition of the stock solution was measured with inductively coupled plasma-mass spectrometry (ICP-MS). The results are given in Table 3.3. The concentration of ^{237}Np was determined to be 2.42×10^{-5} µg/L with gamma spectroscopy (see Section 3.2.1 and Appendix A, Section A.1).

Table 3.3. Measured Composition of the Np(V) Stock Solution, µg/L

Element	Concentration	Element	Concentration	Element	Concentration
Ag[a]	5.99	Hf	<0.06	Rb	0.749
Al	<14.72	Ho	0.047	Re	<0.06
As	<0.58	Ir	<0.06	Rh	<0.02
Au	0.274	K	18400	Ru	<0.06
B	79.4	La	<0.04	Sb	0.114
Ba	<0.12	Li	35.3	Si	58.6
Ca	133	Lu	<0.02	Sm	<0.08
Cd	<0.22	Mg	<2.1	Sn	<0.06
Ce	0.33	Mn	<0.42	Sr	0.163
Co	<0.22	Mo	<0.66	Te	0.815
Cr	<0.44	Na	2450	Ti	<1.02
Cs	<0.1	Nb	<0.08	Tl	<0.04
Cu	2.11	Nd	<0.08	Tm	<0.01
Dy	<0.04	Ni	<1.58	U	0.504
Er	<0.06	^{237}Np[b]	24200	V	<0.12
Eu	<0.02	Pb	11.1	Y	<0.02
Fe	<36.2	Pd	1.53	Yb	<0.04
Ga	<0.06	Pr	<0.02	Zn	5.42
Gd	<0.24	Pt	<0.18	Zr	0.186
Ge	<0.52	^{239}Pu	0.085		

[a]Sum of ^{107}Ag (3.16 µg/L) and ^{109}Ag (2.83 µg/L).
[b]Measured with gamma spectroscopy.

3.3.2 Homogeneous Precipitation Serially Sampled Tests, Borosilicate Glass Liners

This series of tests, which was run in borosilicate glass liners, was stopped after about 56 days due to excessive corrosion of the borosilicate liners in the tests at 240 and 280ºC. In addition, it was seen upon opening the vessels that large amounts of water (e.g., 25-30 mL) had accumulated in the vessels outside of the liners. We believe that this is mostly condensed vapor that was present in the air space at the test temperature and condensed onto the steel vessel when it was cooled; some water probably also evaporated from the test solution and condensed onto the steel vessel as it cooled, since the solution temperature remained higher than the vessel temperature for probably several hours. In the 8/1/2005 sampling of the 240 and 280ºC test solutions, the solutions inside the liners appeared cloudy (probably the result of colloidal dispersions), whereas solution outside the liner was clear. The colloids are generated during glass dissolution (see below). This is consistent with the water outside the liner being condensed vapor that collected when the vessel was cooled and the water inside the liner being the test solution. The test solution was transferred from the liner into a collection bottle. The liner was then carefully removed from the vessel and the water remaining in the steel vessel (and the drop clinging to the liner) was removed using a pipette and added to the test solution in the collection bottle. Very small amounts of water left on the outer surfaces of the vessel and the liner could not be recovered.

The effects of condensation are considered in the following. Saturation of the air in the vessel with water vapor during the test will reduce the solution volume slightly due to evaporation, more so at higher test temperatures, and the amount of water that evaporates can be estimated. The interior volume of the steel vessels is 125 mL and the volume occupied by the borosilicate liner is about 20 mL. Tests run with the borosilicate glass liners contained about 60 mL of solution, so there is about 45 mL of air space in the vessel. Using the specific volumes of steam at the test temperatures from the steam tables, it requires about 0.56, 1.7, 3.7, and 7.2 g of water to saturate the 45 mL of air space in tests at 150, 200, 240, and 280ºC, respectively (see Appendix A, Section A.2). The decreases in the solution volumes due to evaporation during the tests at 150, 200, 240, and 280ºC are about 1%, 3%, 6%, and 14%, respectively, and the test solutions are diluted by these same factors when the water vapor condenses at the end of the test. The amounts of water found outside the liner at the end of the tests greatly exceed the amounts calculated to have been vaporized during the tests, which implies that water has evaporated from the test solutions and condensed on the steel vessels outside of the liners when the vessels were cooled. The large thermal gradient developed between the steel and the solutions vessels as the vessels cooled likely caused the transport of water to outside the liner. Therefore, the water that had condensed outside the liner was added back to the test solution that remained within the liner to better represent the solution composition attained during the test. Although this does result in a slight dilution relative to the composition at the test temperature (due to the addition of the small amount of water that had vaporized during the test), the error is small. That is, the concentrations measured with the condensed water added back to the solution will be a few percent lower than the concentrations attained at the test temperature when some of the water had vaporized. Although the tests with borosilicate glass liners were eventually halted due to corrosion of the glass (see below), they could not have been continued if the water found outside the liner had been discarded at each sampling. Also, if some of the water outside the liner is actually spilled test solution, it needs to be taken into account (even if the dissolved Np was reduced by the steel) to determine the dissolved concentration.

The test execution data for sampling tests with borosilicate glass liners are summarized in Table 3.4. The tests were stopped due to extensive corrosion of the borosilicate liners. Figure 3.2 shows a new borosilicate glass liner and the liner recovered from the 280ºC test on September 15, 2005, after 55 days of reaction. (The new liner has an outer diameter of 1.3 inches and is about 4.3 inches tall.) The solution results are given in Table 3.5. Notice that more than 90% of the Np has been removed from solution at all temperatures and that the solution pH values have increased from that of the stock solution. The pH increase is probably due to dissolution of the borosilicate glass liner. Although the composition of the glass is not known and the solutions were not analyzed for glass constituents, the release of alkali metals and boron commonly generate alkaline solutions. Based on Equation 3.1, the high pH values should promote the formation of NpO_2. The dissolved Np concentrations are plotted in Figure 3.3. Although there are only 2 or 3 data points at each temperature, the concentrations in tests at 200, 240, and 280ºC imply that these systems are near steady state. Note that although these tests were designed to provide a homogeneous system, corrosion of the liner lead to a heterogenous system.

Table 3.4. Test Execution Data for Homogeneous Precipitation Tests, Borosilicate Glass Liners

Sampling Date	Interval Duration, d	Filtrate Sample Number	Bottle Tare, g	Bottle with Np Solution, g	Filtrate Solution Mass, g	pH
Test 150-1: 150ºC, Vessel No. 4 Test started 6/7/2005; Starting mass stock solution= 60.10 g						
6/13/2005	6	150-1-1	—	—	0.9288	7.16
7/6/2005	29	150-1-2	—	—	1.9838	7.40
8/2/2005	56	150-1-3[a, b]	11.1613	13.4104	2.2491	7.60
Test 200-1: 200ºC, Vessel No. 3 Test started 6/7/2005; Starting mass stock solution= 80.15 g						
6/13/2005	6	200-1-1	—	—	0.8052	7.50
7/6/2005	29	200-1-2	—	—	2.0120	7.99
8/2/2005	56	200-1-3[a, b]	11.1689	13.4567	2.2878	8.13
Test 240-1: 240ºC, Vessel No. 240 Test started 7/22/2005; Starting mass stock solution= 80.03 g						
8/1/2005	10	240-1-1	11.1902	12.3288	1.1386	8.13
8/16/2005	25	240-1-2	11.1802	13.5621	2.3819	8.33
9/15/2005	55	Not analyzed	—	—	—	—
Test 280-1: 280ºC, Vessel No. 280 Test started 7/22/2005; Starting mass stock solution= 80.02 g						
8/1/2005	10	280-1-1	11.1797	12.3053	1.1256	8.44
8/16/2005	25	280-1-2	11.1913	13.6055	2.4142	8.24
9/15/2005	55	Not analyzed	—	—	—	—

[a]Sample of test solution prepared for TEM examination.
[b]Sample of filter prepared for examination at APS.

Figure 3.2. Borosilicate Liners Before Use (left) and After 55 Days of Reaction at 280ºC (right)

Table 3.5. Solution Results for Homogeneous Precipitation Tests, Borosilicate Glass Liners

Filtrate Sample Number	Interval Duration, d	$[H^+]$, M	^{237}Np in Filtrate Solution		Decrease in ^{237}Np Conc. due to Precipitation, moles/L	Decrease in Amount of Dissolved Np, %
			^{237}Np Activity, µCi	^{237}Np, moles/L		
Test 150-1 at 150ºC						
150-1-1	6	6.93E-08	1.37E-03	8.85E-06	9.35E-05	91.35%
150-1-2	29	3.96E-08	2.57E-03	7.76E-06	9.45E-05	92.42%
150-1-3	56	2.51E-08	2.49E-03	6.62E-06	9.57E-05	93.53%
Test 200-1 at 200ºC						
200-1-1	6	3.16E-08	2.00E-04	1.49E-06	1.01E-04	98.55%
200-1-2	29	1.02E-08	5.23E-04	1.55E-06	1.01E-04	98.48%
200-1-3	56	7.5E-09	4.85E-04	1.27E-06	1.01E-04	98.76%
Test 240-1 at 240ºC						
240-1-1	10	7.38E-09	5.32E-04	2.79E-06	9.95E-05	97.27%
240-1-2	25	4.65E-09	1.06E-03	2.67E-06	9.96E-05	97.39%
Test 280-1 at 280ºC						
280-1-1	10	3.65E-09	<1.27E-05	<6.72E-08	>1.03E-04	>99.93%
280-1-2	25	5.73E-09	3.68E-05	9.12E-08	1.02E-04	99.91%

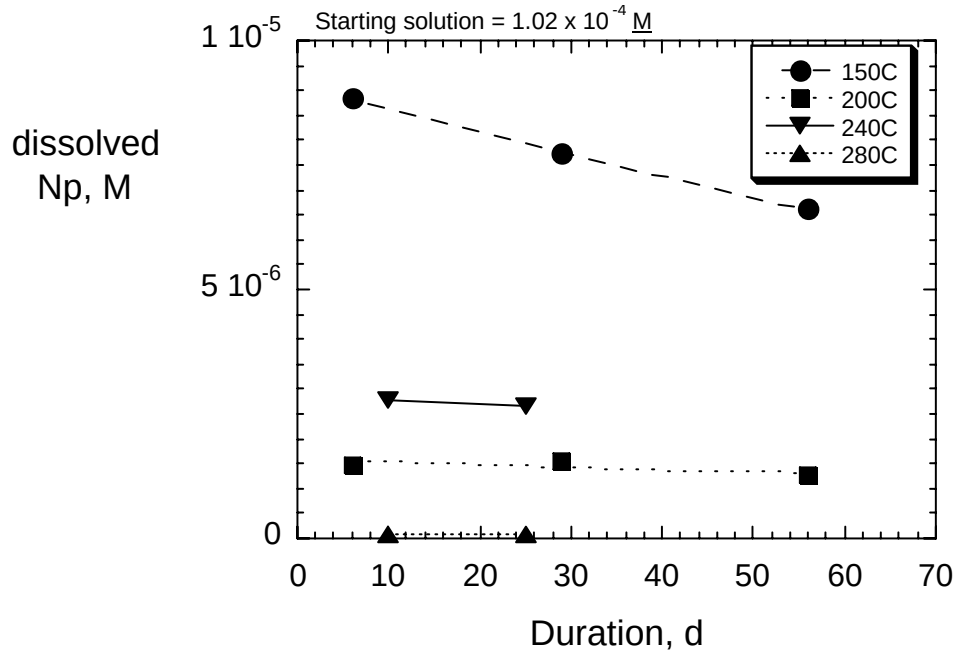

Figure 3.3. Results of Homogeneous Precipitation Tests in Borosilicate Glass Liners

3.3.2.1 Transmission Electron Microscopy (TEM)

Suspended solids from solution samples 150-1-3 and 200-1-3 were prepared for TEM analysis by centrifuging approximately 2 mL of the test solution through a TEM grid with a "lacey" formvar coating that was mounted directly onto a 0.1-μm-pore-size (nominal) centrifuge filter. A preliminary examination was conducted to ascertain the quality of the sample preparation method. (The calibration cycle for the TEM magnification had lapsed when these analyses were performed, and these results are qualitative in nature. They are not used as a quantitative measurement.) The examination was limited to a small portion of the grid and was done quickly to minimize the time that the sample was exposed to the electron beam (to minimize the extent of beam-induced reduction). There was no evidence that the sample was beam-sensitive.

Figures 3.4a and 3.4b show a region at moderate and high magnifications of the filtered solids from sample 200-1-3, respectively. The formvar substrate used to filter the suspended solids is seen in the bottom of both photomicrographs. The most abundant particles, by far, are spheroids of amorphous silica (Figure 3.4a) that are approximately 50 nm in diameter. These probably formed as a result of corrosion of the borosilicate glass liner. The Np-bearing particles were visually located based on their irregularly-faceted morphology and darker appearance (the Np-bearing particles have a higher density than the silica that attenuates the transmission of electrons). The Np-bearing particles are associated with platy aluminosilicate phases, as shown in Figure 3.4b, which were probably also generated during liner corrosion. The presence of Np in these particles was confirmed using energy dispersive x-ray spectroscopy (EDS). Only the silica spheres were detected upon examination of the solids from sample 150-1-3; no Np-bearing solids were seen. The TEM analyst noted there were "perhaps trace [amounts of] Np from EDS" analysis of the spheres.

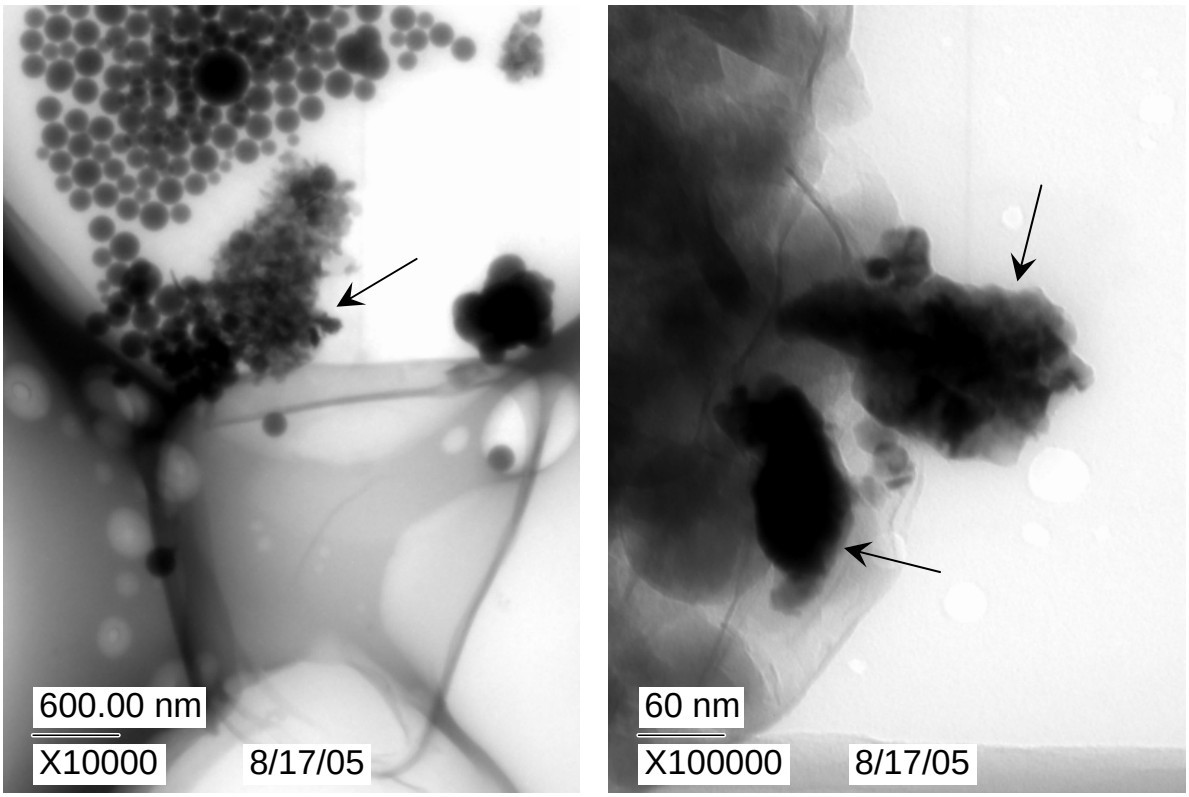

(a) (b)

Figure 3.4. TEM Photomicrographs of Solids Recovered from Sample 200-1-3. (a) Np-bearing colloid (marked by arrow) and spherical silica particles and (b) Np-bearing particles (marked by arrows) on an aluminosilicate substrate.

Electron diffraction analysis of the Np-bearing particles in the 200-1-3 sample was performed using a selected area aperture that encompassed the particles in Figure 3.4. Images of the selected area electron diffraction (SAED) patterns were taken using 60 cm and 120 cm camera lengths (Figures 3.5a and 3.5b). The diffraction patterns appear as spots and streaks that form concentric rings in reciprocal space, and the radii of the rings are related to the reciprocal of the crystalline *d*-spacings. Increasing the camera length increases the resolution of the pattern. If the diameter of a ring (*2Q*) is measured as the distance between diametrically opposite spots or streaks, the *d*-spacing is calculated as

$$d = \frac{2\pi}{Q} \quad . \tag{3.4}$$

The distances between symmetrically opposite diffraction spots on images of the SAED patterns were measured with a ruler to determine a set of *2Q* values. (For instances where only one spot was seen, the distance to the center of the pattern was measured to determine *Q*.) The measured distance was converted to reciprocal Angstroms using the scale bar for each pattern. The *d*-spacing was calculated with Equation 3.4. The results for sample 200-1-3 from Figure 3.5b are summarized in Table 3.6 (the complete results and comparisons are given in Appendix B), along with literature values for *d*-spacings in crystalline NpO_2, Np_2O_5, Np_3O_8, and

$NpO_3 \cdot H_2O$. The uncertainty in the *d*-spacings due to measurement of the diffraction pattern decreases from about ±0.02 Å at a *d*-spacing of 3.20 Å to about ±0.003 Å at a *d*-spacing of 1.05 Å. This is based on the uncertainty in measuring the distance between spots. An additional systematic error in the calculated *d*-spacings on the order of 3% can occur if the crystal is not in the eucentric position in the microscope. This was minimized by locating the center of the diffraction pattern using symmetrically opposite spots. Similar errors can arise due to crystal size effects, variation in the stoichiometry, or the presence of impurities.

The measured *d*-spacings in the SAED analysis of the solid formed in sampling 200-1-3 are consistent with the presence of NpO_2 and perhaps another phase, but these results do not clearly discriminate between the possible Np-bearing phases having different Np oxidation states. For example, the measured *d*-spacings match those of $NpO_3 \cdot H_2O$ almost as well. The formation of this phase in these tests is highly unlikely, but this shows SAED analysis alone is not sufficient to distinguish between NpO_2 and other phases.

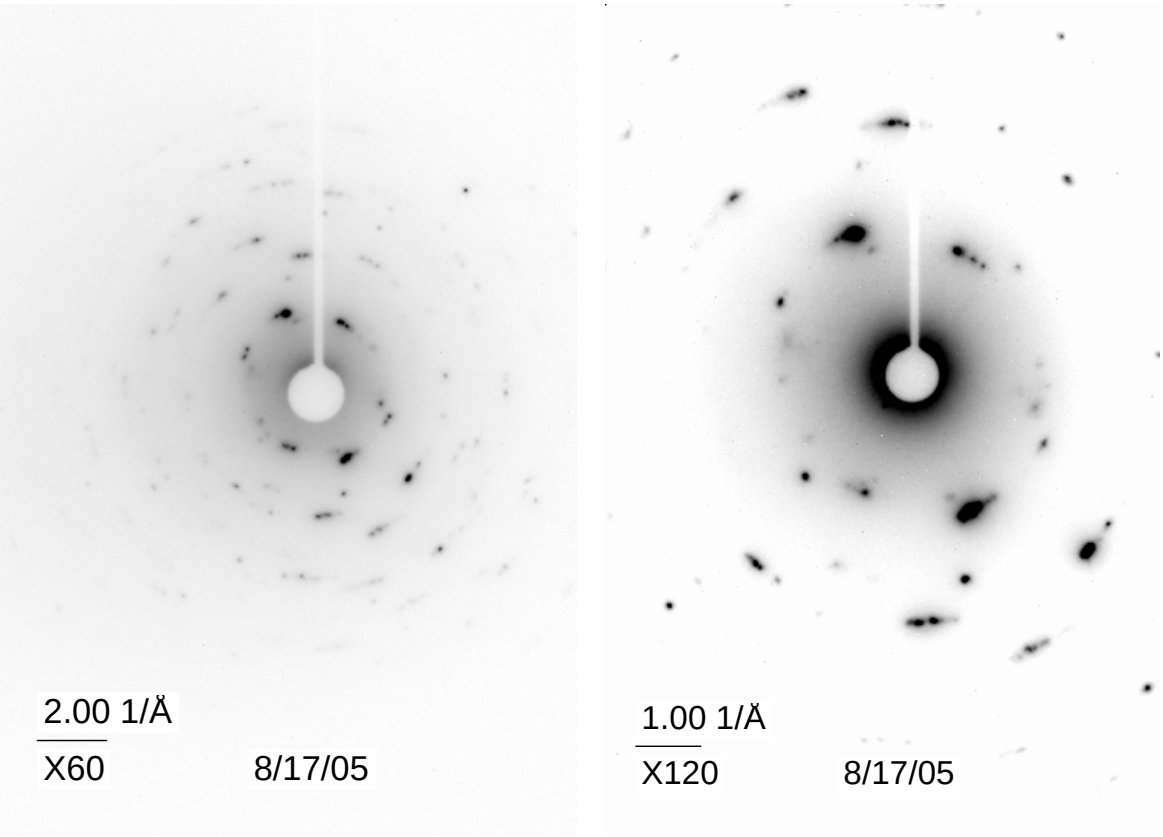

(a) (b)

Figure 3.5. Selected Area Electron Diffraction Analysis of Np-Bearing Solids in Sample 200-1-3 with (a) 60-cm camera length and (b) 120-cm camera length

Table 3.6. Electron Diffraction Results for Sample 200-1-3 and Reference Materials, d-spacings in Å

Sample 200-1-3	Reference Materials			
	NpO_2	Np_2O_5	Np_3O_8	$NpO_3 \bullet H_2O$
3.20	3.14	3.30	3.27	3.14
2.78	2.72	2.68	2.66	2.80
1.94	1.92	1.93	1.93	1.95
—	—	1.73	1.73	—
1.67	1.64	1.65	1.65	1.69
1.60	1.57	1.61	1.60	1.60
1.39	1.36	1.46	1.46	1.47
—	—	1.29	1.29	1.30
1.14	—	—	—	—
1.07	1.11	—	—	—

3.3.2.2 X-Ray Absorption Studies (EXAFS & XANES) (for tests in borosilicate glass liners)

Extended x-ray absorption fine structure (EXAFS) spectroscopy and x-ray absorption near edge structure (XANES) spectroscopy measurements were made at the Materials Research-Collaborative Access Team (MR-CAT), 10ID beam line at the Argonne National Laboratory Advanced Photon Source (APS). The beam line consists of a cryogenically cooled Si(111) double crystal monochromator for energy selection with a rhodium-coated mirror for higher-order harmonic rejection. The insertion device was scanned synchronously with the Bragg angle motion of the monochrometer using the 3rd harmonic. The energy scale was calibrated with a standard reference material containing Np (obtained from NIST) that was scanned in transmission mode downstream of the sample. By careful analysis of the reference spectra, the relative energy scales of the individual scans were aligned to within 0.15 eV, which is approximately one encoder step. A multi-element germanium detector (Canberra) was used to measure the neptunium L-alpha fluorescence from the samples. Live time was typically kept above 75% to minimize the effect of dead time and other count rate corrections. Beam damage effects were deemed to be insignificant based on the results of several subsequent rapid scans of each sample. Data from individual detector elements were inspected to exclude channels with excessive noise or other obvious systemic errors (e.g., level shifts) from the analysis. Signals in each of the remaining channels were summed over several scans and were averaged to create the spectrum for each sample.

One of the difficulties of using the near edge structure of the Np L_3 edge to determine the oxidation state is that the edge positions for Np^{4+} and Np^{5+} are at nearly the same energy. Instead, other spectral features can be used to distinguish the oxidation state. Figure 3.6 shows the spectra of an NpF_4 reference material and the Np(V) stock solution, which provide representative spectra for Np(IV) and Np(V), respectively, along with the spectra for samples 150-1-3 and 200-1-3. By comparison with the reference spectra for the reference and stock solution, both Np(IV) and Np(V) are present in both the 150-1-3 and 200-1-3 samples. The spectrum of sample 200-1-3 is more similar to that of NpF_4 than to that of the stock solution, and

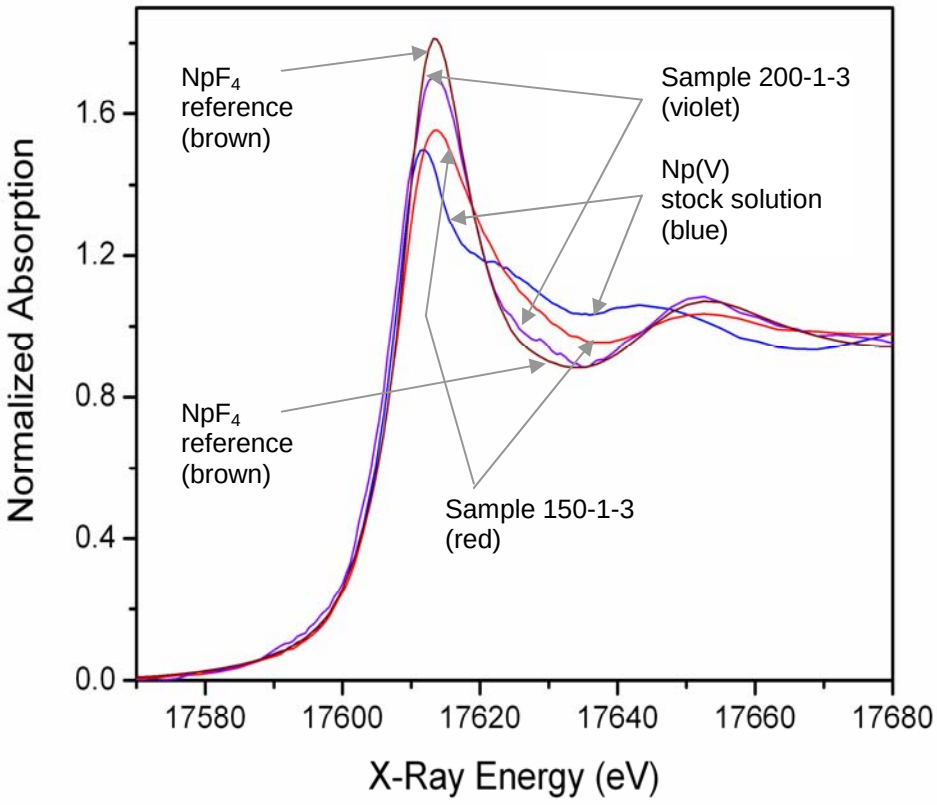

Figure 3.6. XANES NpL_3 Edge Spectra of Np(V) Stock Solution, Samples 200-1-3 and 150-1-3, and NpF_4 Reference Material

probably contains more Np(IV) than Np(V). The shoulder above the white line in the spectrum of the Np(V) stock solution (i.e., at about 17630 eV) is indicative of the neptunyl species, NpO_2^+, sample 200-1-3. Although a shoulder peak is not obvious in the spectrum of sample 150-1-3, the major peak is broadened relative to the stock solution. The hump that occurs in the spectrum of the Np(V) stock solution near 17644 eV is shifted to higher energies in the other spectra (about 17653 eV). Comparisons of the spectra indicate that both the 200-1-3 and 150-1-3 samples have predominantly Np(IV) character, but also some Np(V) character. The solids may contain a mixture of two phases (e.g., NpO_2 and Np_2O_5). No Np-bearing phases were detected in the TEM examination of the wicked test solution. It is likely that the spectrum of the filter from sample 150-1-3 shown in Figure 3.6 is that of Np sorbed onto silica colloids.

The Fourier transform magnitude (k^2 weighted) plots derived from the EXAFS results for the Np(V) stock solution and samples 150-1-3 and 200-1-3 are shown in Figure 3.7. The data are shown by the red squares and the fits are shown by the blue lines. Lightly colored vertical lines are drawn through the figures to facilitate comparison of peak positions in the three spectra. The fit to EXAFS results for the Np(V) stock solution in Figure 3.7a is based on two short Np-O bonds, one at 1.80 Å and the other at 2.50 Å, which is consistent with the presence of NpO_2^+. The experimental peak at 3 Å is not reproduced by this model. (Note that the bond lengths are phase-shifted from the radial coordinates in the Fourier transform plot, and are not directly

proportional. The radial coordinates of peaks in the plots of the same elements, in this case Np and O, are directly comparable.)

The Fourier transform of the spectrum for sample 150-1-3 is shown in Figure 3.7b. A second-shell peak appears at 3.0 Å (located by arrow) that is similar to the peak in the spectrum of the Np(V) stock solution (Figure 3.7a). However, the most intense peak from the spectrum of the 150-1-3 sample at a radial coordinate of about 1.7 Å does not match the Np(V) spectrum. The *k*-dependence indicates Np has next-nearest neighbors with a lower atomic number (i.e., not a Np-Np scattering path), which indicates that NpO_2 is not present in this sample.

Figure 3.7c shows the results for the 200-1-3 sample (squares) and model fit using an Np-O bond length of 2.32 Å and an Np-Np scattering path of 3.82 Å. These bond lengths are consistent with the inter-atomic distances of NpO_2 in the fm3m structure. The measured coordination number for Np-Np in the 200-1-3 spectrum is 0.45. This low value indicates that the sample is comprised of nanometer-sized particles, which is consistent with the TEM results. The most intense peak at a radial coordinate of about 1.7 Å matches that in the 150-1-3 sample, but no peak is seen at 3 Å. The remaining mismatches between this simple model and the data are an indication that the structure of the solid is more complex than single phase NpO_2. This is probably due to the presence of a second phase that, based on the XANES results, contains Np(V).

3.3.3 Homogeneous Precipitation Serially Sampled Tests, Quarts Liners

Small amounts of water were found outside of the quartz liners. These tests were run in quartz liners, with about 80 mL of solution and about 25 mL of air space in the test vessels. Only about 0.3 g of water is needed to saturate the of air space at 150ºC, and about 1, 2, and 4 g are needed at 200, 240, and 280ºC, respectively. The small decrease in the solution volume due to evaporation during the test at 150, 200, 240, and 280ºC results in dilution factors of about 0.4, 1, 3, and 5% when the vapor recondenses after the vessel is cooled to room temperature. Although the same temperature gradient existed between the solution and the test vessel as in the tests with the borosilicate glass liners, the much smaller volume available between the quartz liner and the vessel allowed less water to accumulate outside the liner (i.e., most of the condensate collected in the liner as the vessel cooled). The quartz liners were not visibly corroded during the tests.

The test data for the serially sampled homogeneous precipitation tests run in quartz liners are summarized in Table 3.7. The mass of Np(V) stock solution initially added to the liner was weighed, but the total mass of test solution was not tracked during the tests. In addition to the aliquots taken for analysis of the pH and Np concentration, small aliquots were taken from solution sample numbers 150-2-1, 200-2-1, 200-2-2, 240-2-1, 240-2-2, 280-2-1, and 280-2-2 to prepare samples for TEM examination; the exact amounts of solution that were removed were not measured, but were less than 2 mL. The mass of solution present in the liner during each test interval was not used in the calculations; only the concentrations measured in the filtrate solutions were used to track the change in the Np concentrations and calculate the amounts of Np that had precipitated. Therefore, the decrease in the total solution volume due to samplings does not impact the results, provided that the solution is well-mixed when the aliquots are taken. This

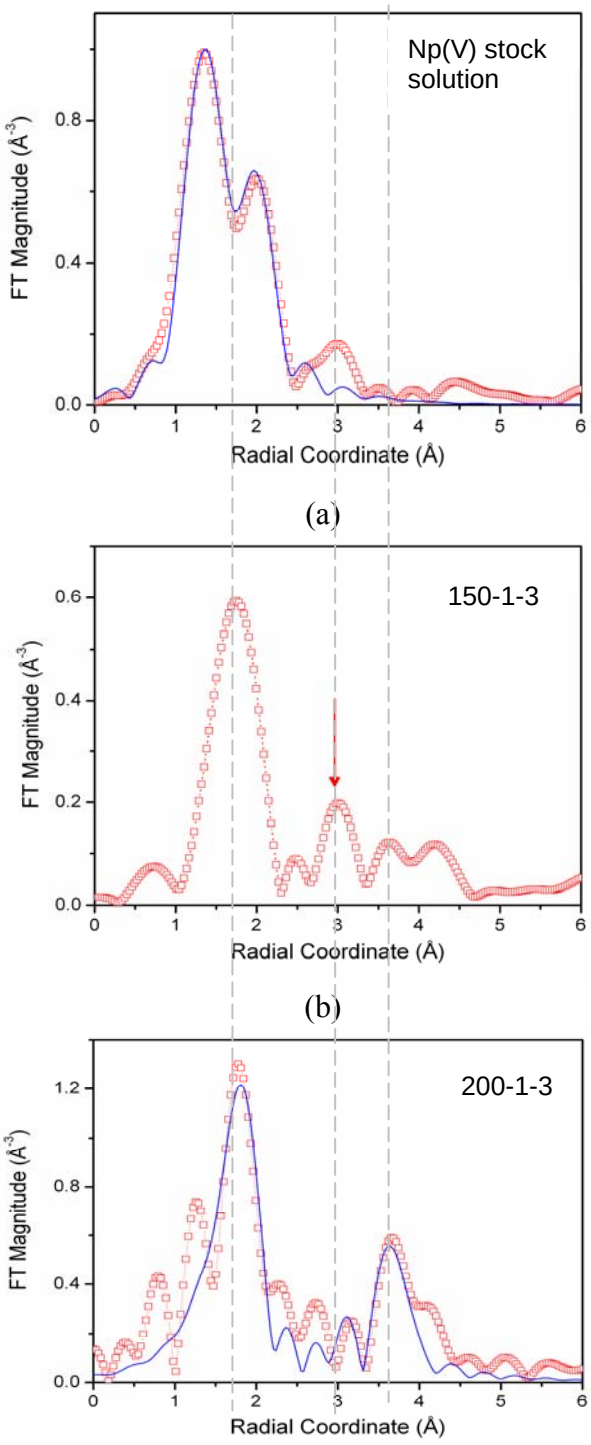

Figure 3.7. Fourier Transform Magnitude (k^2 weighted) EXAFS Results for (a) Np(V) stock solution, (b) sample 150-1-3, and (c) sample 200-1-3

Table 3.7. Test Execution Data for Homogeneous Precipitation Tests, Quartz Liners

Sampling date	Interval duration, d	Filtrate Sample Number	Bottle tare, g	Bottle with Np solution, g	Filtrate solution mass, g	pH
Test at 150ºC, Vessel No. 4 Test started 9/21/2005; Starting mass stock solution= 80.10 g						
9/23/2005	2	150-2-1[a]	11.1729	13.0855	1.9126	5.94
10/3/2005	12	150-2-2	11.1232	13.6331	2.5099	5.54
10/12/2005	21	150-2-3[b]	11.1798	13.6224	2.4426	5.52
11/28/2005	68	150-2-4	11.1914	13.2074	2.0160	5.42
7/7/2006	289	150-2-5	11.1855	12.9729	1.7874	5.62
Test at 200ºC, Vessel No. 3 Test started 9/21/2005; Starting mass stock solution= 80.15 g						
9/23/2005	2	200-3-1[a]	11.1344	13.1062	1.9718	4.79
10/3/2005	12	200-3-2[a]	11.1404	13.1457	2.0053	4.47
10/12/2005	21	200-3-3[b]	11.1780	12.4155	1.2375	4.58
11/28/2005	68	200-3-4	11.1661	13.2513	2.0852	4.30
7/7/2006	289	200-3-5	11.2286	12.9404	1.7118	4.42
Test at 240ºC, Vessel No. 240 Test started 9/21/2005; Starting mass stock solution= 80.03 g						
9/23/2005	2	240-2-1[a]	11.1883	13.0801	1.8918	4.59
10/3/2005	12	240-2-2[a]	11.1640	13.4528	2.2888	4.75
10/12/2005	21	240-2-3[b]	11.1909	12.4528	1.2619	4.46
11/28/2005	68	240-2-4	11.2032	13.2120	2.0088	7.31
Test at 280ºC, Vessel No. 280 Test started 9/21/2005; Starting mass stock solution= 80.02 g						
9/23/2005	2	280-2-1[a]	11.2092	12.9565	1.7473	4.78
10/3/2005	12	280-2-2[a]	11.1531	12.3351	1.1820	5.90
10/12/2005	21	280-2-3[b]	11.1764	11.7347	0.5583	4.95
11/28/2005	68	280-2-4	11.1244	12.9718	1.8474	4.67

[a] Sample of test solution prepared for TEM examination.
[b] Sample of filter prepared for examination at APS.

is why the water that condensed outside the liner was recovered and mixed with the test solution prior to analysis. The results of gamma spectrometry analyses of the samples taken from the serially sampled homogeneous precipitation tests are summarized in Table 3.8 and the results for samplings through 68 days are plotted in Figures 3.8a-8d. (The samplings of tests at 150 and 200ºC taken after 289 days are omitted from these plots to better show and compare the short-term results.) In Table 3.8, the decrease in ^{237}Np concentration due to precipitation is calculated by subtracting the concentration measured in the test from the concentration in the stock solution. The results for tests at each temperature are discussed below.

Table 3.8. Solution Results for Homogeneous Precipitation Tests, Quartz Liners

Filtrate Sample Number	Interval Duration, d	$[H^+]$, M	^{237}Np in Filtrate Solution		Decrease in ^{237}Np Conc. due to Precipitation, moles/L	Decrease in Amount of Dissolved Np, %
			^{237}Np Activity, µCi	^{237}Np, moles/L		
Test 150-2 at 150ºC						
150-2-1	2	1.16E-06	3.051E-02	9.543E-05	6.872E-06	6.73%
150-2-2	12	2.88E-06	4.014E-02	9.566E-05	6.644E-06	6.50%
150-2-3	21	3.01E-06	3.870E-02	9.478E-05	7.520E-06	7.36%
150-2-4	68	3.84E-06	3.177E-02	9.426E-05	8.042E-06	7.87%
150-2-5	289	2.40E-06	3.570E-02	1.195E-04	-1.717E-05	-16.78%
Test 200-3 at 200ºC						
200-3-1	2	1.63E-05	1.484E-02	4.503E-05	5.727E-05	55.98%
200-3-2	12	3.38E-05	6.320E-03	1.885E-05	8.345E-05	81.57%
200-3-3	21	2.66E-05	3.526E-03	1.704E-05	8.526E-05	83.34%
200-3-4	68	5.02E-05	6.242E-03	1.791E-05	8.439E-05	82.50%
200-3-5	289	3.82E-05	5.577E-03	1.949E-05	8.281E-05	80.95%
Test 240-2 at 240ºC						
240-2-1	2	2.56E-05	2.127E-03	6.725E-06	9.558E-05	93.43%
240-2-2	12	1.80E-05	2.945E-03	7.698E-06	9.460E-05	92.48%
240-2-3	21	3.44E-05	1.499E-03	7.106E-06	9.519E-05	93.05%
240-2-4	68	4.90E-08	3.389E-03	1.009E-05	9.221E-05	90.14%
Test 280-2 at 280ºC						
280-2-1	2	1.65E-05	3.303E-04	1.131E-06	1.012E-04	98.89%
280-2-2	12	1.26E-06	4.488E-04	2.272E-06	1.000E-04	97.78%
280-2-3	21	1.12E-05	2.838E-04	3.040E-06	9.926E-05	97.03%
280-2-4	68	2.13E-05	2.230E-03	7.220E-06	9.508E-05	92.94%

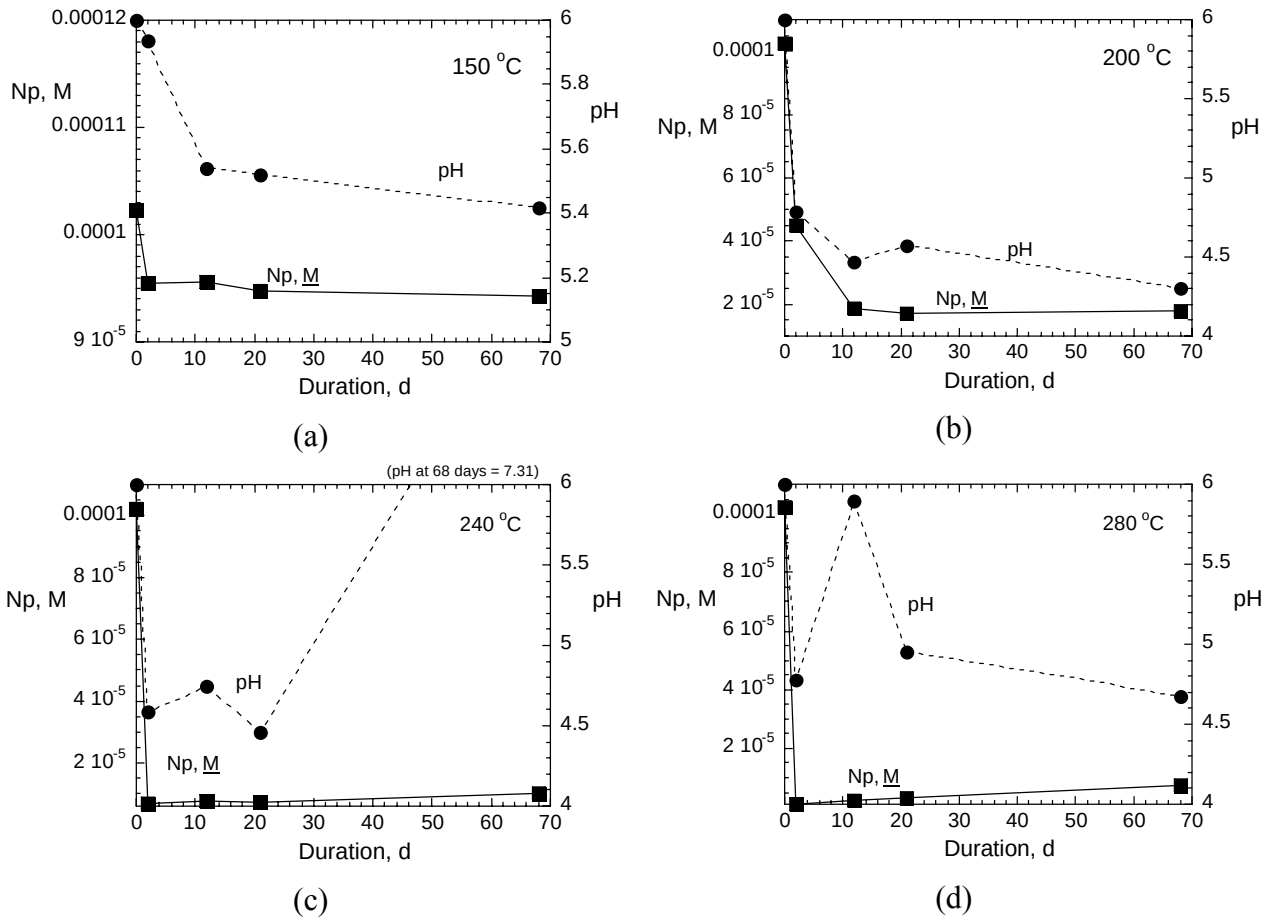

Figure 3.8. Neptunium in the Test Solutions of Serially Sampled Homogeneous Precipitation Tests through 68 Days at (a) 150ºC, (b) 200ºC, (c) 240ºC, and (d) 280ºC

150 ºC – The results of samples taken from the test at 150ºC show Np concentrations that are below the concentration in the stock solution through 68 days, but the Np concentration measured in the sampling taken after 289 days (1.195×10^{-4} M) was about 15% higher than that in the stock solution. This degree of concentration would require the loss of 11.51 g of water (without losing any Np), which is an unreasonably large amount of water. The difference in concentrations is attributed to the combined uncertainty in testing and analysis. Although the samplings after 2, 12, 21, and 68 days suggest that a small amount of Np has precipitated from solution, the high concentration measured after 289 days indicates that these solids either redissolved or were never formed. In fact, the concentration in the 289-day sampling is about 17% higher than the concentration in the stock solution and is suspected to be in error. Although some evaporative loss of solution probably occurred during sampling, a loss of 17% would correspond to about 11 mL of test solution between samplings 150-3-4 and 150-3-5. An error of about 0.5 mL in the sample volume would be required to account for the discrepancy, and this is not plausible. The sample mass was re-checked and found to be correct and the solution was re-analyzed for Np content. The re-measured Np concentration was 1.25×10^{-4} M. (The counting uncertainties in the gamma spectroscopy analyses at successive samplings were 0.23%, 0.11%, 0.24%, 0.48%, and 0.09% for the original analyses, and 0.10% for the re-analysis of 150-2-5.)

200ºC – The results of samples taken from the test at 200ºC show Np concentrations to decrease significantly during the first and second test intervals of 2 and 12 days, and then to remain nearly constant in samplings taken after 21, 68, and 289 days (289-day result not shown in Figure 3.8b). The steady-state concentration is taken to be the average of the concentrations in the 12, 21, and 68 day samplings, which is 1.79×10^{-5} M. (The counting uncertainties in the gamma spectroscopy analyses of the test solutions at successive samplings were 0.32%, 0.34%, 0.45%, 0.79%, and 0.28%.)

240ºC – The results of samples taken from the test at 240ºC show Np concentrations to decrease precipitously during the initial test interval and to remain nearly constant thereafter. The steady-state concentration is taken as the average of the values in the 4 samplings, which is 7.91×10^{-6} M. The concentration increases slightly in the 68-day sampling, but the masses were not measured and this cannot be attributed to water vapor loss. (The counting uncertainties in the gamma spectroscopy analyses of the test solutions at successive samplings were 0.70%, 0.53%, 0.95%, and 1.00%.)

280ºC – The results of samples taken from the test at 280ºC also show Np concentrations to become very low immediately and to remain low. The steady-state concentration is taken as the average of the values in the 4 samplings, which is 3.42×10^{-6} M. The concentration increases slightly in the 68-day sampling, but the masses were not measured and this cannot be attributed to water vapor loss. (The counting uncertainties in the gamma spectroscopy analyses of the test solutions at successive samplings were 3.8%, 1.7%, 2.7%, and 0.83%.)

3.3.3.1 TEM Analysis of Suspended Solids

Solids recovered from the test solutions from samplings 150-2-1, 200-3-2, 240-2-1, and 280-2-1 by passage through lacey formvar-coated copper TEM grids were examined with TEM. Many Np-bearing solids were seen in the samples from samplings 200-3-2, 240-2-1, and 280-2-1, but only Si-based spheroids were seen in sample 150-2-1. Crystalline Np-bearing particles were seen in the other samples with a hexagonal growth habit (seen most clearly in the 240-2-1 sample) and sized 50–1000 nm across. Several crystals from each sample were analyzed with SAED, and the results are tabulated in Appendix B as *d*-spacings determined from the measured spot separations. These are arranged to facilitate comparisons of spectra for each sampling with each other and with *d*-spacings measured in x-ray diffraction studies of Np-bearing oxides from the literature. (In Table B-1, the numeric spectrum identifiers indicate different particles and the suffixes "a, b, c" indicate different locations on the same particle.) Due to the limited orientations that were sampled in the SAED analyses, not all of the *d*-spacings will be detected for the crystallites that are analyzed in any given spectrum. Therefore, the *d*-spacings obtained from the analyses of several particles (or different regions of a particle) in each sampling should be consolidated for comparison with the literature values of *d*-spacings measured with x-ray diffraction. The relative intensities of the diffraction peaks from x-ray diffraction analyses are not relevant for comparisons with SAED spectra due to the limited number of orientations that are sampled during the SAED analyses.

The sets of particles within each sampling have several *d*-spacings that are very similar, and several *d*-spacings are common to all samples; however, the sample spectra cannot be matched uniquely to any of the Np-bearing reference materials, including NpO_2 and Np_2O_5. The

reference materials have many similar *d*-spacings, and the differences between the reference materials are similar to the differences in the samples.

3.3.3.2 X-Ray Absorption Studies (EXAFS & XANES) (tests with quartz liners)

Solids recovered from test solution samples 200-3-3, 240-2-3, and 280-2-3 were analyzed with EXAFS spectroscopy and XANES spectroscopy at the APS. Figure 3.9 shows the spectra obtained for the precipitates, the stock solution, and an NpF_4 reference material. The stock solution shows a major peak at about 17612 eV, a shoulder peak at about 17623 eV, and a weak peak at about 17644 eV. The spectra of the precipitated phases are essentially identical and overlap each other, and all match almost exactly the spectrum of the NpF_4 reference material. The spectra of the NpF_4 reference material and all precipitates have a major peak at about 17614 eV and a minor peak at about 17653 eV, and possibly a shoulder at about 17628 eV. The similarity of the spectra of the precipitates to that of the NpF_4 reference material and dissimilarity with the stock solution indicates that the precipitates contain Np(IV) with no detectable Np(V). Figure 3.10 shows the Fourier transform spectrum determined from the XANES spectrum for the solids in sample 200-3-3 and the model with atomic spacings 2.35 Å and 2.85 Å (for the nearest and next-nearest neighbors). The modeled fit is in good agreement with NpO_2, although there is some minor discrepancy at radial distances between 4 and 5 Å. Based on their identical spectra, solids formed at 240 and 280ºC are also identified as NpO_2.

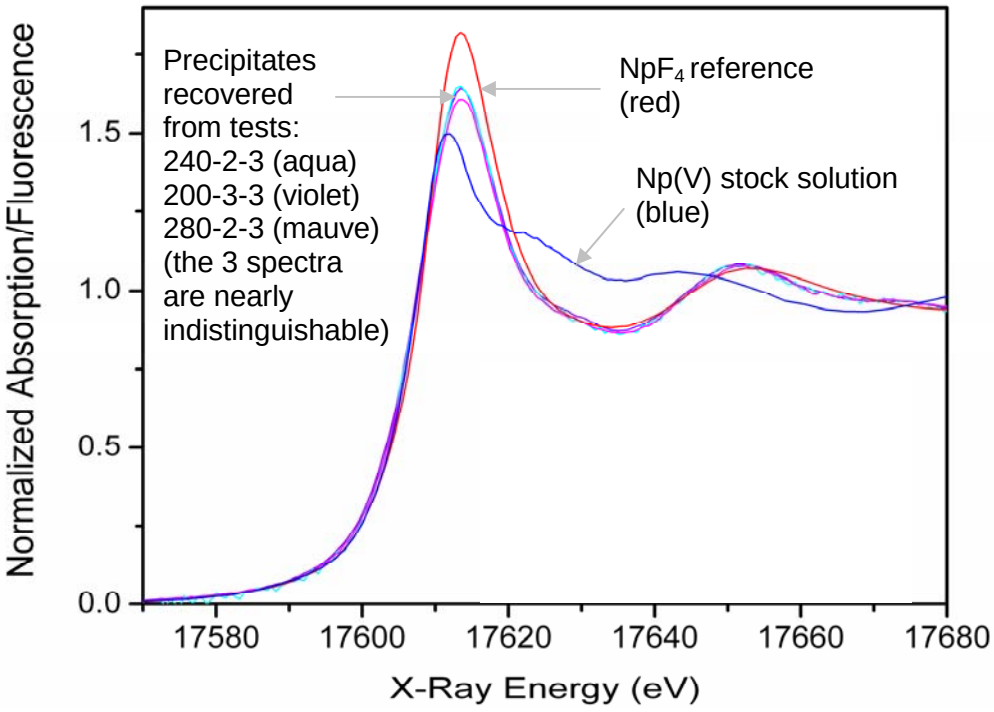

Figure 3.9. XANES Spectra of Solids Recovered from Samples 200-3-3, 240-2-3, and 280-2-3, an NpF_4 Reference Material, and the Np(V) Stock Solution

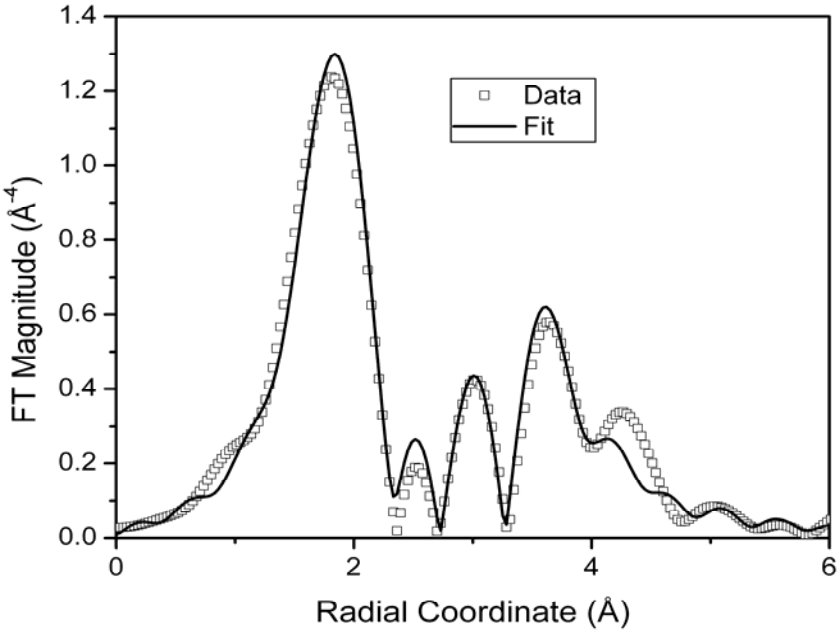

Figure 3.10. Fourier Transform Spectrum for Sample 200-3-3 (squares) and Model Fit (line)

3.3.4 Homogeneous Precipitation Batch Tests, Teflon Liners

The test execution data for the batch tests conducted at 200ºC are summarized in Table 3.9. These tests were performed using Teflon liners and separate tests were conducted for each duration. The Teflon liners used in the series of batch tests had a cover that contained water during the test and when the vessel was cooled. Water was not detected outside the cup when the vessels were opened. However, as shown in Table 3.9, almost 1 g of water was lost due to vessel leakage through 71 days. This will affect the total amount of Np sequestered in the precipitates, but not the Np concentration in the test solution under near-steady-state conditions.

Table 3.9. Test Execution Data for Homogeneous Precipitation Batch Tests, Teflon Liners

Test Number	Vessel Tare, g	Total Initial Weight, g	Initial Np Solution Weight, g	Sample Date[a]	Interval Duration, d	Total Final Weight, g	Weight Change, g	Final Np Solution Weight, g
200-2-1	1046.46	1054.47	8.01	8/31/2005	1.83	1054.46	-0.01	8.00
200-2-2	1046.54	1054.59	8.05	9/6/2005	8	1054.55	-0.04	8.01
200-2-3	1046.05	1054.12	8.07	9/15/2005	17	1054.08	-0.04	8.03
200-2-4	1046.24	1054.27	8.03	9/21/2005	23	1054.21	-0.06	7.97
200-2-5	1043.56	1051.58	8.02	9/28/2005	30	1051.42	-0.16	7.86
200-2-6	1045.83	1053.87	8.04	10/13/2005	45	1053.52	-0.35	7.69
200-2-7	1044.59	1052.67	8.08	11/28/2005	71	1051.74	-0.93	7.15

[a]All tests were started 8/29/2005.

The results of the batch tests at 200ºC are summarized in Table 3.10. The counting uncertainties in the gamma spectroscopy analyses are 1.6%, 3.6%, 1.4%, 0.52%, 2.2%, 0.52%, and 0.77% for increasing sample numbers. Essentially all the Np has precipitated within the shortest test duration. The dissolved concentration increases slightly at the longest test durations. This difference is not expected to be due to the loss of water: test 200-2-6 lost 4.4% of its water and test 200-2-7 lost 11.5% of its water. The average concentration of the first 5 tests is 4.04E-6 M, and the concentrations in tests 200-2-6 and 200-2-7 are 2.3-times and 3.3-times the average.

Table 3.10. Solution Results for Homogeneous Precipitation Batch Tests, Teflon Liners

Test and solution sample number	Test duration, d	pH	^{237}Np in filtrate solution		Decrease in ^{237}Np conc. due to precipitation, moles/L	Decrease in amount of dissolved Np, %
			^{237}Np activity, µCi	^{237}Np, moles/L		
200-2-1	1.83	4.72	9.320E-04	3.03E-06	9.928E-05	97.04%
200-2-2	8	6.16	7.444E-04	2.27E-06	1.000E-04	97.78%
200-2-3	17	5.94	1.068E-03	3.13E-06	9.918E-05	96.94%
200-2-4	23	4.31	2.919E-03	8.13E-06	9.418E-05	92.06%
200-2-5	30	5.54	1.352E-03	3.66E-06	9.865E-05	96.43%
200-2-6	45	4.20	3.709E-03	9.30E-06	9.301E-05	90.91%
200-2-7	71	3.98	6.583E-03	1.33E-05	8.903E-05	87.02%

Water loss cannot account for the higher-than-average concentrations measured in test solutions 200-2-6 and 200-2-7. Although the Teflon liners were cleaned before use, it is possible that small amounts of F were leached during the test and lead to the formation of NpF_4.

3.3.5 Heterogeneous Precipitation Test

The test solution recovered from the heterogeneous precipitation test in the presence of UO_2 had a measured concentration of 3.4×10^{-5} M Np(V) and the pH was 8.24. About 67% of the Np was removed from solution within 4 days, and was either precipitated or sorbed to the UO_2. The 9.53 mL of stock solution contains 9.75×10^{-7} moles of Np; 67% of this is 6.53×10^{-7} moles, which corresponds to 3.73×10^{17} atoms. Although the surface area occupied by a sorbed Np species is not known, a uniform monolayer containing this much Np would require an impossibly small area of 0.025 Å^2 for each sorbed Np atom. Because the solution was sampled at only one duration, it is not known if this is near the steady-state concentration. The surface of the UO_2 recovered from the heterogeneous precipitation test was analyzed with XANES at the APS. Figure 3.11 shows that spectrum and the spectra of NpO_2 (solids from sample 240-2-3) and a Np(V) carbonate reference material. Comparison with the reference spectra indicates that the solids present on the UO_2 sample contain both Np(IV) and Np(V). This is consistent with the co-precipitation of more than one phase, or one phase may be replacing the other over time.

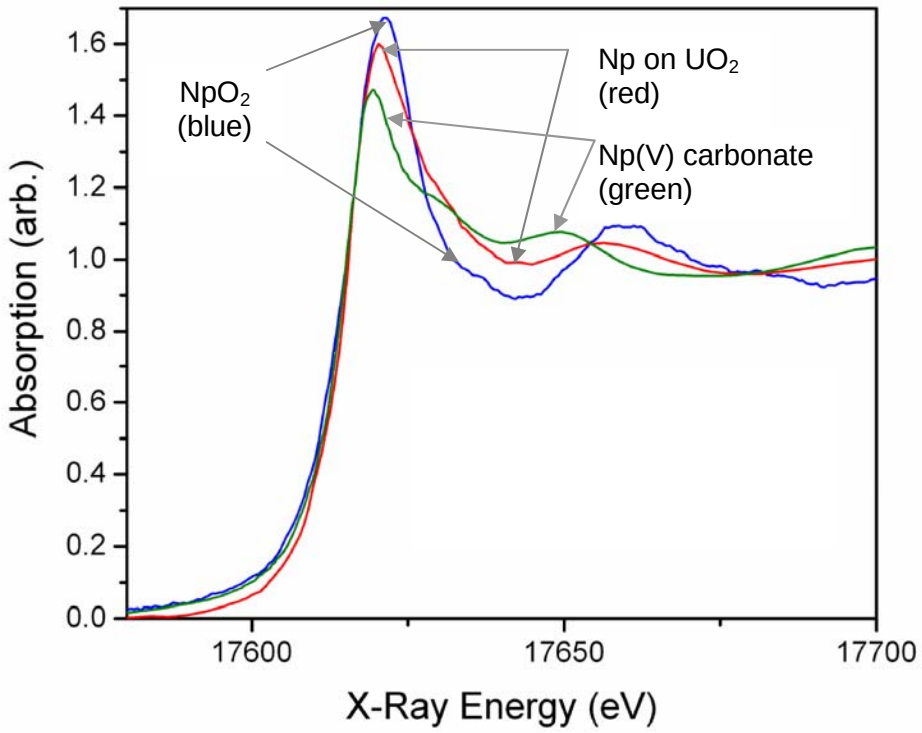

Figure 3.11. XANES Spectra of Np on UO_2 Surface after Exposure to Np(V) Solution at Room Temperature, $Np(IV)O_2$, and $(Np(V)O_2)_2CO_3$

3.4 DISCUSSION

The results of this Task are considered in the following order: (1) comparison of the results of various tests at 200ºC; (2) comparison with Roberts et al. (2003); (3) temperature effects; (4) estimation of activation energy for precipitation; and (5) analysis of precipitated phases.

3.4.1 Comparison of Argonne Tests at 200ºC in Borosilicate, Quartz, and Teflon Liners

The dissolved Np concentrations that were measured in batch tests and serially sampled tests in borosilicate glass and quartz liners conducted at 200ºC are plotted in Figure 3.12. The decrease in the dissolved concentration (due to precipitation) is seen to occur much faster in serially sampled tests run in borosilicate glass liners than those run in quartz liners, and lower concentrations are reached. The average of the concentrations attained in the 12-, 21-, and 68-day samples of the test in quartz is 1.70×10^{-5} M, and the average of the three samples of the test in borosilicate glass liner is 1.44×10^{-6} M. The decrease in the Np concentration is also rapid in the batch tests in Teflon. The short-term tests in Teflon reach Np concentrations similar to those in the borosilicate glass liner, but the longer-term tests attain higher concentrations similar to those maintained in the tests in quartz liners. Higher solution pH values were maintained in tests in the glass liners (about pH 8) than in tests in the quartz liner (about pH 4.5) or in Teflon (about

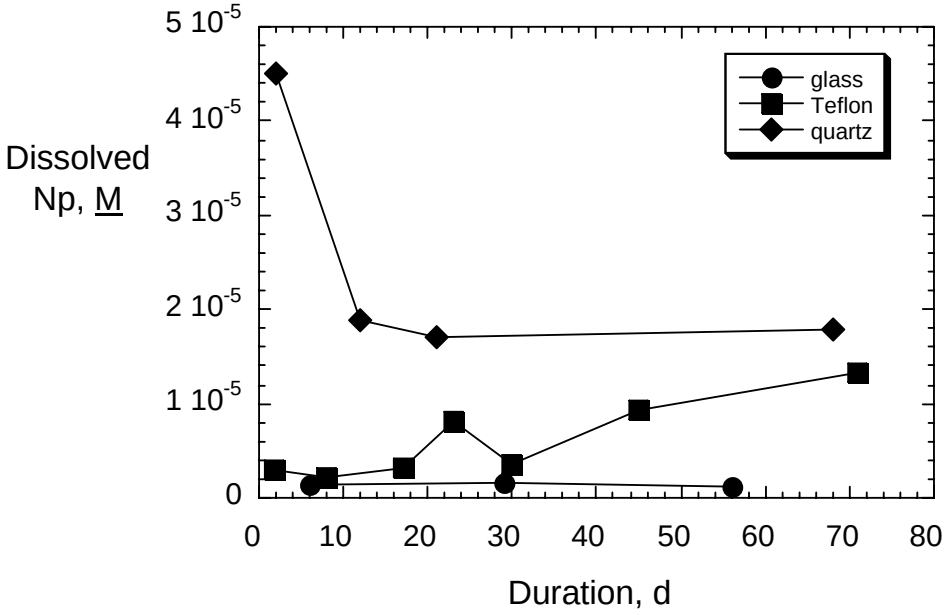

Figure 3.12. Results of Homogeneous Precipitation Tests Conducted as Serially Sampled Tests with a Borosilicate Glass (●) or Quartz (◆) Liner and Batch Tests with Teflon Liners (■)

pH 4 but scattered). The corrosion of the borosilicate glass liner is probably responsible for the increase in the pH, and also the abundance of silica colloids seen in those tests. Both the high pH and colloids could affect the dissolved concentration of Np, and the results of the tests conducted with borosilicate glass liners are not considered further.

The cause of the slow increase in concentration after the initial rapid decrease seen in the short-term batch tests in Teflon is not yet understood. Teflon is not expected to catalyze precipitation, although the presence of any surface can affect precipitation and the impact of leached F is not known. The air was refreshed in the interrupted tests at every sampling, whereas the air in the batch tests was not. However, the slight buildup of O_2 that occurred in the vessels of the batch tests is expected to slow the precipitation of NpO_2, according to Equation 3.1. The slightly higher solution pH conditions in the batch tests may have affected the equilibrium Np concentration: the 8-, 17-, and 30-day tests had higher-than-expected pH values and lower-than-expected Np concentrations. (Recall the tests with borosilicate glass liners also attained higher pH values and lower Np concentrations than the tests in the quartz liners.) The concentrations in tests conducted in Teflon appear to be approaching the steady-state concentration reached in tests in quartz liners after about 71 days.

3.4.2 Comparison of Argonne Tests at 200 ºC in Quartz Liners with Roberts et al. (2003)

Precipitation occurs faster in both the serially sampled and batch tests conducted at Argonne than in the serially sampled test of Roberts et al. (2003). Figure 3.13 shows the results of Roberts et al. plotted with the results of corresponding serially sampled test at 200ºC. The

initial concentrations were essentially the same in both series of tests: 1.00 x 10^{-4} M in the Roberts et al. tests and 1.02 x 10^{-4} M in the tests conducted at Argonne. The initial solution used by Roberts et al. was stated to have a pH value of 6-6.5, whereas our solution had a measured pH of 6.0. Essentially the same steady-state Np concentrations are reached in both tests, although it is reached after only about 12 days in the tests conducted at Argonne (filled squares) but not until about 60 days in the tests of Roberts et al. (open squares).

Roberts et al. (2003) regressed their data with a first-order precipitation equation,

$$[Np] = \left([Np]_o - [C]\right) e^{-kt} + [C], \tag{3.5}$$

where *[Np]* is the aqueous Np concentration at time *t*, $[Np]_o$ is the initial aqueous Np concentration, *k* is a first order rate constant at 200 ºC, and *[C]* is the steady-state aqueous Np concentration that is attained (Roberts et al. 2003). They determined that $k = 0.0736$ d^{-1} for their results at 200ºC. The more rapid approach to the steady-state dissolved concentration in the tests conducted at Argonne suggests a higher value of *k*, and regressing Equation 3.5 to the data from the serial test run in a quartz liner (see Figure 3.14) gives a value $k = 0.374$ d^{-1}.

Why the tests by Roberts et al. (2003) and those conducted at Argonne reach steady state after different durations is not yet understood. Despite the small difference in the times required to attain steady state, the actual steady-state concentrations that are reached in the serially sampled tests are in excellent agreement. Likewise, the concentration attained in the static tests conducted at Argonne were significantly lower than in the test by Roberts et al. (2003) in the early samplings, but in good agreement in the longer-term samplings. This suggests that there is some unidentified and uncontrolled factor in the test equipment or procedure that accelerated the precipitation of NpO_2 in both the serially sampled and batch tests, but resulted in formation of the same solid phase(s) and attainment of the same solubility limit. The most obvious difference is that passivated titanium reaction vessels were used by Roberts et al. (2003), whereas borosilicate glass, quartz, and Teflon liners were used in the tests conducted at Argonne. The use of glass, quartz, and Teflon was intended, in part, to electrically isolate the solution. This may have resulted in slightly different test conditions that affected the reduction of Np(V) to Np(IV) necessary for the formation of NpO_2. The initial pH of the solution in the Roberts et al. (2003) test is uncertain, since the text indicates a range of pH 6-6.5 for the initial leachant solution, but a value of 6.5 ± 0.5 is plotted at 0 days with the results in Figure 1 of Roberts et al. (2003). According to Equation 1, a solution with a lower pH is expected to **slow** the precipitation reaction. This was seen in the current set of tests: the solutions from the test in a quartz liner had lower pH values and evidenced slower Np precipitation than the solutions in the corresponding test in a borosilicate glass liner; however, similar pH values were measured in the sampled solutions in the test by Roberts et al. (2003) and the test in a quartz liner, so the possible difference in the pH of the leachant solution is not believed to be a significant factor.

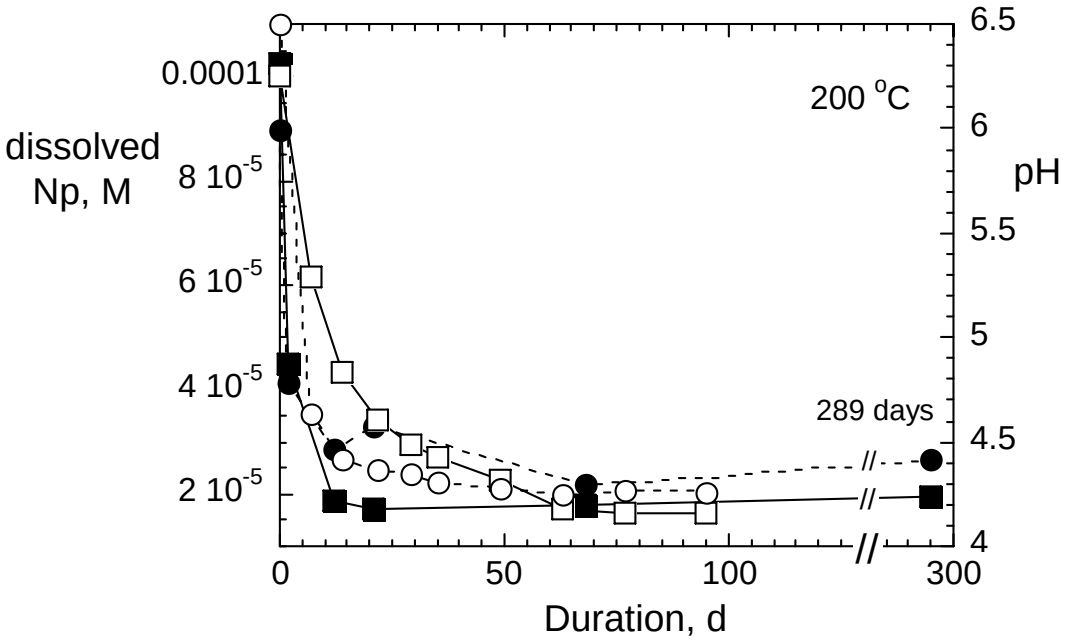

Figure 3.13. Comparison of the Results of Serial Tests at 200ºC (filled symbols) with Results of Roberts et al. (open symbols): Np concentration (■) and pH(RT) (●)

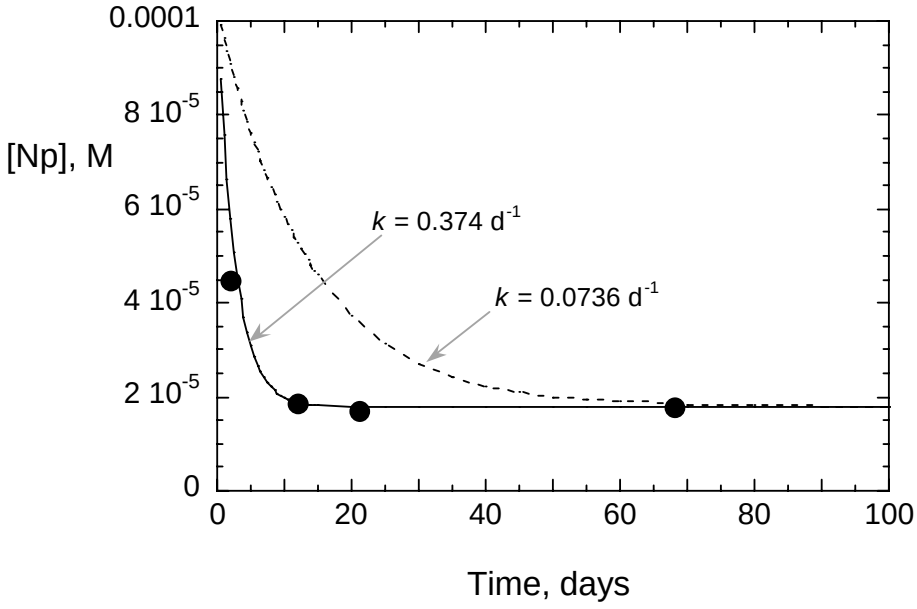

Figure 3.14. Regression of Eq. 3.5 to Results of Tests at 200ºC. The dashed line shows the fit with the rate constant determined by Roberts et al. (2003)

3.4.3 Temperature Effects in Argonne Tests with Quartz Liners

The results of the serially sampled homogeneous precipitation tests run in quartz liners at different temperatures are plotted together in Figure 3.15 and the measured steady-state concentrations are shown. Whereas the concentrations attained in tests at 200, 240, and 280ºC are probably controlled by a precipitated Np-bearing phase(s), the concentrations in the test at 150ºC may reflect the uncertainty in measuring the Np concentration. The uncertainty in the Np concentrations measured by gamma spectroscopy were about 2% for 3-day sampling and 1% or less for the other samplings. Uncertainty bars are drawn at 5% in Figure 3.15 to take into account the added uncertainty in test execution (e.g., measuring solution masses). As mentioned earlier, the Np concentration measured in the 150ºC test after 289 days was higher than that measured in the initial solution, and the difference exceeds the testing and analytical uncertainties and what can be attributed to the loss of water during the test. Re-analysis of that solution confirmed the result. The steady-state concentrations attained within 68 days in tests at 200, 240, and 280ºC provide some insight into the concentrations that would be expected at 150ºC if the same Np-bearing phase(s) formed and controlled the solution concentration. While it is not certain if precipitation occurred at 150ºC over the 289-day test period, precipitation occurred within 4 days at room temperature (about 24 ºC) in the presence of UO_2 to leave a residual solution having a concentration of 3.4×10^{-5} M Np(V). Although sampling of the test solution is available for only a 4-day period, that concentration is assumed to be an upper bound to the steady-state concentration at 24ºC. Analyses of the solids indicates that the same phases form in the test with UO_2 and in the high temperature homogeneous precipitation tests. The measured steady-state concentrations in tests at 200, 240, and 280ºC and the concentration attained in the room-temperature test in the presence of UO_2 are plotted against temperature in Figure 3.16. The data show a retrograde solubility for the controlling phase(s); that is, the

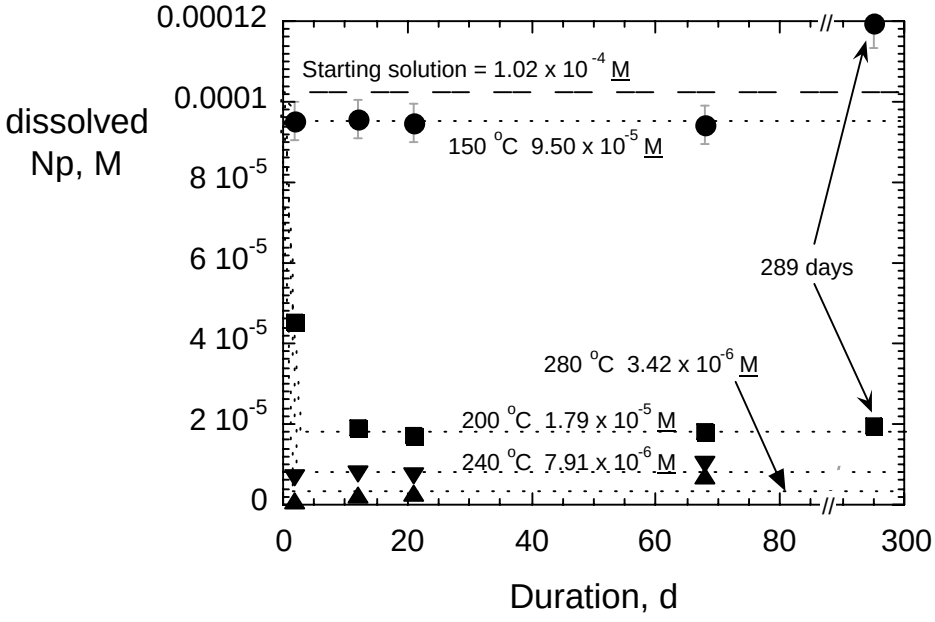

Figure 3.15. Dissolved Np Concentrations in Serial Tests at Different Temperatures

dissolved concentration of Np(V) decreases with increasing temperature. Regressing the steady-state concentrations with an empirical fit (solid line) gives a predicted Np concentration of 2.04 x 10^{-5} M at 150ºC. This fit is not intended to imply a mechanism or analytical temperature dependence of the measured concentrations. Instead, it is intended to estimate the saturation limit likely to be imposed by the phase(s) formed at high temperatures (and presumably also at room temperature) at 150ºC. The predicted value is below the concentrations measured in the test solutions from the 150ºC tests (9.5 x 10^{-5} M). This is interpreted to indicate that either the solutions attained in the 150 C tests remain oversaturated with respect to the phase(s) formed at higher temperatures and their precipitation is inhibited, or those phase(s) do not control the dissolved concentration 150ºC.

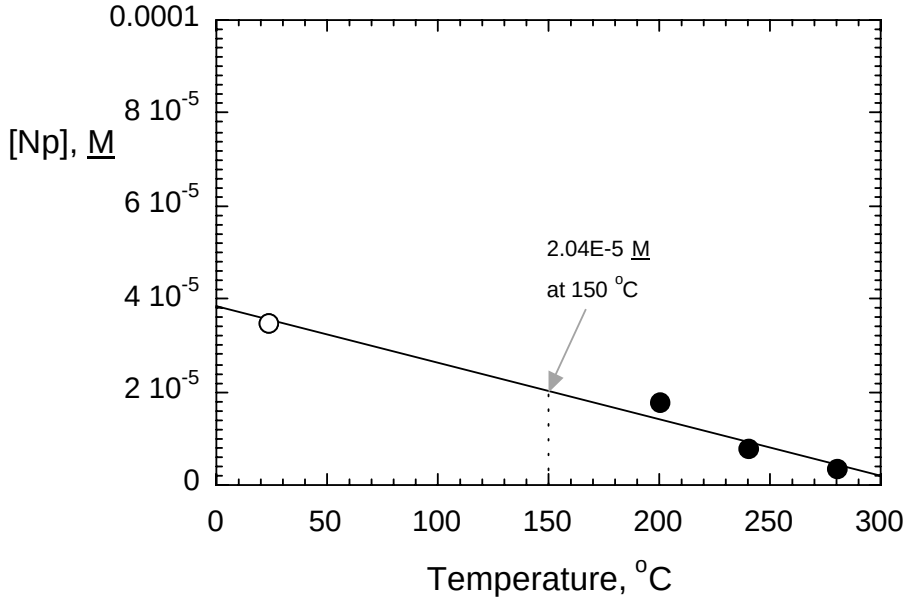

Figure 3.16. Steady-State Np Concentrations Measured for Tests at Different Temperatures (●) and Concentration in the Presence of UO_2 (O)

From the table "Dissolved Concentration Limits of Radioactive Elements AMR" (Table 6.6-1 in BSC 2005a), which assigns a pH dependence but not a temperature dependence to the Np concentrations, the dissolved concentrations as controlled by NpO_2 are 4.7 x 10^{-5} M at pH 5.0, 1.5 x 10^{-5} M at pH 5.5, 1.5 x 10^{-4} M at pH 4.5, and 4.7 x 10^{-5} M at pH 5.0, which are the approximate pH values attained in tests at 280, 240, 200, and 150ºC, respectively. The modeled solubility is 4.6 x 10^{-8} M at pH 8.25, which is the pH attained in the test with UO_2. (The molar concentrations were calculated from the solubilities given in the table in units of mg/L using the factor 4.219 M/(mg/L).) The 1.023 x 10^{-4} M stock solution itself is oversaturated with respect to NpO_2 according to the "Dissolved Concentration Limits of Radioactive Elements" model: the modeled solubility at pH 6.0 is 4.7 x 10^{-6} M.

3.4.4 Activation Energy for Np Precipitation

Our intended approach was to determine rate constants from the changes in the Np concentrations measured at different temperatures by using Equation 3.5 (presuming the data would support a first-order precipitation model), and then apply the Arrhenius equation using

those rate constants to determine the effective activation energy. The experimentally determined activation energy would have been considered an effective energy, since it would describe a complex process involving a chemical reduction step as well as precipitation (though not necessarily in that order). The higher-than-expected precipitation rate seen in the 200ºC test with the quartz liner, as compared to the results of Roberts et al. (2003), reduced the usefulness of the tests at higher temperatures for this purpose—that is, the temperatures and sampling times selected for the tests were based on an expectation that steady-state (saturation) would be reached after about 60 days at 200ºC, and the sampling schedule became inappropriate when saturation was reached in less than 12 days. The data sets from tests at 240 and 280ºC are not sufficient to estimate the rate constants needed to determine the temperature dependence, since the steady-state solution concentrations were reached within the first sampling interval of 2 days. Although the results of tests at 150ºC showed a decrease in the Np concentration (at least through 68 days), the decrease is smaller than expected (as discussed in Section 4.3), and does not necessarily indicate that precipitation has occurred. The currently available database is not sufficient to determine an activation energy using rate constants determined at various temperatures. (A crude estimate of activation energy is made in Appendix A, section A.3.)

3.4.5 Comments on Mechanism

While it is not certain if precipitation occurred at 150ºC over the 289-day test period, precipitation did occur within 4 days at room temperature in the presence of UO_2 to leave a residual solution having a concentration of 3.4×10^{-5} M Np(V). Examination of the solids indicates they are a mixture of the same phases that formed in the homogeneous precipitation tests at high temperatures. This suggests that UO_2 catalyzes the precipitation, but it is not expected to affect the solubility of the precipitated phase(s). As mentioned earlier, the oxidation of uranium promotes the reduction of neptunium and the UO_2 structure can act as a template to facilitate the formation of NpO_2. The UO_2 can affect both the reduction and nucleation steps in the formation of NpO_2.

The amount of Np lost from solution due to precipitation of NpO_2 was expected to be correlated with the pH through the generation of H^+ according to Equation 3.1. The hydrogen ion concentrations in the samples of the test solutions were calculated from the measured pH values, and the amounts of H^+ generated during the tests were calculated by subtracting 1.00×10^{-6} M, which is the concentration of H^+ in the stock solution based on the measured pH value of 6.00. The H^+ concentrations are compared directly with the concentrations of Np removed by precipitation (in tests at 200, 240, and 280ºC) in Figure 3.17. (The decrease in Np concentration in the 150ºC test is included for completeness, even though it is suspected that precipitation did not occur. The results for sampling 240-2-4 are not shown in the plot because the pH increased to 7.31, so that $[H+] = 4.9 \times 10^{-8}$ M.) The uncertainty bars are drawn conservatively at 10% for the H^+ concentration and 5% for the Np concentration. The dashed line marks the 1:1 correspondence expected based on Equation 3.1, in which H^+ is a product of the precipitation reaction. No correlation is seen between the concentrations of Np and H^+ in the plotted results.

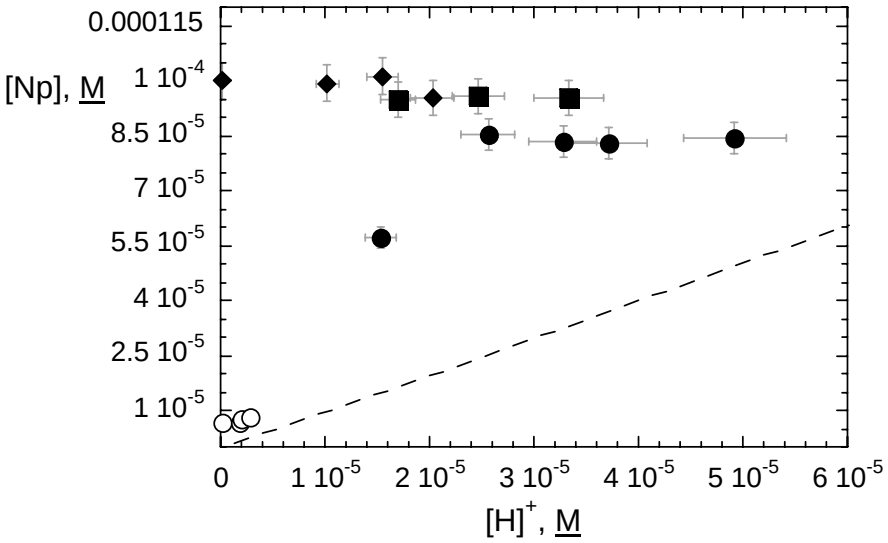

Figure 3.17. Correlation Between [Np] Removed from Solution by Precipitation and pH in Serially Sampled Tests at (O) 150ºC, (●) 200ºC, (■) 240ºC, and (◆) 280ºC

Finally, we note that only NpO_2 was detected in the homogeneous precipitation tests in the quartz liner, but the solids formed in tests in borosilicate glass liners had a small amount of Np(V) character and the solids formed in the presence of UO_2 had similar amounts of Np(IV) and Np(V) character. This suggests that UO_2 facilitates the precipitation of NpO_2 by reducing the dissolved Np(V) to Np(IV), but also facilitates the nucleation of Np_2O_5. It has been presumed that the kinetically favored Np_2O_5 phase will be replaced by the thermodynamically more stable phase NpO_2 (Roberts et al. 2003), but this remains to be demonstrated.

In summary, the homogeneous precipitation tests have shown that solids precipitate from a 1 x 10^{-4} M Np(V) solution over the temperature range of 200–280ºC, but no evidence was found that any solids precipitated from the same solution at 150ºC through 289 days. The solids were predominantly a Np(IV)-bearing phase, probably NpO_2. The activation energy for homogeneous precipitation over this temperature range could not be determined from the test results. The presence of UO_2 resulted in precipitation at room temperature of a solid containing similar amounts of Np(IV)- and Np(V)-bearing phases, probably NpO_2 and Np_2O_5. Although the UO_2 is presumed to act as a reducing agent for Np(V) that facilitates the formation of NpO_2, it also appears to facilitate the nucleation of a Np(V)-bearing phase (probably Np_2O_5).

3.5 REFERENCES FOR SECTION 3

BSC (Bechtel SAIC Company), "Dissolved Concentration Limits of Radioactive Elements," ANL-WIS-MD-000010 Rev. 05, Bechtel SAIC Company, LLC, Las Vegas, Nevada (2005a).

BSC, "Technical Work Plan for Waste Form Testing," TWP-WIS-MD-000018 REV 00, Bechtel SAIC Company, LLC, Las Vegas, Nevada (2005b).

BSC, "In-Package Chemistry Abstraction," ANL-EBS-MD-000037 Rev. 04 Bechtel SAIC Company, LLC, Las Vegas, Nevada (2005c).

R. W. Barnard, M. L. Wilson, H. A. Dockery, J. H. Gauthier, P. G. Kaplan, R. R. Eaton, F. W. Bingham, and T. H. Robey, "TSPA 1991: An Initial Total-System Performance Assessment for Yucca Mountain," Report SAND 91-2795, Sandia National Laboratories, Albuquerque, New Mexico (1992).

D. W. Efurd, W. Runde, J. C. Banar, D. R. Janecky, J. P. Kaszuba, P. D. Palmer, F. R. Roensch, and C. D. Tait, "Neptunium and Plutonium Solubilities in a Yucca Mountain Groundwater," Environmental Science and Technology **32**, 3893-3900 (1998).

R. J. Finch, "Precipitation of Crystalline NpO_2 During Oxidative Corrosion of Neptunium-Bearing Uranium Oxides," Proceedings of the Materials Research Society Symposium Scientific Basis for Nuclear Waste Management XXV held November 26-29, 2001 in Boston, Massachusetts, B. P. McGrail and G. A. Cragnolino, eds., pp. 639-646 (2002).

J. P. Kaszuba and W. H. Runde, "The Aqueous Geochemistry of Neptunium: Dynamic Control of Soluble Concentrations with Applications to Nuclear Waste Disposal," Environmental Science and Technology **33**, 4427-4433 (1999).

Katz, Seaborg, and Morss (eds.), *Chemistry of the Actinide Elements*, Vol.1, 2nd edition, Chapman and Hall, New York, New York (1986).

H. Nitsche, R. C. Gatti, E. M. Standifer, S. C. Lee, A. Müller, T. Prussin, R. S. Deinhammer, H. Maurer, K. Becraft, S. Leung, and S. A. Carpenter, "Measured Solubilities and Speciations of neptunium, Plutonium, and Americium in a Typical Groundwater (J-13) from the Yucca Mountain Region," LA-12562-MS, Los Alamos National Laboratory Report, Los Alamos New Mexico (1993a).

H. Nitsche, K. Roberts, T. Prussin, D. Keeney, S. A. Carpenter, K. Becraft, and R. C. Gatti, "Radionuclide Solubility and Speciation Studies for the Yucca Mountain Site Characterization Project," Proceedings of the International High-Level Radioactive Waste Management Conference **2**, 1490-1495 (1993b)

K. E. Roberts, T. J. Wolery, C. E. Atkins-Duffin, T. G. Prussin, P. G. Allen, J. J. Bucher, D. K. Shuh, R. J. Finch, S. G. and Prussin, "Precipitation of Crystalline Neptunium Dioxide from Near-Neutral Aqueous Solution," Radiochimica Acta **91**, 87-92 (2003).

C. N. Wilson and C. J. Bruton, “Studies on Spent Fuel Dissolution Bbehavior under Yucca Mountain Repository Conditions,” American Ceramic Society **9**, 423 (1989).

C. N. Wilson, "Results from NNWSI Series 2. Bare Fuel Dissolution Tests," Report PNL7169, Pacific Northwest National Laboratory, Richland, Washington (1990a).

C. N. Wilson, "Results from NNWSI Series 3. Spent Fuel Dissolution Tests," Report PNL-7170, Pacific Northwest National Laboratory, Richland, Washington (1990b).

APPENDIX A. MISCELLANEOUS CALCULATIONS

A.1 DETERMINATION OF Np(V) CONCENTRATION IN STOCK SOLUTION

A 5.5812-g sample of the Np(V) stock solution had a measured activity of 0.095455 μCi. The specific activity of ^{237}Np is 7.054 x 10^{-4} Ci/g, so in 5.5812 g of stock solution there is

$$\frac{0.095455\ Ci}{7.054\times10^{-4}\ Ci/g\ Np} = 1.353\times10^{-4}\ g\ Np\ . \tag{A-1}$$

The Np concentration is

$$\frac{1.353\times10^{-4}\ g\ Np}{5.5812\ g\ solution} = 2.425\times10^{-5}\ g\ Np/g\ solution. \tag{A-2}$$

Assuming a solution density of 1 g/cm^3, the Np concentration is

$$\frac{1.353\times10^{-4}\ g\ Np}{5.5812\ g\ solution}\times\frac{1\ mole\ Np}{237\ g\ Np}\times\frac{1\ g\ solution}{1\times10^{-3}\ L\ solution} = 1.023\times10^{-4}\ M. \tag{A-3}$$

A.2 AMOUNTS OF WATER IN SATURATED STEAM IN VESSELS AT TEST TEMPERATURES

The amount of water that evaporates to fill the air space in a test vessel with saturated steam was calculated using the specific volume of steam at the various test temperatures and the estimated air spaces in the assembled vessels. The specific volumes were taken from the CRC Handbook (Weast 1975). The test temperatures were converted to degrees-Fahrenheit using Equation A-4,

$$°F = °C \bullet \frac{5}{9} + 32\ . \tag{A-4}$$

The inverse of the specific volume was converted to units of g/cm^3 using Equation A-5,

$$\frac{lb}{ft^3}\bullet\frac{ft^3}{12^3\ in.^3}\bullet\frac{in.^3}{2.54^3\ cm^3}\bullet\frac{2.2\ kg}{lb}\bullet\frac{10^3\ g}{kg} = \frac{0.07769\ g}{cm^3}\ . \tag{A-5}$$

The estimated air volumes were multiplied by 0.07769 g/cm^3 to calculate the masses of water that evaporated to saturate the vessels at the test temperatures. The results are shown in Table A-1.

Table A-1. Calculated Amounts of Saturated Steam in Test Vessels

Temperature		Specific volume, ft^3/lb	1/sp vol		Mass water in 25 cm^3 air, g	Mass water in 45 cm^3 air, g
ºC	ºF		lb/ft^3	g/cm^3		
150	302	6.2861	0.159	0.0124	0.30	0.56
200	392	2.0369	0.491	0.0381	0.95	1.7
240	464	0.95557	1.05	0.0813	2.0	3.7
280	536	0.48257	2.07	0.161	4.0	7.2

A.3 ESTIMATION OF AN EFFECTIVE ACTIVATION ENERGY

Although the effective activation energy for precipitation could not be calculated from the current data set, the activation energy can be roughly approximated by using the empirical rates obtained by dividing the amount of Np that precipitated from the initial 1.02×10^{-4} M solution to reach the steady-state Np concentrations that were measured at different temperatures by the time required to reach steady state. This method neglects the differences in the saturation concentrations at different temperatures (i.e., the differences in the amounts of Np that had to precipitate) and requires a subjective definition of the time required to reach saturation. This estimation is performed to see if the assumption that homogeneous precipitation at near-ambient temperatures can occur during the repository service life is unreasonable; that is, if a physically unreasonable (effective) activation energy would be required for precipitation to occur at repository temperatures.

The test data used to estimate the (effective) activation energy are summarized in Table A-2. Values are listed with "less than" or "greater than" signs to indicate whether steady state is believed to be attained before or after that test duration, respectively. Steady state is attained within the first test interval in tests at 280 and 240ºC. We assume that steady state was reached earlier in the test at 280ºC than in the test at 240ºC, and exclude the 280ºC test result from the analysis of the (effective) activation energy. Steady state was reached within 2 days in the test at 240ºC, and so the data point for the 240ºC test is considered to be a lower bound for the precipitation rate at 240ºC. The steady-state concentration is reached within about 12 days in the 200ºC test. The natural logarithms of the estimated rates are plotted against the reciprocal of the test temperature in Figure A-1. The results of the test at 150ºC indicate saturation has not been reached after 289 days (precipitation probably does not occur at all). For the purpose of estimating a bounding (effective) activation energy, the steady-state concentration at 150ºC is taken to be the average of the first 4 samplings, which is 9.50×10^{-5} M. Also plotted in Figure A-1 is the rate based on the time needed to reach saturation in the tests of Roberts et al. (2003).

Using the results of tests conducted at Argonne at 240 and 200ºC as bounding values, the activation energy is calculated to be 96.3 kJ/mol. Extrapolation of this fit to 90 and 25ºC give rates of 3.1×10^{-9} and 2.9×10^{-12} M/d, which are 2270 and 2,420,000 times slower than the rate at 200ºC. The precipitation rate at 150ºC is predicted to be 3.81×10^{-7} M/d using this activation energy. To estimate an upper bound to the activation energy, the data point for the 150ºC test is considered to be a conservative upper bound for the precipitation rate at 150ºC. As shown in

Figure A-1, use of the results of the 240ºC and 150ºC tests as bounding values gives an effective activation energy of 151 kJ/mol. From the plot in Figure A-1, the 63-day saturation time measured by Roberts et al. (2003) is (fortuitously) consistent with this approximation.

Although there is a very high level of uncertainty associated with these values, they do indicate that homogeneous precipitation has a high effective activation energy, and that homogeneous precipitation will be extremely slow at repository-relevant temperatures, if it occurs at all. The difference in the rates determined from the results of Roberts et al. (2003) and the Argonne results indicates there is a small effect of the vessel or other uncontrolled experimental variable on the reduction, nucleation, and/or precipitation reactions. Until these effects are understood, it is premature to use the effective activation energy determined from this analysis to infer precipitation rates at ambient temperatures.

Table A-2. Data Used in Arrhenius Plot

Temp. ºC	1/RT, 1/(kJ/mol)	Np in Solution at Steady State, M	Np Removed from Solution at Steady State, M	Time to Saturation, days	Rate, M/d	ln Rate
150	0.2843	9.50E-5	7.27E-6	Not attained	<3.63E-5	<-12.52
200	0.2543	1.79E-5	8.44E-5	<12	>7.03E-6	>-11.87
200	0.2543	1.79E-5	8.44E-5	<63[a]	>1.34E-6	>-13.52
240	0.2345	7.91E-6	9.44E-5	<2	>4.72E-5	>-9.96
280	0.2175	3.42E-6	9.89E-5	<2?	>9.94E-5	>-9.91

[a]Time to saturation measured by Roberts et al. (2003)

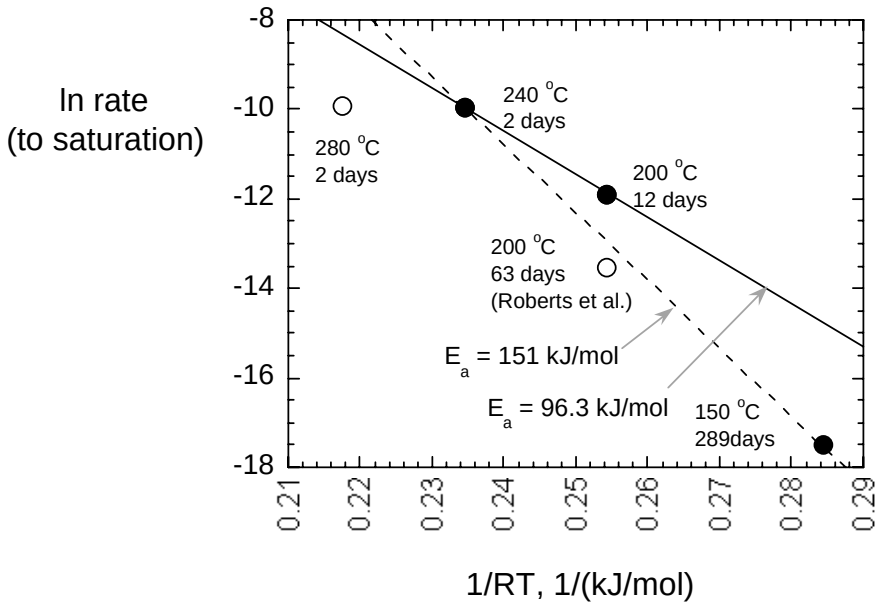

Figure A-1. Arrhenius Plot of Rates to Reach Steady-State Concentrations during Homogeneous Precipitation (see text)

REFERENCES

K. E. Roberts, T. J. Wolery, C. E. Atkins-Duffin, T. G. Prussin, P. G. Allen, J. J. Bucher, D. K. Shuh, R. J. Finch, and S. G. Prussin, "Precipitation of Crystalline Neptunium Dioxide from Near-Neutral Aqueous Solution," Radiochimica Acta **91**, 87-92 (2003).

R. C. Weast (ed.), *Handbook of Chemistry and Physics*, 56th edition, CRC Press, Inc., Cleveland, Ohio (1975)

APPENDIX B: RESULTS OF ELECTRON DIFFRACTION ANALYSES

Table B-1. Results of Electron Diffraction Analyses of Suspended Solids Recovered from Test Solutions, d-spacings in Å

Sample 200-3-1					Sample 240-2-1			Sample 240-2-2				Reference Materials			
200-3-2.1	200-3-2.2	200-3-2.3	200-3-2.4	200-3-2.5	240-2-1a.d	240-2-1a	240-2-1.2	240-2-2a	240-2-2.1.b	240-2-2.2	240-2-2.b	NpO_2[a]	Np_2O_5[b]	Np_3O_8[c]	$NpO_3.H_2O$[d]
															4.98
													4.18	4.14	
															3.85
										3.50					
													3.47	3.45	
			3.42												
			3.39			3.39									
3.29	3.31					3.34							3.3		
3.26	3.26	3.26			3.29				3.26					3.27	
			3.16	3.19	3.19										
			3.14		3.14							3.14			3.14
						3.05									
					2.89	2.89	2.93								
								2.85							
								2.83							
2.81										2.81	2.79				2.803
					2.74										
						2.70						2.717			
													2.678		
			2.67		2.67								2.666		2.654
														2.66	
										2.61					2.599
										2.59			2.586	2.58	
															2.559
				2.46											2.487
															2.444
															2.275
					2.09								2.092	2.09	2.091
													2.043	2.04	
2.02			2.02			2.02									
					2.01										
						2.00			1.98						
															1.949
			1.94			1.94									1.927
												1.921	1.934	1.93	1.922
															1.861
													1.841		

Table B-1. (continued)

Sample 200-3-1					Sample 240-2-1			Sample 240-2-2				Reference Materials			
200-3-2.1	200-3-2.2	200-3-2.3	200-3-2.4	200-3-2.5	240-2-1a.d	240-2-1a	240-2-1.2	240-2-2a	240-2-2.1.b	240-2-2.2	240-2-2.b	NpO_2[a]	Np_2O_5[b]	Np_3O_8[c]	$NpO_3.H_2O$[d]
													1.831	1.83	
													1.796	1.79	1.797
					1.78								1.766	1.76	1.763
													1.757		
					1.75								1.754		
						1.74							1.73	1.73	
1.74		1.74				1.74	1.74								
1.72			1.72		1.72	1.72		1.72		1.72					
1.72	1.72														
1.71					1.71	1.71		1.71			1.71				
		1.70			1.70										
		1.68			1.68	1.68								1.65	1.687
						1.67					1.67				
						1.66				1.66	1.66				
	1.64	1.64	1.64			1.64							1.646		
1.63									1.63			1.638			
					1.62				1.62	1.62					
													1.607	1.6	1.6
			1.58												1.576
1.55												1.568			1.567
													1.531	1.53	
														1.5	1.495
										1.48			1.464	1.46	1.467
1.44							1.44								
						1.42									
						1.38		1.37			1.39				
					1.36	1.35	1.34	1.34				1.358			
					1.32					1.32					
1.30		1.31				1.31	1.31	1.31							
1.29	1.29	1.29	1.29			1.29				1.29				1.29	1.295
						1.28					1.28				
1.27			1.27		1.27				1.27		1.27			1.27	
		1.26			1.26						1.26				
	1.26	1.26	1.26												
						1.25						1.247			
						1.24									1.24
			1.22									1.215		1.2	1.214
	1.19		1.21												
1.16				1.16	1.16									1.16	
1.15	1.15					1.15									
1.15									1.15						
				1.14							1.14				

Table B-1. (continued)

Sample 200-3-1					Sample 240-2-1			Sample 240-2-2				Reference Materials			
240-2-2.c	240-2-3	240-2-2.3a	240-2-2.3.b.d	240-2-3a	240-2-.3	280-2-1	280-2-1.1a	280-2-1.2	280-2-1.2a	280-2-1.3	280-2-1.3a	NpO_2[a]	Np_2O_5[b]	Np_3O_8[c]	$NpO_3.H_2O$[d]
		1.14	1.14		1.14										
		1.12	1.13			1.13									
					1.11	1.11						1.109			
		1.10				1.10						1.1046			
1.08			1.08		1.08				1.08						
1.07			1.07		1.07	1.07									
						1.06									
						0.99	0.99								
							0.98								
								0.97							
							0.96	0.96							
		0.95													
											0.94				
											0.93				
							0.92								
						0.90									
											0.87				
								0.86							
								0.85							
			0.84												
											0.83				
							0.76	0.76							
									0.73						

Table B.1 (continued)

	Sample 240-2-3					Sample 280-2-2						Reference Materials			
240-2-2.c	240-2-3	240-2-2.3a	240-2-2.3.b.d	240-2-3a	240-2-.3	280-2-1	280-2-1.1a	280-2-1.2	280-2-1.2a	280-2-1.3	280-2-1.3a	NpO_2[a]	Np_2O_5[b]	Np_3O_8[c]	$NpO_3.H_2O$[d]
															4.98
					4.50										
		4.45													
				4.32											
	4.23			4.27											
													4.18	4.14	
						3.81									3.85
										3.50	3.47		3.47	3.45	
	3.34												3.3		
3.24	3.26			3.26		3.26								3.27	
3.14										3.14		3.14			3.14
		3.10													
					3.05										
			2.85	2.85	2.85										
			2.83												
			2.79												2.803
			2.77						2.76						
												2.717			
													2.678		
													2.666	2.66	2.654
					2.61										2.599
		2.57			2.59								2.586	2.58	
		2.56									2.57				2.559
											2.48				2.487
										2.40	2.40				2.444
		2.32			2.32										2.275
										2.18	2.12		2.092	2.09	2.091
										2.05			2.043		
	2.03			2.03						2.04	2.03			2.04	
										2.02					
	2.02														
				2.00							2.00				
1.98			1.98												1.949
						1.96		1.96							1.927
							1.94			1.94		1.921	1.934	1.93	1.922
					1.92										
1.89															1.861
		1.87											1.841		
			1.85										1.831	1.83	
						1.81							1.796	1.79	1.797

Table B.1 (continued)

	Sample 240-2-3					Sample 280-2-2						Reference Materials			
240-2-2.c	240-2-3	240-2-2.3a	240-2-2.3.b.d	240-2-3a	240-2-.3	280-2-1	280-2-1.1a	280-2-1.2	280-2-1.2a	280-2-1.3	280-2-1.3a	NpO_2[a]	Np_2O_5[b]	Np_3O_8[c]	$NpO_3.H_2O$[d]
										1.75	1.76	1.638	1.754		
			1.72							1.74	1.72		1.73	1.73	
			1.71			1.71					1.71				
	1.70		1.70			1.70									
			1.68												1.687
			1.67					1.67							
	1.64												1.646	1.65	
		1.63		1.63	1.62	1.62	1.61						1.607	1.6	1.6
															1.576
1.57												1.568			1.567
		1.54											1.531	1.53	
					1.50									1.5	1.495
		1.48											1.464	1.46	1.467
			1.42												
			1.41				1.38		1.41		1.41				
												1.358			
				1.31											
	1.30			1.30											1.295
	1.29	1.29		1.29	1.29						1.29			1.29	
			1.28											1.27	
1.26			1.26			1.26	1.26					1.247			
1.24			1.25		1.24	1.25	1.25								1.24
1.23		1.23						1.23				1.215		1.2	1.214
	1.17													1.16	
	1.15			1.15							1.15				
												1.109			
	1.10		1.10							1.10		1.1046			
	1.08		1.07	1.07			1.07								
1.05															
	0.96		0.95	0.95	0.95										
0.92		0.91	0.93		0.91		0.91		0.92	0.92	0.92				
0.90				0.89				0.89							
0.84							0.74								
0.75															
0.68															

[a]PDF 00-023-1269 Machiels, Thesis, University of Liège (1969)
[b]PDF 00-018-0871 Cohen, Walter, J. Chem. Soc. 2696 (1964).
[c]PDF 00-012-0013 Collins, Phillips. J. Inorg. Nucl. Chem. **6**, 67 (1958)
[d]PDF 00-019-0832 Bagnal, Laidler, J. Chem. Soc. 2693 (1964).

Distribution for ANL-06/49

Internal (Printed and Electronic Copies):

J. C. Cunnane (12)
W. L. Ebert (5)
R. J. Finch
J. A. Fortner
A. V. Guelis
J. L. Jerden
M. T. Peters
M. J. Steindler

Internal (Electronic Copy Only):

M. R. Hale, TIS
D. Lewis
D. J. Graziano
G. F. Vandegrift
M. C. Regalbuto
A. J. Bakel
D. B. Chamberlain
M. M. Goldberg
M. Kaminski
C. J. Mertz
Y. Tsai
V. S. Sullivan
M. A. Williamson

External (Electronic Copies Only):

M. A. Buckley, ANL Library-E
P. Bernot, Bechtel SAIC Co
N. C. Painter, Bechtel SAIC Co.
D. W. Thomas, Bechtel SAIC Co.
N. R. Brown, Bechtel SAIC Co.
P. R. Dixon, Los Alamos National Laboratory
P. W. Reimus, Los Alamos National Laboratory
D. J. Weaver, Los Alamos National Laboratory
P. V. Brady, Sandia National Laboratory
D. L. Hanson, Sandia National Laboratory
D. S. Sevougian, Sandia National Laboratory
P. N. Swift, Sandia National Laboratory
C. F. Jove-Colon, Sandia National Laboratory
P. Vaughn, Sandia National Laboratory
S. E. Boggs, Sandia National Laboratory
D. Sassani, Sandia National Laboratory
J. I. Friese, Pacific Northwest National Laboratory
B. D. Hanson, Pacific Northwest National Laboratory

Chemical Engineering Division
Argonne National Laboratory
9700 South Cass Avenue, Bldg. 205
Argonne, IL 60439-4837

www.anl.gov

UChicago ▶ Argonne LLC

A U.S. Department of Energy laboratory
managed by UChicago Argonne, LLC